Spring 2018

An integrated method for understanding the fluid flow behavior and forecasting well deliverability in gas condensate reservoirs with water aquifer drive

Abdulaziz Mustafa Em. Ellafı

AN INTEGRATED METHOD FOR UNDERSTANDING THE FLUID FLOW BEHAVOIR AND FORECASTING WELL DELIVERABILITY IN GAS CONDENSATE RESERVOIRS WITH WATER AQUIFER DRIVE

by

ABDULAZIZ MUSTAFA EM. ELLAFI

A THESIS

Presented to the Faculty of the Graduate School of the

MISSOURI UNIVERSITY OF SCIENCE AND TECHNOLOGY

In Partial Fulfillment of the Requirements for the Degree

MASTER OF SCIENCE IN PETROLEUM ENGINEERING

2018

Approved by

Ralph Flori, Advisor
Shari Dunn-Norman
Mingzhen Wei

ABSTRACT

Gas condensate reservoirs constitute a significant portion of global hydrocarbon reserves. In these reservoirs, as bottomhole pressure falls below the dew point, liquid develops in the pore space. This results in the formation of a liquid bank near the wellbore region that decreases gas mobility, which then reduces gas inflow. Some gas condensate reservoirs have bottom aquifer drive, which also negatively impacts gas production. This research used a field case study to demonstrate an integrated workflow for forecasting well deliverability in a gas condensate field in Libya. The workflow began with the interpretation of open-hole log data to identify the production interval net pay and to estimate petrophysical properties. A compositional model was developed and matched to actual reservoir fluids. Transient pressure analysis was described and used to identify reservoir properties. Inflow performance relationships (IPRs) were analyzed using three types of backpressure equations. The workflow integrated all data in a numerical simulation model, which included the effect of bottom water drive. Sensitivity analysis was used to identify parameters with the greatest impact on future deliverability and recovery. The results provided in this case study demonstrated the importance of an integrated workflow in predicting future well performance in gas condensate fields with bottom water drive. The study demonstrated how to implement the workflow in managing or developing these types of reservoirs.

ACKNOWLEDGMENTS

First, I would like to thank Allah for giving me the strength, knowledge, ability, and opportunity to accomplish this research.

I would like to express my sincere gratitude to my advisor, Dr. Ralph Flori who, has been a great teacher, a friend, an inspiration, a role model and a pillar of support in my guide.

I am thankful for the members of my advisory committee: Dr. Shari Dunn-Norman for her technical guidance and Dr. Mingzhen Wei for her continuous assistance.

I am grateful to the Libyan Ministry of Education for the financial support during my academic study. I also wish to acknowledge Mellitah Oil & Gas B.V. for providing me with all the field data needed to complete this research.

I highly appreciate Mr. Ole S. Fjaere (Kappa Engineering Technical Support), Dr. Mohsen Khazam (University of Tripoli), Prof. Thomas A. Blasingame (Texas A&M), Prof. John Spivey (Phoenix Reservoir Engineering), and Ms. Emily Seals (Missouri S&T) for their valuable explanation and guidance.

My acknowledgement would be incomplete without thanking the biggest source of my strength, my family. This would not have been possible without their unwavering and unselfish love and support given to me at all times.

TABLE OF CONTENTS

Page

LIST OF FIGURES

Page

LIST OF TABLES

Page

1. INTRODUCTION

In recent years, the global demand for energy resources rapidly increased, and as the world oil and gas reserves leveled off, production from existing reservoirs became a greater challenge that required a better understanding of reservoir engineering basics and developed technology applications. Awareness of such concepts plays an important role for any reservoir study. With improvement in technology and knowledge, the achievement of the study becomes much more efficacious. Development plans induced from any study depend mainly on the effects of fluid behavior and reservoir parameters on well productivity and thus the recoverable oil and gas.

Gas condensate fluids behave differently from gas and oil flow. Such distinctive behavior needs to be observed and quantified. Simulation technology is an additional tool for the technical measurement, which can overcome the insufficiency of the experimental measurement. Therefore, the study of the gas condensate flow performance is still a relevant project (Al-Shaidi et al., 1997).

1.1 SIGNIFICANCE OF GAS CONDENSATE IN GAS PRODUCTION

Gas condensate reservoirs constitute an important portion of global hydrocarbon reserves that are economically profitable. Gas condensate reservoirs comprise more than 6,183 trillion cubic feet of the world's gas reserves (U.S. Energy Information Administration., 2015). The most important gas condensate reservoirs in the world that contain huge reserves are located in the following fields: the Arun field in Indonesia, the Shtokmanovskoye field in the Russian Barents Sea, the Karachaganak field in the

Kazakhstan, the offshore North field in Qatar, the South Pars field in Iran, and the Cupoagua field in Colombia (Li et al., 2005). This research will focus on the importance of gas condensate reservoirs in Libya. Libya has 1,504.9 billion cubic meters of proven gas reserves, and the main gas condensate fields are distributed in the following fields: W-12, F-12, N-8, and North African (National Oil Corporation of State of Libya).

1.1.1 Gas Condensate Phase and Fluid Flow Behavior. Considering the reservoir conditions (pressure and temperature), Figure 1.1 shows a phase diagram of the gas condensate system. The two-phase region is enclosed within the bubble-point line, the dew-point line, and the critical point. The lines numbered inside the two-phase region are called quality lines, and each represents the liquid fraction within the fluid defined at certain reservoir conditions. For typical gas condensate reservoirs, the initial pressure is above the cricondenbar, which refers to the maximum pressure at which the two-phase region can exist in equilibrium. The initial reservoir temperature for a gas condensate system lies between the critical temperature and the cricondentherm (Raghavan et al., 1996).

The typical reservoir temperature for gas condensate reservoirs is normally 200˚F to 400˚F, while the reservoir pressure is between 3,000 up to 15,000 psia. The produced fluid from a gas condensate reservoir characterized with a colorless to slightly colored fluid, the variety of the conditions that gas condensate fluid exists in allows the fluid to gain a wide assortment of physical status. For gas condensate fluids, the liquid/vapor ratio and gas-oil ratio usually reversed to condensate-gas ratio unlike conventional gases since there is a remarkable amount of liquid fraction especially in rich gas condensate fluids, the

condensate-gas ratio (CGR) can be more than 300 Stb/MM Scf according to the Headlee Devonion field in West Texas (O'Dell et al., 1967).

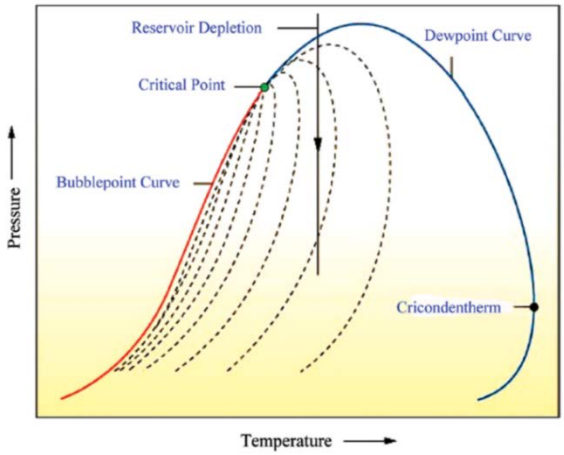

Figure 1.1. A typical gas condensate phase envelope (Zendehboudi et al., 2012).

Gas condensate reservoirs exhibit complex behavior during production when the pressure drops below the dew point. This behavior is called retrograde phenomenon, where the liquid starts to dropout from the gas. The composition of the fluid changes when reservoir pressure decreases. As a result, liquid volume increases and accumulates near the wellbore region until reaching the maximum volume. After a period of production, the condensate banking will be created, which will affect the reservoir performance significantly.

Due to the complex behavior of gas condensate reservoirs, engineering and operating methods are significantly different from conventional oil and gas reservoirs. The development and operation of gas condensate reservoirs require a sufficient understanding of the phase behavior of gas-condensate systems under isothermal depletion and need

precise estimates of reservoir properties in order to maximize recovery of these reservoirs (Al-Ismail et al., 2010).

Optimizing the recoveries for both gas and oil in gas condensate reservoir systems should consider the effect of condensate blockage that occurs during depletion by trying to reduce the loss of condensate inside the reservoir in order to economically increase the profit of production plans regardless of any enhance oil recovery (EOR) processes (Fevang et al., 1995).

1.1.2 Water Influx Gas Condensate. Wells. In gas condensate reservoirs, the pressure declines during the gas and condensate production; for reservoirs with aquifer connections, the water from the aquifer tends to invade the interconnected zones between the reservoir and the aquifer, which is usually referred to as water encroachments. In some cases, the invasion of the water is significantly sufficient to maintain high pressure support and thus maintains the well deliverability. This support could extend to a higher level than the natural depletion cases (Faizan et al., 2014).

The amount of water invading the reservoir depends on aquifer parameters such as permeability, compressibility of formation rock, and the aquifer size. The permeability has been proven as the parameter with most influence on the aquifer support. This factor contributes to how much time it would take the water to replace the fluid produced from the reservoir. Higher aquifer permeability will provide an excellent pressure support, while very low aquifer permeability will cause lower invasion into the reservoir mechanism. Unfortunately, the active water support causes some problems in gas recovery; the water flow toward the reservoir traps the gas inside it and eventually results in early abandonment (Faizan et al., 2014).

The development strategy of offshore gas condensate reservoirs with aquifer supports requires deep understanding of how to maintain the advantage of pressure support caused by the aquifer while controlling the well deliverability. Producing gas at a lower rate is a suggested scenario and in this thesis. Research will investigate and analyze a case study of a Libyan offshore gas condensate reservoir with similar conditions.

1.2 PRESSURE TRANSIENT ANALYSIS

Well testing is an effective tool that plays the main role for monitoring reservoir performance and well conditions. The transient pressure behavior that generates through a reservoir during the test is caused by a change in production rate. After that, the pressure transient response is analyzed in order to obtain information that will make decisions about how to produce and develop the reservoir (Spivey et al., 2013). The following parameters are the main information obtained from the well-testing analysis: Reservoir transmissibility, wellbore storage, skin factor, initial reservoir pressure, and reservoir boundaries.

There are several tests of pressure transient analysis in which each test is dedicated to a specific stage of reservoir discovery, development, and production. The drill stem test (DST) and wireline formation test are normally run for the exploration and appraisal wells. Through reservoir life, conventional well tests such as drawdown, buildup, interference, multi-rate, multi-layer, and pulse tests are utilized for surveillance of the reservoirs performance (Kamal, 2009).

Each type of tests has a level of accuracy and various reservoir properties that can be obtained. For example, the buildup test is more precise than the drawdown test in permeability estimation; however, the drawdown test has higher accuracy than the buildup test in skin factor determination. Table 1.1 lists the types of tests and different information that can be obtained from each test (Kamal et al., 1995).

Table 1.1. Reservoir properties obtainable from various transient tests (Kamal et al., 1995).

Types of Tests	Data Obtained
Drill Stem Test (DST)	Reservoir behavior Fluid samples Permeability Skin Fracture length Reservoir pressure Reservoir limit Boundaries
Wireline Formation Test	Reservoir behavior Fluid samples Some reservoir properties
Buildup Test	Reservoir behavior Permeability Skin Reservoir pressure Boundaries
Multi-rate Test	Formation parting pressure Permeability Skin
Falloff Test	Mobility in various banks Skin
Falloff Test	Reservoir pressure Fracture length Location of front Boundaries

This research focuses on the analysis of the drawdown test and buildup test to define the reservoir behavior and obtain reservoir permeability, skin, average reservoir pressure, and draining area to build reservoir simulation, which will be discussed in Section 3.

1.2.1 Drawdown Test. In the drawdown test, the well is tested at a constant flow rate for a period of time in which the pressure response is measured as the pressure decreases (drawdown), as illustrated in Figure 1.2 (Spivey et al., 2013).

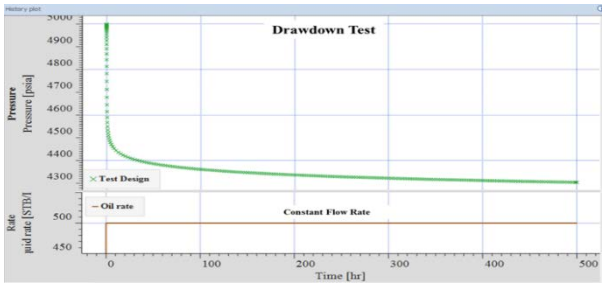

Figure 1.2. Drawdown test (modified from Spivey et al., 2013).

1.2.2 Buildup Test. In the buildup test, the well is tested at zero flow rate for a period of time in which the pressure response is measured as the pressure increases (buildup), as shown in Figure 1.3 (Spivey et al., 2013).

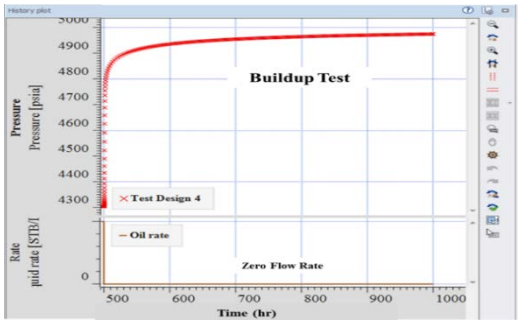

Figure 1.3. Buildup test (modified from Spivey et al., 2013).

1.3 FLOW REGIME CATEGORIES

Fluid flow in porous media is described by using the diffusivity equation that is derived by combining three physical principles: The continuity equation, Darcy's law, and the equation of state for a slightly compressible liquid. The type of fluid flow throughout the reservoir depends on the shape and size of the reservoir. The flow changes over time based on pressure and rate change. Flow behavior is classified into three main flow regimes: steady-state flow, pseudo-steady state flow, and unsteady state flow (Spivey et al., 2013).

1.3.1 Steady-state Flow. Steady-state flow occurs during the late time region when the reservoir is under strong or weak water aquifer or has a gas cap expansion that assists to maintain and support the reservoir pressure. In steady-state behavior, the reservoir pressure does not change anywhere with time in Equation 1.1, which is called the constant pressure boundary.

$$\frac{\delta p}{\delta t} = 0 \tag{1.1}$$

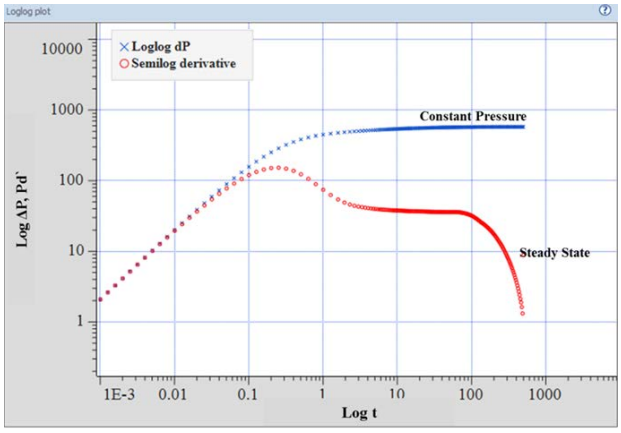

Figure 1.4. Steady-state flow plot for buildup test/drawdown test (modified from Fekete Associates Inc, 2010).

Figure 1.4 is a diagnostic plot (log-log plot) that shows the steady-state behavior at the late time (i.e., the pressure drop line) is constant and the derivative line drops suddenly when the pressure reaches the boundary (Spivey et al., 2013).

1.3.2 Pseudo-steady State Flow. Pseudo-steady state flow occurs during the late time region when there is no flow from the outer boundaries in the reservoir. This behavior is due to the effect of nearby producing wells or the presence of sealing faults. The closed boundary system acts as a tank system that results from a constant pressure drop for each unit of time under a constant rate production shown in Equation 1.2.

$$\frac{\delta p}{\delta t} = \text{Constant} \tag{1.2}$$

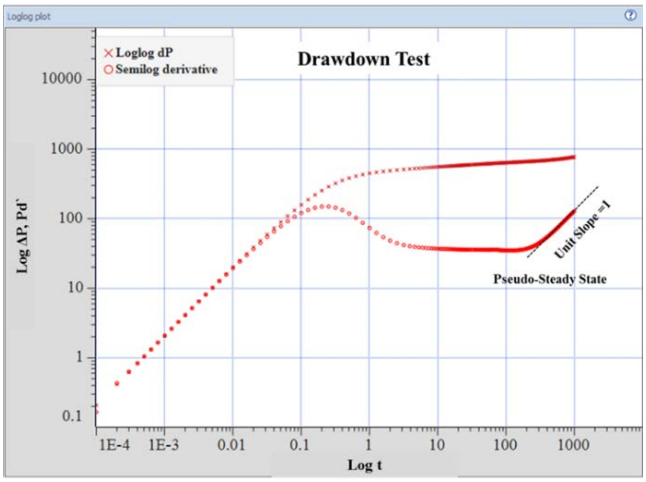

Figure 1.5. Pseudo-steady state flow plot for drawdown test (modified from Fekete Associates Inc, 2010).

This behavior is also called the semi-steady state or depletion state. In the drawdown test shown in the pressure derivative plot (log-log plot) in Figure 1.5, the flow behavior creates the unit slope (slope=1) when the pressure drop reaches the boundary at

the late time. In contrast, the pressure derivative in the buildup test and falloff test does not create the unit slope, and the pressure drop line and the derivative line act like steady-state behavior when the pressure reaches the boundary, as shown in Figure 1.6 (Ahmed, 2006).

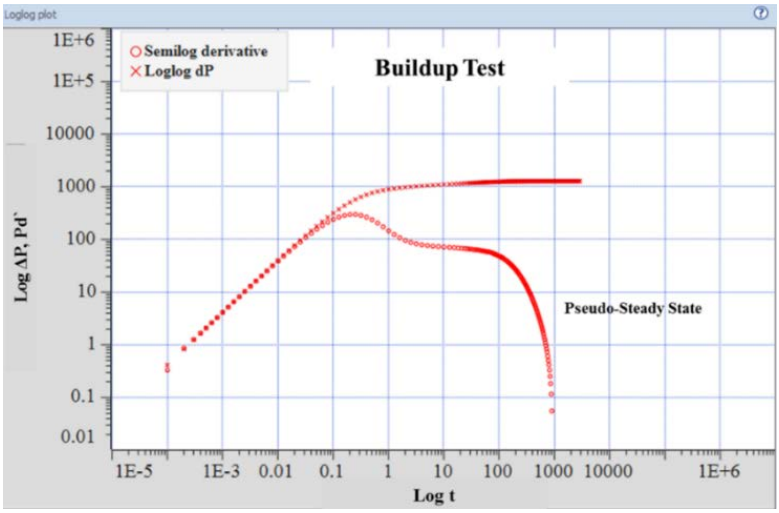

Figure 1.6. Pseudo-steady state flow plot for buildup test (modified from Fekete Associates Inc, 2010).

1.3.3 Unsteady State Flow. Unsteady state flow or transient flow occurs in the middle region of the reservoir formation. The fluid flow condition in the transient period is defined in Equation 1.3 as the rate of change of pressure with respect to time being equal to a function of position in the reservoir and time.

$$\frac{\delta p}{\delta t} = f(i, t) \tag{1.3}$$

The transient flow is a very important region that is used to obtain reservoir permeability and heterogeneity. This flow is also called infinite acting radial flow (IARF) and is known from the diagnostic plot (log-log plot) when the flow creates zero slopes in the pressure derivative line, as shown in Figure 1.7 (Fekete Associates Inc, 2010).

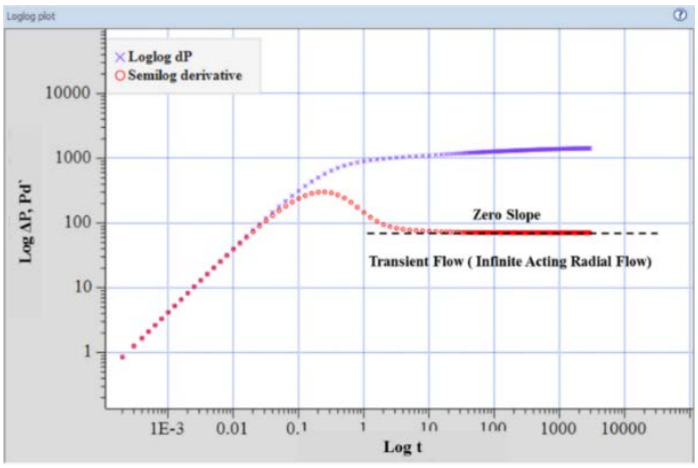

Figure 1.7. Unsteady state flow plot for buildup test/drawdown test (modified from Fekete Associates Inc, 2010).

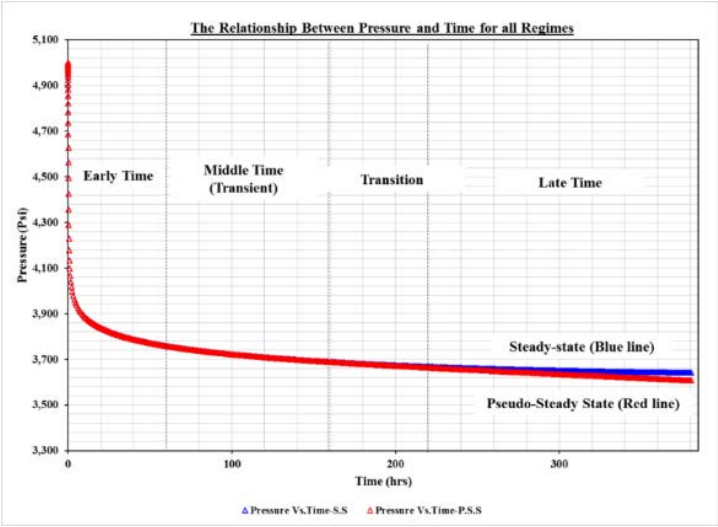

Figure 1.8. Plot of pressure versus time for all regimes (modified from Fekete Associates Inc, 2010).

Figure 1.8 illustrates the typical plot of pressure with respect to time for fluid flow behavior throughout the reservoir. The pressure derivative shows the different flow categories, where S.S is the steady-state flow and P.S.S is the pseudo-steady state flow, as shown in Figure 1.9.

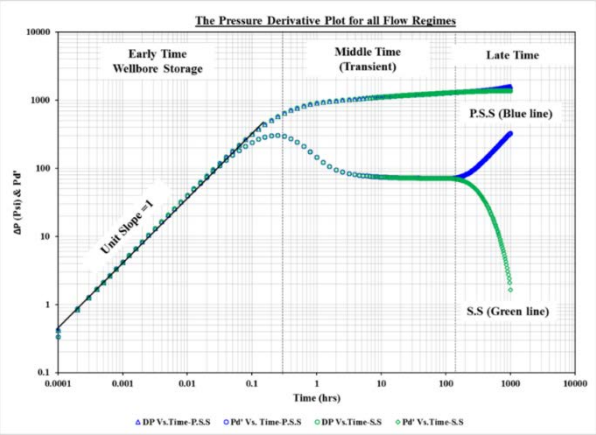

Figure 1.9. The pressure derivative plot for all regimes (modified from Fekete Associates Inc, 2010).

Flow regimes occur for each flow period. Table 1.2 lists the flow regimes for vertical wells.

Table 1.2. Specific flow regimes within all categories (Fekete Associates Inc, 2010).

Early Time	Middle Time	Transition Time	Late Time
Wellbore storage	Radial flow	Single no-flow boundary	Pseudo- steady state
Linear fracture		Linear channel	Steady state
Bilinear fracture			
Spherical			

1.4 WELL DELIVERABILITY

Well deliverability is well production rate as a function of some constraining pressure. Strictly speaking, this rate pressure relation should be defined at the wellhead, and so defining the well deliverability relation includes all sources for pressure loss from the reservoir to the surface separators (bulk reservoir, near the wellbore, tubing, and gathering lines). A less useful but commonly used definition of the well deliverability

considers only the pressure losses in the reservoir ("wellbore" deliverability). Because gas is always sold at the surface, deliverability calculations (and rate-time production forecasts) should always be based on the wellhead deliverability relation (Fevang, 1995).

The well deliverability test is the most widespread and precise method that is used in the oil and gas industry. The test is run by producing wells at several different flow rates in order to measure the production capabilities, also known as absolute open flow (AOF) potential, under a specific condition of reservoir and bottomhole flowing pressure. Deliverability of gas well is predicted by using one of the following three methods: conventional back-pressure, isochronal test, or the modified isochronal test in which the flowing pressure and flow rates are recorded during the test as a function of time. Stabilization is the main assumption required for all three methods, and the basic semi-steady-state flow equation is used in its analysis techniques. The deliverability test is usually done when the well is put on production for the first time and throughout the reservoirs life. The test can provide parameters that are vital for processes such as compression design, reservoir simulation studies, performance of the oil and gas reservoir development plan, and reliable information to support future exploration and development (Urayet, 2011).

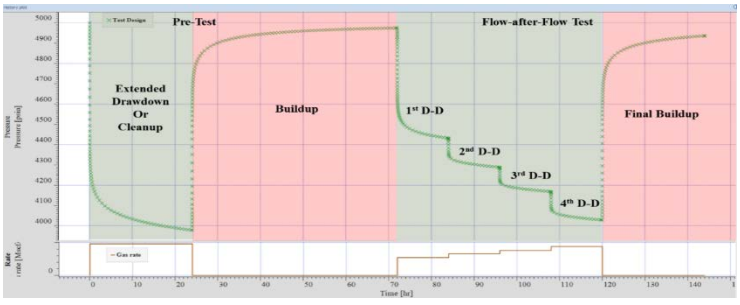

Figure 1.10. Flow-after-flow test.

The deliverability for this case study was measured using the flow-after-flow test in 2009 and 2014, which consists of four drawdown tests and one buildup test at the final period of the deliverability test, as shown in Figure 1.10.

1.5 MODELING OF COMPOSITIONAL SIMULATION

To be able to understand the specifications of the fluid flowing through the reservoir in gas condensate systems must need to quantify the physical properties of the fluid also observe and predict the phase behavior; both are dependent on the fluid composition and pressure at the reservoir temperature.

The process of quantifying the physical property using experimental measurement is essential in understanding the flow behavior of the fluid, property measured using experimental measurement are like viscosity, saturation pressure, and the liquid dropout volumes. Such measurements are conducted under a narrow range of conditions, and this is considered as a shortage since the engineering calculations cover a wide range of reservoir production conditions. In addition, the experimental measurement is very expensive and time-consuming and thus engineers have developed easier techniques.

Equations of state are developed by engineers and used as a substitute for the experiment. These equations represent a relationship between the pressure, temperature, and volume predict the fluid behavior in any condition. The most known and commonly used equations of state in the petroleum industry are the Peng-Robinson and Soave-Redlich-Kwong equations. Relative volume along with oil viscosity measurements are used to tune the equation of state in order to properly mimic the fluid behavior at any

condition. Actually, tuning the equation of state is not an easy job, but with computer technology, engineers have been able to reach a higher level of accuracy. Figure 1.11 represents a measured constant volume depletion test and a predicted liquid dropout curve using PR-EOS for a gas condensate system.

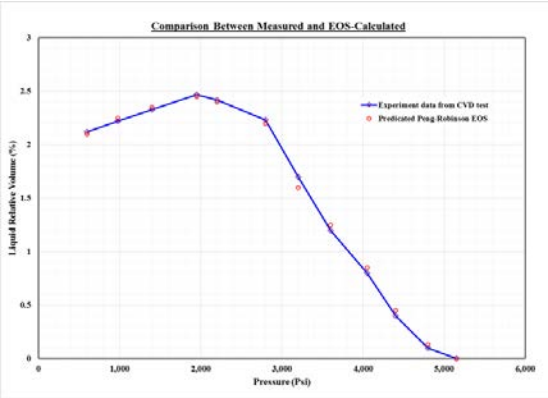

Figure 1.11. Liquid dropout curve at 220˚F for binary gas condensate system (modified from Whitson et al., 2005).

The tuned equation of state is used within useful technology such as compositional simulation to predict and simulate the whole behavior of the reservoir fluids during all of their production scenarios. This powerful technique enables us to study and conclude the best and most profitable development plans for the gas condensate reservoir.

1.6 RESERVOIR SIMULATION

Reservoir simulation is a remarkable technology in the area of the petroleum industry, it provides a full detailed picture of what goes through the reservoir up to the production and surface processes. With applications such as reservoir forecasting, history

matching, development scenarios, and reservoir management, the reservoir simulation has been an essential part of any comprehensive study of reservoir performance.

The simulation model describes almost the actual reservoir behavior based on actual data such as reservoir fluid properties analysis (PVT), well-testing, special core analysis (SCAL), and production data, although with mathematical equations that depend on a reasonable assumption within the simulator itself. The model will be valid to represent the reservoir behavior. With accurate input of characteristics and information, the reservoir simulator can forecast the reservoir deliverability, and along with history matching, it can help in the assessment of reservoir development strategy and management. The aim of building such models is that multiple runs of different development schemes can be made within a short time and at lower expense. Observation of each model has concluded the optimal production strategy for the reservoir to apply the best mechanisms to enhance the reservoir deliverability and the optimal recovery (Abdrakhmanov, 2013).

There are various reservoir simulators, which are distinguished by type. Choosing the right type of reservoir simulator is essential in solving the reservoir problems and building the reliable models. Based on the type of fluids flowing through the reservoir, there are two main and commonly used reservoir simulators as follows: the black oil simulators and compositional simulators.

The black oil simulators deal with only two components, oil and gas. This type of simulator is used in cases where the compositional changes in the reservoir fluids are not significantly affected on the recovery of the reservoir. Such simulator is used with black oil reservoirs.

The compositional simulator represents the reservoir fluids with multiple components. Each component can be found and expressed in both the liquid and the vapor phase. Unlike the black oil, the compositional simulators are used in a variety of situations in which a black oil simulator does not adequately describe the fluid behavior of the reservoir. They are also used in where the recovery is very dependent on the compositional changes throughout the reservoir fluid. Gas condensate reservoirs are typical cases where compositional simulators are used to visualize the changes of fluid compositions and the pressure maintenance caused maybe by aquifer support. Furthermore, multiple miscible contacts occurred in some EOR process (Zhangxin, 2007).

1.7 OVERVIEW OF THE NORTH AFRICAN FIELD

North African gas and condensate field is the Libyan field that is located in the Mediterranean Sea. The structure of the field is an ENE/WSW trending narrow and elongated anticline about 31 miles long and 2.4 miles wide. The reservoir rock type is composed of carbonate facies. Generally, the field has good petrophysical characteristics. The activities of exploration in the field started in 1977 and 1979 by drilling two wells, followed by five more exploratory wells. The production started in the field in 2005 and currently produces around 600 million standard cubic feet a day (MMscf/d) of sales gas and around 30,000 barrel per day of condensate (Bbl/d).

1.8 RESEARCH OBJECTIVES

The primary objective of this research was to interpret the real field data for the North African gas condensate field using an integrated reservoir engineering method. Due to the complex behavior during the production process in gas condensate reservoirs, the reservoir simulation studies was established in order to understand and investigate the fluid flow behavior throughout the reservoir. The aim of the reservoir simulation was predicting the reservoir performance and defining the reservoir parameter that highly impacted the reservoirs performance. In order to build the reservoir simulation study, several approaches were utilized to determine the reservoir and fluid properties. The objective of each method is described as follows:

1. Formation Evaluation Using Open-hole Logs.

The primary objective of this approach was to detect the reservoir boundaries that contain the hydrocarbon. Also, the petrophysical properties were determined in order to build the reservoir properties section in the reservoir simulation study. In addition, the results that were obtained from the analysis represent the reservoir properties with the goal of having a representative model to obtain reliable outcomes.

2. Compositional Simulation and Gas Properties Correlations.

The aim of this tool was to have the probable reservoir fluid model that represents the field in order to investigate the reservoir fluid behavior, especially the liquid dropout, during the depletion process. The precise model can predict the future liquid behavior through the formation and near the wellbore region. On the other hand, the correlation methods were used to confirm the laboratory results of the gas properties. These properties

are crucial in the well-testing interpretation and the objective of confirming the results to avoid the error in the interpretation and obtain the accurate results.

3. Transient Pressure Analysis

Well testing is the effective tool that was used in order to define the well, reservoir, and boundary model for North African field. Also, the liquid dropout phenomena could be conducted using this tool. The goal was to detect the radial flow region in order to determine the reservoir permeability, a very important parameter in the reservoir simulation studies. Furthermore, the formation damage or stimulation can be shown using the well-testing approach, which is important to have a deep understanding of the reservoir characteristics. In order to perform the well deliverability, the average reservoir pressure was the target of using well testing interpretation.

4. Well Deliverability

This target of studying the well deliverability was to define the well ability and the potential energy. Moreover, the results were used to perform the inflow performance relationship of the well. As an off-shore gas well, the deliverability calculations are crucial for the gas sell contract, and this approach is used routinely in order to obtain the absolute open flow (AOF) potential. The vertical lift performance plot was performed in this research to estimate the gas flow rate system that can be produced. Several methods were utilized to estimate accurate outcomes in order to have deep results and confirmed them using software applications.

5. Sensitivity Analysis

The primary aim of using the sensitivity analysis approach was to conduct the effect of the water aquifer on the future performance, where the water cut was controlled by

changing the perforation interval from open to close. In addition, the vertical lift performance was measured to define the gas flow system for future years.

1.9 RESEARCH SCOPE

This research applied the integrated approach on the field data for the North African gas condensate reservoir to evaluate and forecast well deliverability. Understanding the behavior of gas condensate reservoirs and water influx effects on the gas recovery is essential for any offshore field management and development in the future. Figure 1.12 illustrates the reservoir applications that were utilized to accomplish this study. These steps were used to obtain results and then mimic the field by establishing the reservoir simulation model in order to achieve the objectives of this research.

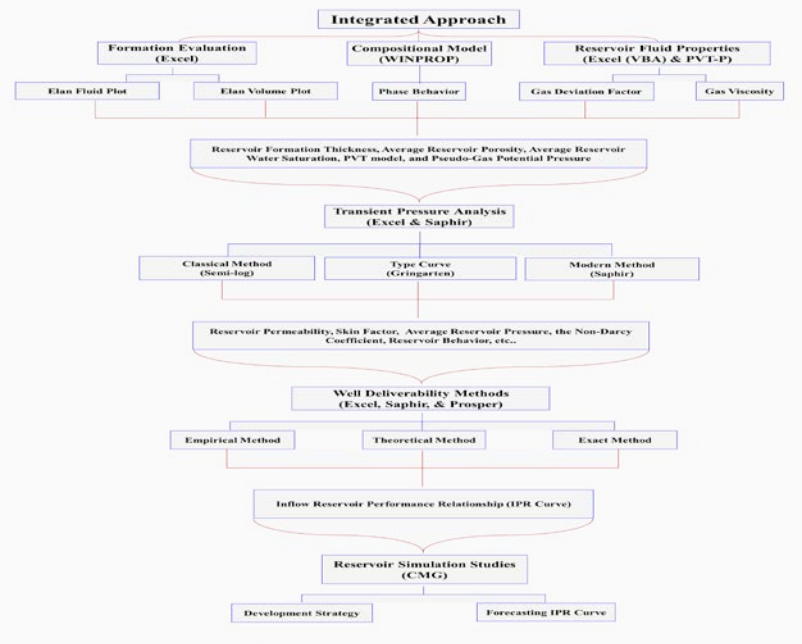

Figure 1.12. Flowchart for research scope.

2. LITERATURE REVIEW

2.1 GAS CONDENSATE CHARACTERIZATION

In general, the hydrocarbon reservoir fluids are classified as oil or gas reservoir fluid, which is mainly differentiated based on the hydrocarbon composition of the reservoir fluid and reservoir conditions (initial reservoir pressure and temperature). Also, the reservoir hydrocarbons are subdivided into arbitrary divisions based on their fluid density (API gravity), fluid color, molecular weight, and a gas-oil ratio, as shown in Table 2.1 (Gravier et al., 1986).

Table 2.1. Typical Characterization for differentiate hydrocarbon type (Wall, 1982).

Characterization	Black Oil	Volatile Oil	Condensate	Gas
Molecular Weight C_7^+, (Ib/Ib.mole)	225	181	112	157
Liquid-Gas Ratio, (Rbbl./MM Scf)	1600	500	55	9.5
Tank oil gravity, (API)	34.3	50.1	60.8	54.7
Color	Green/Black	Pale red/Brown	Straw	White

The phase behavior of gas condensate reservoirs provides a larger variety of conditions due to the large range of pressures and temperatures along with the wide composition ranges. The gas condensate fluid usually contains a large composition consisting of methane and small fractions of short-chain hydrocarbons. Also, the fluid consists of small amounts of long-chain hydrocarbons (heavy end components). The methane fraction contents in gas condensate systems range from 65 to 90 mole (%) and contain a lower amount of heptane and heavier C_7^+. On the other hand, the methane fraction

in crude oil systems ranges from 40 to 55 mole (%) and contains a higher amount of heptane and heavier C_7^+ (Kamath, 2007). The typical composition values for different hydrocarbon systems are shown in Table 2.2. Figure 2.1 illustrates the comparison in the composition of gas condensate systems with other hydrocarbon systems.

Table 2.2. Typical hydrocarbon composition for different fluid types (Wall, 1982).

Component	Black Oil, (%)	Volatile Oil, (%)	Condensate, (%)	Gas, (%)
Methane	48.83	64.36	87.07	95.85
Ethane	2.75	7.52	4.39	2.67
Propane	1.93	4.74	2.29	0.34
Butane	1.6	4.12	1.74	0.52
Pentane	1.15	2.97	0.83	0.08
Hexane	1.59	1.38	0.6	0.12
C_7^+	42.15	14.91	3.8	0.42

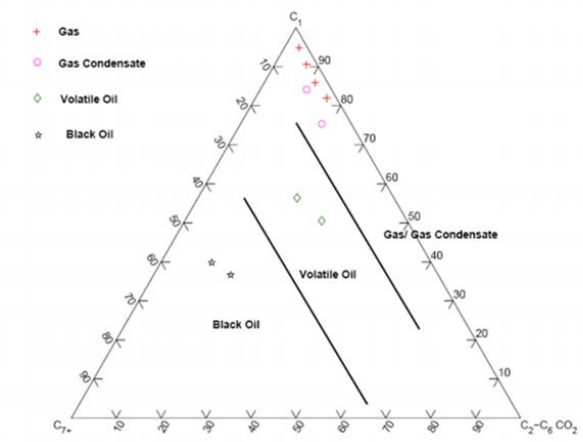

Figure 2.1.Ternary visualization of hydrocarbon classification (Whitson et al., 2000).

Most gas condensate reservoirs were found in deep reservoirs ranging from 5,000 to 10,000 ft. Formation pressures and temperatures ranged from 3,000 to 8,000 psia and 200 to 400 ˚F, respectively (Moses et al., 1962).

The phase envelope of the gas condensate fluid is used to describe the flow behavior of the fluids under different reservoir conditions, as shown in Figure 2.2. In gas condensate reservoirs, the initial reservoir temperature lies between the critical temperature and cricondentherm of the reservoir fluid. At the initial condition, gas condensate reservoirs are often above the dew-point pressure, where the single phase fluid (dry gas) exists only in the reservoir. The fluid composition is changed due to the isothermal expansion through path B-B`, when the reservoir pressure reaches the dew-point line. Then, the retrograde condensation will exist in the reservoir, as shown in Figure 2.2 (Fan et al., 2006).

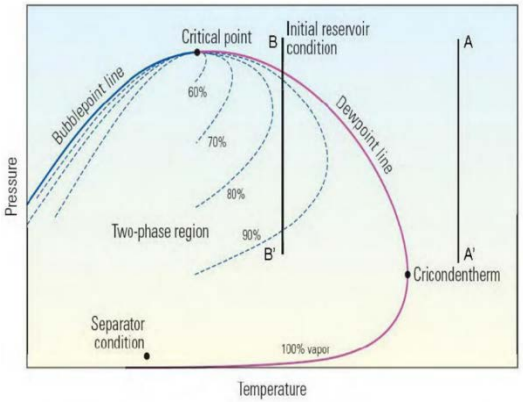

Figure 2.2. Phase diagram of a gas-condensate system (Fan et al., 2006).

The amount of condensate present in the reservoir depends on several factors, such as pressure, temperature, and fluid composition. The gas condensate reservoirs can be divided into categories: a lean and rich gas condensate depending on the fluid composition, liquid recovery, and range of gas-oil-ratio (GOR) (Kgogo et al., 2010).

As shown in Figure 2.3, when reservoir pressure is below the dew-point pressure, a rich gas condensate creates a higher amount of liquid than a lean gas condensate due to

its composition that contains appreciable amounts of the heavier hydrocarbons, such as Butanes (C_4), Pentanes (C_5), Hexane (C_6), and Heptanes plus (C_7^+).

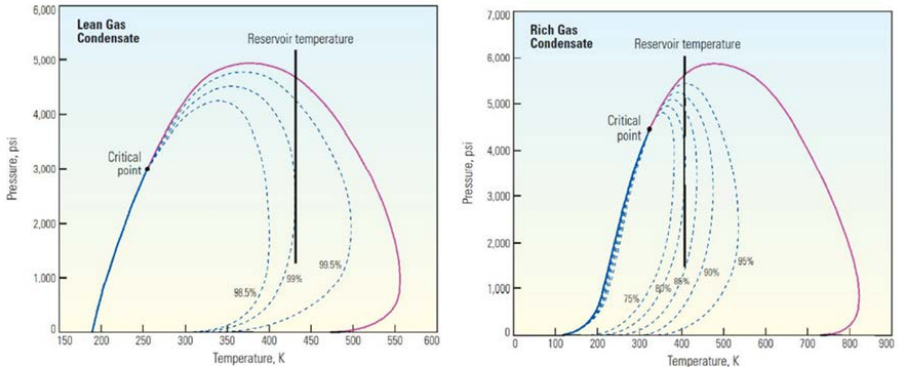

Figure 2.3. Phase diagram of a lean and rich gas condensate system (Fan et al., 2006).

Typically, a rich gas condensate produces a large volume of liquid that is more than 300 barrel per million cubic feet, while a lean gas condensate produces a small volume of liquid less than 30 barrel per million cubic feet, as shown in Figure 2.4 and Table 2.3, respectively (Kamath, 2007).

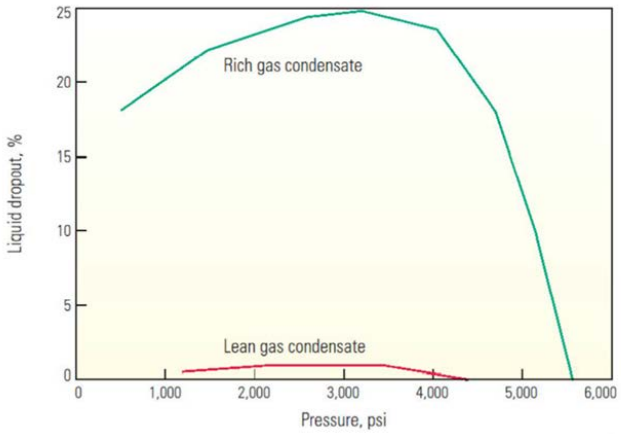

Figure 2.4. Liquid dropout for a lean and rich gas condensate system (Fan et al., 2006).

Table 2.3.Typical values of classification of gas condensate fluid.

Classification	Lean-Condensate	Rich-Condensate
Liquid Recovery, (STB/MM Scf)	20-50	>100
C_7^+, (mole (%))	around 1.71	around 7.47

2.2 GAS CONDENSATE FLOW BEHAVIOR

O'Dell and Miller (1967) introduced a gas flow rate equation included a pseudo-pressure formula in order to describe the impact of condensate banking phenomena near wellbore regions. Their equation is applicable when the condensate blockage radius is small and average reservoir pressure is over the dew-point pressure. The research outcomes showed that the gas well deliverability can be significantly decreased even for small regions of condensate blockage. Later, a radial compositional model was developed by Fussell (1973). This model was used in order to investigate gas condensate behavior below dew-point pressure under depletion production pressure. He modified the O'Dell-Miller equation in order to account for the gas dissolved in the flowing condensate phase. The results indicated that the equation overpredicts the deliverability loss due to the condensate blockage near the wellbore. Furthermore, Jones and Raghavan (1985) studied the transient pressure behavior in the radial gas condensate wells using drawdown and buildup pressure data. This research used a compositional simulation for gas condensate fluid that consists of three components (C_1, C_4, and C_{10}). They noticed at the late time when reservoir pressure reached the reservoir boundary, the Fussell function is only valid for the depletion reservoirs. Fevang and Whitson (1995) proposed a method for calculating well deliverability by using pseudo-gas potential pressure formula. This method is the most

effective to obtain the pressures and saturations easily based on the producing well stream composition (the instantaneous producing GOR). During depletion in gas condensate reservoir, three main different flow regimes can be identified, as shown in Figure 2.5. Single phase (only gas) is shown in region 3 where the reservoir pressure is significantly above the dew-point pressure. This region is far from the wellbore region and has high pressure drop and only gas phase. Condensate buildup starts at a 3,000 ft radius around region 2, where the first liquid dropout occurred when pressure reached the dew-point pressure. However, the liquid phase is still immobile and gas phase is only mobile because the condensate does not reach the critical saturation yet. Region 1 is close to the wellbore region in which the condensate saturation exceeds the critical saturation and starts to be mobile in the reservoir (Gerami et al., 2010).

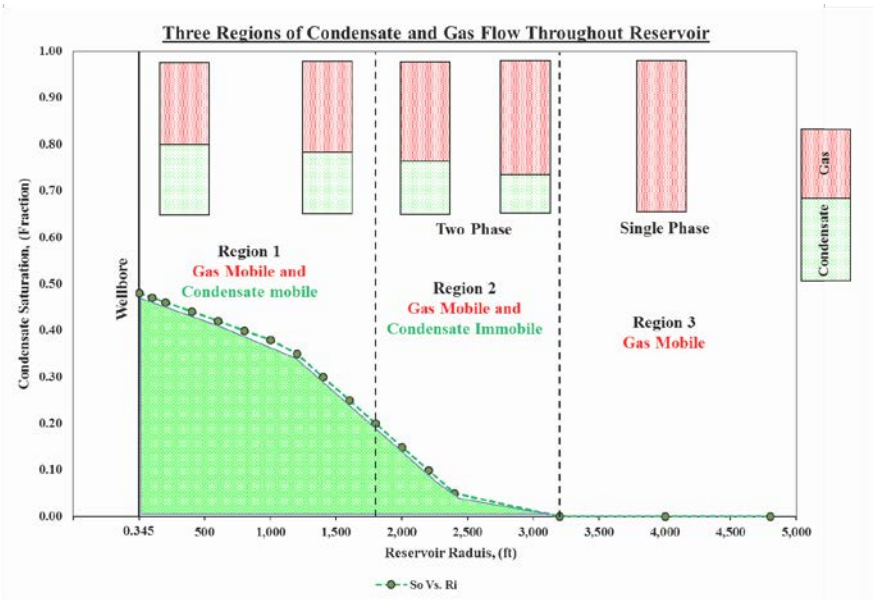

Figure 2.5. Change in condensate saturation and gas throughout reservoir (modified from Roussennac, 2001).

2.3 HISTORY OF GAS WELLS DELIVERABILITY

Inflow performance relationship (IPR) is a crucial factor in a reservoir production system in order to produce wells economically. This relationship indicates reservoir condition and its ability to produce under a specific condition. The deliverability test is a routine test used for gas wells in order to determine reservoir potential flow and build a new design of new wells for future development. In addition, monitoring and optimization processes for producing wells are based on well deliverability results. A common indicator of well productivity is the absolute open flow (AOF) potential. This parameter is defined as the maximum flow rate for the well that could flow at the atmospheric pressure. Though the well cannot produce at the AOF's rate, the AOF is an important value to establish field proration schedules, know maximum allowable production at each well, gather pipeline and system design, and negotiate of sale contracts especially for off-shore wells (Johnston et al., 1991).

In order to calculate a gas well's production capabilities, the relationship between the gas flow rates and flowing bottomhole pressure is required. This relationship is determined by using one of three well deliverability methods: the conventional backpressure test, the isochronal test, or the modified isochronal test. All these methods require four flow rate tests in order to perform the deliverability relationship. After a period of shut in a gas well, the gas flow behavior throughout the reservoir is an unsteady state flow until the pressure reaches the boundary. Then, the flow behavior changes to a steady state or semi-steady state (pseudo-steady state) condition. This means that the flow rate reaches the stabilization deliverability, which is required by three methods (Chase, 2002).

Backpressure test is also known as a flow-after-flow test, which is normally conducted by producing in a sequence of at least four increasing flow rates (four point backpressure test), as illustrated in Figure 2.6.

In case of high liquid ratio wells, the reverse sequence (decreasing flow rates) is necessary in order to clean up the wellbore from the liquid volume, as shown in Figure 2.7.

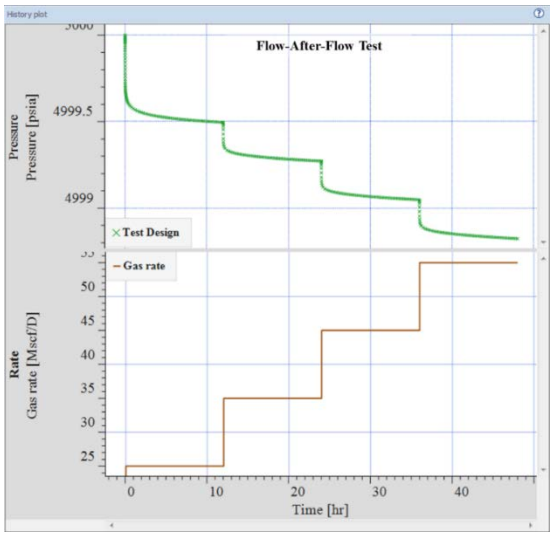

Figure 2.6. Typical flow-after-flow test.

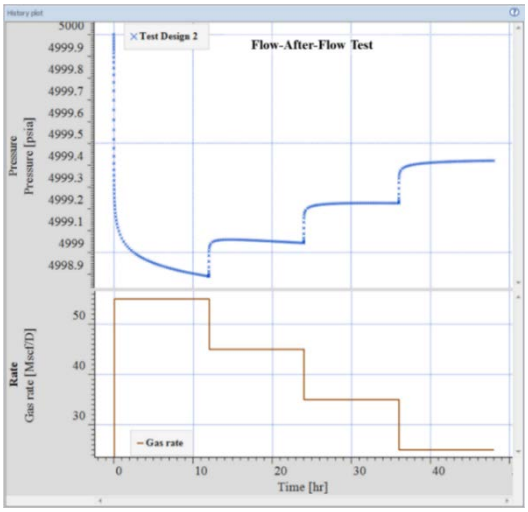

Figure 2.7. Reverse sequence of flow-after-flow test.

The test is required to reach a stabilization period (steady state or pseudo-steady state flow) at each flow rate in order to determine the deliverability results successfully. The stabilization period depends on the time in transient period flow. In high reservoir permeability, the test takes a shorter amount of time to reach stabilization. As a result, the conventional backpressure test is only valid in high reservoir permeability (Urayet, 2011). When using a single-point backpressure test, a well produces at a single flow rate in order to reach the stabilization period. This can introduce significant error in the determination of absolute open flow (AOF) potential (Poe et al., 1988).

On the other hand, the isochronal and modified isochronal tests were developed for low reservoir permeability (shorter test times). As shown in Figure 2.8, these tests have a similar procedure, where wells producing at a constant flow rate and is then shut-in the well to allow it to buildup and reach the average reservoir pressure before beginning the next flow rate period. The time duration is the only difference, where the modified isochronal test is not long enough to reach the drainage reservoir area (and thus the average reservoir pressure). Both tests require the single stabilization period in order to perform the well deliverability (Johnston et al., 1991). Cullender (1955) introduced the isochronal performance method as an empirical method in order to determine the flow characteristics of gas wells. Furthermore, the modified isochronal test technique was presented by Katz et al. in 1959 (Hashem et al., 1996).

The basic practical test of the conventional flow-after flow backpressure test was developed by Pierce and Rawlins (1929), where they studied the fundamental basis for controlling and gauging natural gas wells by computing the pressure at the sand in the gas well.

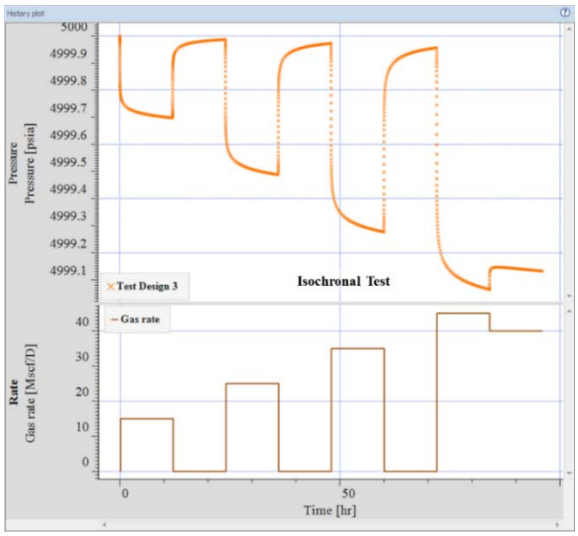

Figure 2.8. Typical isochronal test.

After that, Rawlins and Schellhardt (1936) introduced the concept of the conventional deliverability test (backpressure testing) using the flow-after-flow test, which was developed empirically using the observation method of a number of gas well tests. They noticed that the relationship between difference squares of the average reservoir pressure and bottomhole flowing pressure versus gas flow rate on a logarithmic graph gives a straight line relationship, where the reverse of the slope is n (the performance exponent) and the intercept over negative value of n is C (the stabilized performance coefficient). The theoretical value of n depends on the fluid flow throughout reservoir where ranges from 0.5 turbulent flow indicators to 1.0 laminar flow indicator. The empirical equation is frequently used in deliverability test analysis, which is applicable only at low pressures. Although the empirical equation is not theoretically rigorous, this equation is still widely used in oil and gas industry for deliverability analysis, especially when the absolute open flow (AOF) potential from the test is minimal compared to other methods. Later, the

empirical method was adjusted by replacing normal pressure with pseudo-gas potential pressure in order to modify the equation to be applicable over all pressures and obtain an accurate absolute open flow (AOF) potential value (Lee, 1982).

Moreover, Houpeurt (1959) developed the empirical equation in order to have more precise analysis for absolute open flow potential by modeling the theoretical method. This method requires stabilization data measured during pseudo-steady state flow. On the other hand, Brar and Aziz (1978) predicted well deliverability without using stabilized flow data based on the transient Houpeurt deliverability equation (Lee, 1982).

This research focuses on the deliverability analysis for the flow-after-flow test used for high permeability formation and pseudo-steady state flow. The theoretical consists of two theoretical factors that can be estimated if reservoir property data are available. These coefficients are a and b, which also can be determined from flow-after-flow data. The absolute open flow (AOF) potential using the theoretical method is determined by using pressure square, where the squared pressure difference divided by gas flow rate is plotted versus gas flow rate data. This relationship is plotted on a linear plot (Cartesian scale), where a is the intercept and b is the slope (Hashem et al., 1996).

In order to apply inflow performance relationship is to a wide range of pressure, the exact method is used by replacing the pressure squared with gas pseudo-pressure. Houpeurt equations are rigorously correct, and using the empirical method (Rawlins and Schellhardt) could cause an incorrect value of absolute open potential flow due to large variations in pressure when extrapolating the empirical equation (Johnston et al., 1991).

2.4 INFLUENCE OF WATER AQUIFER SUPPORT

Water-bearing rock that surrounds some of the hydrocarbon reservoirs is known as water aquifer. The water aquifer is classified into three types: infinite water aquifer, moderate water aquifer, and small water aquifer. These classifications are based on aquifer size. More than half of global gas reservoirs are connected with sizeable underlying aquifers. As pressure falls in the reservoir due to depletion, water invade the reservoir. The water drive plays the main role in hydrocarbon recovery and controls the reservoir performance. As the water aquifer size is bigger, the effect on the reservoir performance is high. The water aquifer assists to maintain reservoir pressure and prevents a lower declines during production. On the other hand, reservoir pressure in volumetric reservoir decline early due to oil and gas withdrawals that lose the reservoir energy where there is no alternative energy that supports the reservoir pressure. In oil reservoirs, the oil production can be maximized by a water drive mechanism from the aquifer, minimizing pressure decline (Ahmed, 2010).

In gas reservoirs, the two major drive mechanisms are volumetric (depletion) and water. The water influx completely affects the production of these reservoirs. Agrawal et al. (1965) studied the importance of water influx in gas reservoirs and considered the water aquifer to have an opposing effect on the gas reservoir recovery. According to Kelker (2008), as the water cut increases in gas reservoirs, the gas production decreases due to the gas trapped saturation, which causes early abandonment these reservoirs with high gas residual saturation. According to research studies that have been done by Charles et al. (1999) Givens (1968) and Firoozabadi et al. (1987), the gas recovery from the volumetric

reservoir is around 80% to 90%. On the other hand, the gas recovery factor for partial water drive mechanism is close 70% to 80%, while that for a strong or active water drive mechanism is around 35% to 60% (Ogolo et al., 2014).

A feasibility study has been done in order to improve the gas recovery by water influx control in water drive gas reservoirs by Ogolo et al. (2014) (SPE-172364) where the objective is to prevent water encroachment into the gas reservoirs by keeping the gas zone from direct contact and injecting CO_2 at the gas water contact. The results showed that the CO_2 injection reduces water production where the gas and condensate recovery was improved.

3. METHODOLOGY

Several steps are required before determining the well deliverability and establishing the simulation model that represents the North African field. The integrated methods were utilized to interpret the real field data where the interpretation results defined the reservoir behavior and characteristics in order to build the representative model. The research procedures were started with the formation evaluation interpretation, compositional model, and PVT analysis to define the reservoir gas properties. After that, well-testing interpretation and well deliverability calculations were done, respectively. Finally, reservoir simulation studies were done in order to investigate the gas condensate phenomena and the water drive effect. This research was done using the following reservoir and production engineering tools:

- Excel (VBA),
- Petroleum Expert package (PVT-P and Prosper software),
- Kappa Engineering package (Saphir software),
- CMG Simulator (GEM and WINPROP).

3.1 OPEN-HOLE LOGS INTERPRETATION

Open-hole logs are combination tools that are usually available immediately after drilling to evaluate the formation of interest. The primary objective of formation evaluation methods is the identification of reservoir boundaries and estimation petrophysical properties that are the important inputs for hydrocarbon reserve calculations, estimation of recoverable hydrocarbon, well-testing interpretation, and reservoir simulation studies

(IPIMS, 2012). The data that were provided by the company are limited to the specific logging tools. These data were used to build a formation evaluation model in order to obtain the formation thickness, average reservoir porosity, and average initial water saturation about the formation target. The wireline logging data were measured through one foot of the formation, and then the GR log, sonic interval time, and the formation resistivity data were gathered and plotted versus the formation depth in different scales based on the type of log, as shown in Figure 3.1. The Excel spreadsheet was utilized for the open-hole logs calculations in order to perform the Schlumberger's Elan fluid and Elan volume.

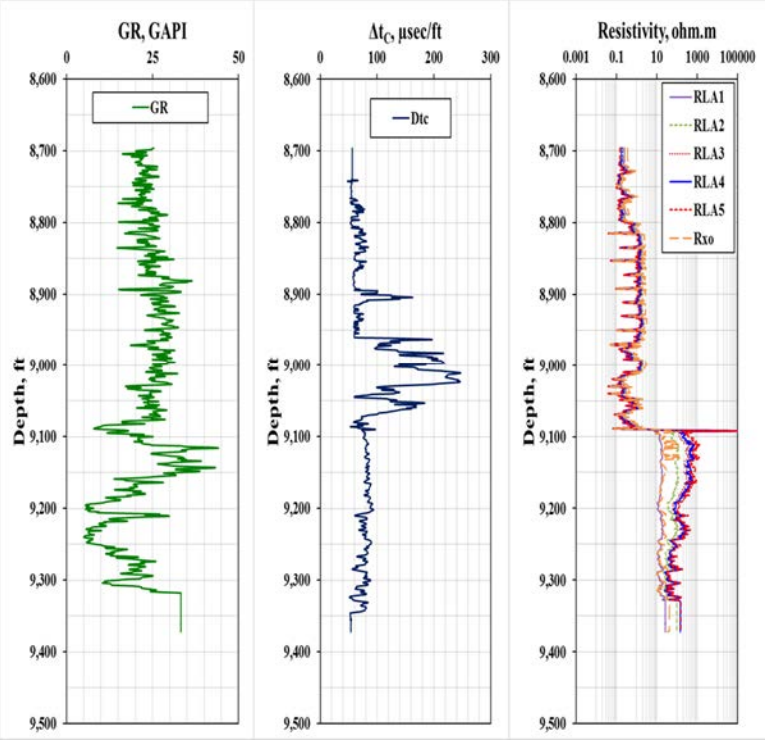

Figure 3.1. Formation evaluation open-hole logs data.

3.1.1 Wireline Logging Tools. First, this section introduces the well logging tools that were used. After that, the interpretation procedure is defined step-by-step.

3.1.1.1 Lithology logs. The gamma ray (GR) log is the most important lithology log used for formation evaluation interpretations in order to identify permeable formations, determine boundaries between permeable and non-permeable formations, and provide lithology information. The GR log measures the natural radioactivity material in formations where a high GR reading represents shale formation and a low GR reading represents clean sand or carbonate formation. Also, the GR log is used to calculate the volume of shale, as written in Equation 3.1 (Schlumberger, 1972).

$$V_{sh} = \frac{GR_{Log} - GR_{Min}}{GR_{Max} - GR_{Min}} \quad (3.1)$$

Where:

V_{sh} = Volume of shale content in formation, (fraction)

GR_{Log} = Gamma ray reading of formation, (GAPI)

GR_{Min} = Minimum gamma ray (clean sand or carbonate), (GAPI)

GR_{Max} = Maximum gamma ray (shale), (GAPI)

3.1.1.2 Porosity logs. The sonic log is the porosity log tool used to record the interval transit time (Δt) of a compressional sound wave traveling through one foot of formation (Asquith et al., 1982). The main objective of the porosity log is to provide accurate lithology and porosity determination, formation stress determination, abnormal pressure detection, and fracture detection. Table 3.1 lists the typical values of sonic velocities and interval transient times for different formation types. These values are utilized in the sonic porosity in Equation 3.2 to define the porosity value (Schlumberger, 1972). The reservoir lithology in this study is the limestone formation, and the values in Table 3.1 for limestone were used for the porosity calculation.

Table 3.1. Sonic velocities and interval transient times for different formations (Schlumberger, 1972).

Formation	V_{ma}, (ft/sec)	Δt_{ma}, (µsec/ft)
Sandstone	18,000 to 19,500	55.5 to 51.0
Limestone	21,000 to 23,000	47.6 to 43.5
Dolomite	23,000 to 26,000	43.5 to 38.5
Anhydrite	20,000	50.0
Salt	15,000	66.7

$$\emptyset_{sonic} = \frac{\Delta t_{Log} - \Delta t_{ma}}{\Delta t_{fluid} - \Delta t_{ma}} \quad (3.2)$$

Where:

$\emptyset_{sonic}$ = Sonic derived porosity, (fraction)

Δt_{ma} = Interval transient time of the matrix (Table 3.1), (µsec/ft)

Δt_{ma} = Interval transient time of formation, (µsec/ft)

Δt_{fluid} = Interval transient time of the fluid in the wellbore (fresh mud=189, salt mud= 185) , (µsec/ft)

3.1.1.3 Resistivity logs. Resistivity logs are also known as the saturation logs where resistance to the flow of electrical current is measured. The saturation logs are normal and lateral devices, laterologs, and induction logs. These logs are designed in order to determine the thickness of a formation, estimate an accurate value for true formation resistivity, utilize the recorded data for correlation purposes, and provide indication about hydrocarbon content in formation (Schlumberger, 1972).

The key equation in formation evaluation studies is Archie's equation, which has wide use in well logging interpretation in order to obtain the formation saturation

distribution. Equation 3.3 and 3.4 are used to estimate initial water saturation, moveable hydrocarbon saturation, and unmovable hydrocarbon saturation.

$$S_w = \left(\frac{F \times R_W}{R_t}\right)^{\frac{1}{n}} \tag{3.3}$$

$$S_{xo} = \left(\frac{F \times R_{mf}}{R_{xo}}\right)^{\frac{1}{n}} \tag{3.4}$$

Where:

S_w = Water saturation, (fraction)

S_{xo} = Flush zone saturation, (fraction)

F = Formation resistivity factor, $F = \frac{a}{\emptyset^m}$

$\emptyset$ = Porosity, (fraction)

m = Cementation factor, which ranges from 1.7 to 3, but normally 2

a = Tortuosity, normally 1

n = Saturation exponent, which ranges from 1.8 to 4, but normally 2

R_w = Formation water resistivity, (ohm.m)

R_t = True formation resistivity, (ohm.m)

R_{mf} = Mud filtrate resistivity, (ohm.m)

R_{xo} = Flush zone resistivity, (ohm.m)

3.1.2 Interpretation Procedures.

1. The previous equations in the wireline logging tools section were used to determine the volume of shale, formation porosity, and water saturation.

2. The water formation resistivity was estimated using Schlumberger's chart Gen-9, as illustrated in Figure 3.2. The following is the procedure to obtain the formation water resistivity value:
    a. The X-axis represents the formation temperature, the right y-axis represents the formation water salinity, and the left y-axis is the target value of the formation resistivity.
    b. The starting point is the formation temperature 285 ˚F where a vertical line was drawn from the temperature value and extended until reaching the formation salinity 75,000 ppm.
    c. The other line was drawn horizontally from the intercept of the formation temperature and the formation salinity, and then extended to the formation water resistivity value that represents the field, as demonstrated by the red arrow.
3. Figure 3.3 illustrates the target formation between two dotted lines, where lower GR reading and separation between the formation resistivity logs are shown.
4. RLA 1, 2 resistivity logs indicate the reading of the formation resistivity in the shallow formation (closest to the wellbore region). On the other hand, RLA3, 4, 5 resistivity logs indicate the reading of the formation resistivity in the deep formation. Rxo is the formation resistivity in the flushed zone affected by the mud filtration process.
5. The separation in the resistivity logs in the target zone indicates that there is hydrocarbon content in this region. In addition, R_{xo} is higher than RLA5 in depths from 8,700 to 9,100 ft, which means the used mud during the drilling process was a fresh water base mud.

6. The value of mud filtrate resistivity (R_{mf}) is a crucial input for the next formation evaluation analysis. Based on the key that showed the used mud is a freshwater base mud, the R_{mf} was assumed to be around 0.0570 ohm.m and higher than the formation water resistivity value.

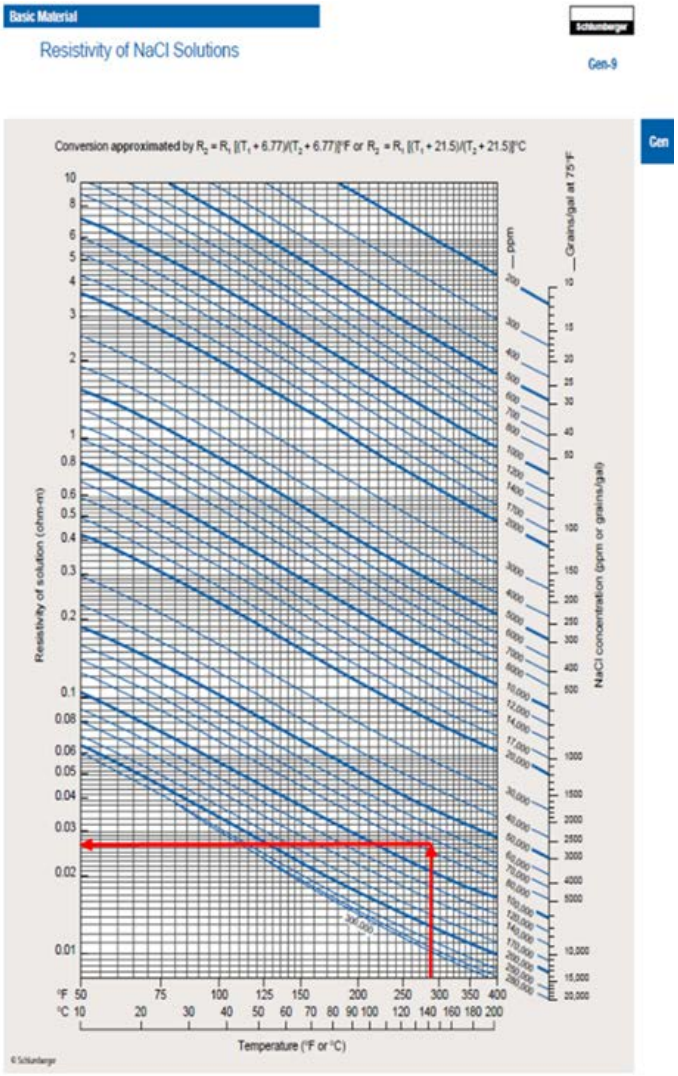

Figure 3.2. Schlumberger's chart (Gen-9) to estimate formation water resistivity (Schlumberger, 2013).

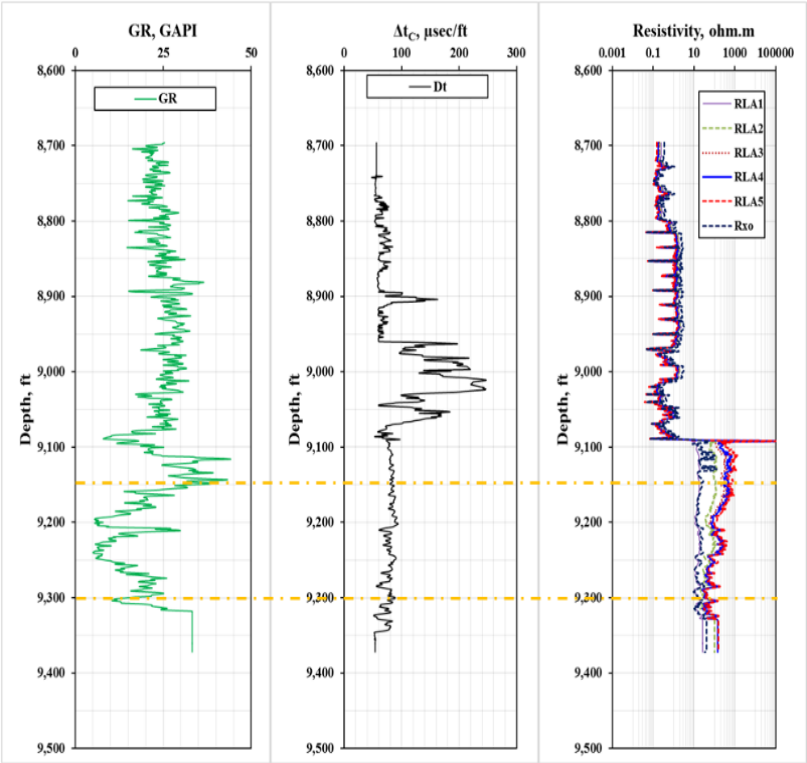

Figure 3.3. The target formation open-hole logs.

7. GR log and sonic log were interpreted in order to perform the Elan volume. Equations 3.1 and 3.2 were used to determine the volume of shale and porosity. On the other hand, the bulk volume and pore volume Equations 3.5 and 3.6 were utilized in order to determine the volume of water using Equation 3.7.

$$V_b = X^3 \tag{3.5}$$

$$V_P = V_b \times \emptyset \tag{3.6}$$

$$V_w = V_p \times S_w \tag{3.7}$$

8. The Elan fluid was performed from the analysis of resistivity log interpretation. The water saturation, movable hydrocarbon saturation, and unmovable hydrocarbon saturation were determined using Archie's Equations 3.3 and 3.4.

9. In order to determine the formation net thickness, the average reservoir porosity, and the average initial water saturation, the cut-off value calculations were used as follows:

Where:

V_b = Bulk volume, (ft^3)

X = Depth interval, which in this case every one foot, (ft)

V_P = Pore volume, (ft^3)

$\emptyset$ = Porosity, (fraction)

S_w = Water saturation, (fraction)

V_w = Volume of water, (ft^3)

a. If shale volume content is 40% (If value of V_{sh} in each layer is higher than 40%, then layer is defined as the shale layer and will not be considered as production formation. On the other hand, if V_{sh} in each layer is lower than 40%, then the layer is considered as the limestone formation “production zone”).
b. Porosity is 6% (if each layer has porosity lower than 6%, then it will not be considered as production formation).
c. Water saturation is 50% (If each layer has water saturation higher than 50%, then it will not be considered as production formation).
d. The final step was the summation of the layer that under previous cut-off value condition to obtain the net thickness value. On the other hand, the average reservoir porosity and initial water saturation were determined using the same procedure, but instead of using the summation function, the average function was utilized to obtain the average values.

3.2 COMPOSITIONAL SIMULATION (PHASE BEHAVIOR)

In reservoir simulation studies, it is crucial to study the phase behavior for the reservoir fluid, especially in gas condensate reservoirs. The compositional simulation was utilized to mimic the reservoir fluid to be representative of the reservoir condition. The compositional model was built using PVT-P petroleum expert package and WINPROP 2013 simulator CMG package. The main function of the software is to match the experiment points from the PVT laboratory measurements tests that are designed for gas condensate reservoirs. The simulator generates the model based on the equation of state (EOS), where the Peng-Robinson EOS was chosen for the phase behavior study. The following are the main procedures in order to obtain the reliable phase behavior model that represents the North African field.

1. The PVT data were gathered from the PVT report.
2. The hydrocarbon and non-hydrocarbon composition series were selected from the library section in the software, as shown in Figure 3.4.
3. The reservoir fluid composition data, molecular weight, reference pressure, reference temperature, and reference depth were entered manually into the software.
4. PVT-P software works based on the Peng-Robinson EOS in order to build the phase envelope for the gas condensate systems.
5. Figure 3.5 shows the phase envelope after running the model, where the saturation pressure (dew-point pressure) did not match with the saturation pressure obtained from the laboratory measurement.

6. Gas-oil-ratio (GOR) and API gravity obtained from the model should match with the PVT laboratory measurements. If not, then the molecular weight and specific gravity of the pseudo-component (C_{13}^{+}) should be adjusted until the target values will be reached.

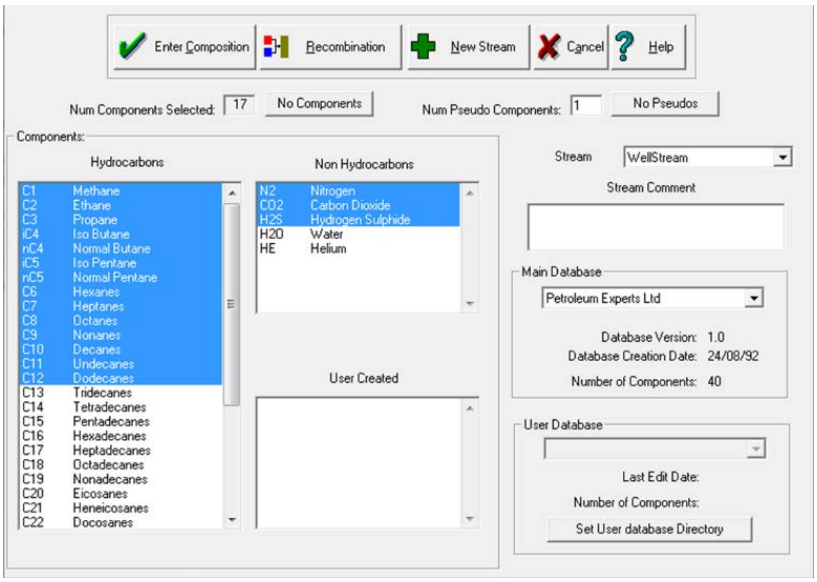

Figure 3.4. The hydrocarbon and non-hydrocarbon series.

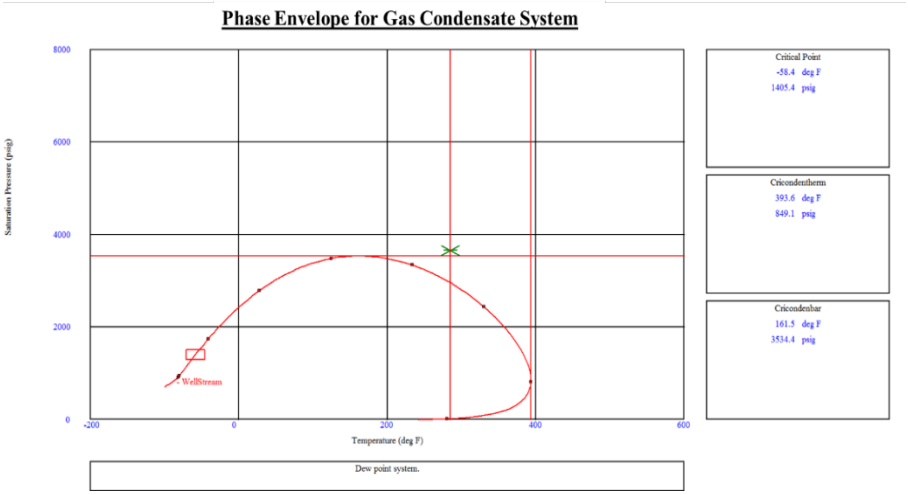

Figure 3.5. Phase envelope for the gas condensate system before reaching the match using EOS.

7. The molecular weight and specific gravity of the pseudo-component (C_{13}^{+}) can be modified by 5-10% until obtaining the close results that match with the PVT report (Akpabio et al., 2014).
8. The saturation pressure was matched, as shown in Figure 3.6 where the molecular weight and specific gravity of the pseudo-component (C_{13}^{+}) were changed to 230 and 0.815, respectively.
9. The values were modified 1.39% for specific gravity of the pseudo-component (C_{13}^{+}) and 1.819% for the molecular weight of the pseudo-component (C_{13}^{+}).

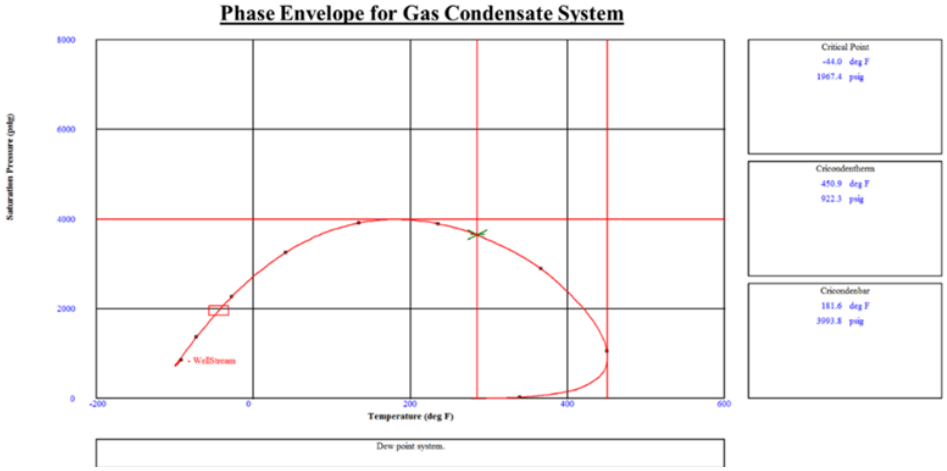

Figure 3.6. Phase envelope for gas condensate system after reaching the match using EOS.

10. The pseudo-component (C_{13}^{+}) properties were corrected and the fluid composition imported into the WINPROP simulator to build the phase behavior for the North African field.
11. In order to establish the precise simulation study, the phase behavior is very important to have representative fluid at the reservoir condition.

12. The pseudo-component (C_{13}^{+}) was split into single carbon number fractions, which was done automatically by the simulator.
13. The constant volume depletion (CVD) test and constant composition expansion (CCE) test were imported into the simulator.
14. The tuning process was done throughout the regression process to match the main two tests for the gas condensate reservoir.
15. The single regression represented by x was done first, as shown in Figure 3.7.
16. The main parameters that needed regression were the critical pressure, critical temperature, acentric factor, and volume shift.
17. The simulator was run and results checked in the log-file, simulation output, and plots.
18. After that, work on the regression process continued by grouping the single components that were split in previous steps until reaching the match for both the constant volume depletion (CVD) test and the constant composition expansion (CCE) test.

Component	Pc (atm)	Vc (l/mol)	Tc (K)	Ace. factor	Mol. W	Vol. shift	V Shift Coef1 (1/deg F)	Omega A	Omega B	Henry const.	V inf. (l/mol)
H2S											
CO2											
N2											
CH4						X					
C2H6											
C3H8											
IC4											
NC4											
IC5											
NC5											
FC6											
FC7											
FC8											
FC9											
FC10											
FC11											
FC12											
C13-C16	Grp#1		Grp#2	Grp#3		Grp#4					
C17-C19	Grp#1		Grp#2	Grp#3		Grp#4					
C20-C22	Grp#1		Grp#2	Grp#3		Grp#4					
C23-C25	Grp#1		Grp#2	Grp#3		Grp#4					
C26+	X		X	X		X					

Figure 3.7. Regression process to tune the reservoir fluid.

3.3 RESERVOIR GAS CONDENSATE PROPERTIES

This section introduces the correlations used to estimate the gas deviation factor, gas viscosity, and isothermal compressibility. These gas properties are very important for the well testing and well deliverability calculations to count the change in gas properties with respect to pressure. Laboratory measurement is the most precise way to determine gas properties. However, correlation techniques are an alternative way in the absence of laboratory measurement data. On the other hand, these methods are used to validate the results from the laboratory measurements. The following are the brief definitions of the gas properties that were determined and the correlations methods used for each property.

3.3.1 Gas Deviation Factor. Gas deviation factor is also known as gas compressibility or Z-factor and is defined as the ratio of actual volume at reservoir conditions to the ideal volume at surface conditions (Ahmed, 2000).

The gas deviation factor is the term used most in engineering applications such as estimation gas reserves, design of gas separator, transient pressure analysis in gas wells, and design pipelines for the transmission of produced gas. Several correlations estimate the gas deviation factor, and most of these correlations are functions of pseudo-reduced pressure, (P_{pr}) Equation 3.8, pseudo-reduced temperature, (T_{pr}) Equation 3.9, and gas gravity (γ_g) (McCain, 1991).

$$T_{pr} = \frac{T_R}{T_c} \tag{3.8}$$

$$P_{pr} = \frac{P_R}{P_c} \tag{3.9}$$

Equations 3.10 and 3.11 are pseudo-critical pressure and the pseudo-critical temperature for any hydrocarbon mixture.

For gas condensate reservoirs the specific gravity for well-stream in Equation 3.12 should be used to estimate the gas deviation factor instead of surface gas gravity. Equation 3.13 is the corrected molecular weight for gas condensate systems (Urayet, 2011).

Where:

T_R = Reservoir temperature, (˚R)

P_R = Reservoir pressure, (Psi)

T_{pc} = Pseudo-critical temperature, (˚R)

P_{pc} = Pseudo-critical pressure, (Psi)

$$P_{pc} = \sum_{i=1}^{n} x_i \times P_{ci} \tag{3.10}$$

$$T_{pc} = \sum_{i=1}^{n} x_i \times T_{ci} \tag{3.11}$$

Where:

n = number of components, (#)

x_i = mole fraction of the component, (mole)

P_{ci} = Critical pressure of the component, (Psi)

T_{ci} = Critical temperature of the component, (˚R)

$$\gamma_g = \frac{\gamma_{gs} + R_{cs} \times 4{,}580\, \gamma_{cs}}{1 + 133{,}000 \times R_{cs}\, \frac{\gamma_{cs}}{M_o}} \tag{3.12}$$

$$M_o = \frac{6{,}084}{\gamma_{API} - 5.9} \tag{3.13}$$

If the fluid composition is unknown, the Sutton R.P Equations 3.14 and 3.15 are used to determine pseudo-critical pressure and temperature.

The Wichert and Aziz Equations 3.16 and 3.17 are utilized when impurities are present in hydrocarbon composition in order to correct the values of pseudo-critical pressure and temperature.

Where:

γ_{gs} = Specific gravity of the separator gas, (fraction)

γ_{cs} = Specific gravity of the stock tank condensate, (fraction)

R_{cs} = Gas-oil ratio (Stb condensate/Scf separator gas)

M_o = Molecular weight of the tank oil, (Ib/Ib.mole)

$$P_{pc} = 756.8 - 131(\gamma_g) - 3.6(\gamma_g)^2 \tag{3.14}$$

$$T_{pc} = 169.2 - 349.5(\gamma_g) - 74(\gamma_g)^2 \tag{3.15}$$

$$T'_{pc} = T_{pc} - \varepsilon \tag{3.16}$$

$$P'_{pc} = \frac{P_{pc} \times T'_{pc}}{T_{pc} + B(1-B)\varepsilon} \tag{3.17}$$

Where:

T'_{pc} = Pseudo-critical temperature for gas mixture including the impurities

P'_{pc} = Pseudo-critical pressure for gas mixture including the impurities

ε = Defined using Equation 3.18

$$\varepsilon = 120(A^{0.9} - A^{1.6}) + 15(B^{0.5} - B^4) \tag{3.18}$$

A = Equation 3.19 is the sum of the mole fraction of hydrogen sulfide and carbone dioxide

According to Dr. Urayet, a professor at the University of Tripoli, the Wichert and Aziz correlation proves for Libyan gas fields, and the average absolute error for this correlation around 0.97%. This correlation has accurate results because it works for the gas mixture that has high concentration of carbon dioxide (CO_2).

$$A = X(H_2S) + X(CO_2) \tag{3.19}$$

B = Equation 3.20 is the mole fraction of hydrogen sulfide

$$B = X(H_2S) \tag{3.20}$$

The following is the main correlation that was used in this study to check and validate the gas deviation factor from the constant volume depletion (CVD) test.

1. Brill and Beggs' Method. This method is one of the simplest and most practical correlations to estimate the gas deviation factor. Brill and Beggs presented this correlation in 1974 where the Z-factor values are accurate enough for reservoir engineering applications (Guo et al., 2005). Brill and Beggs' gas deviation factor correlation is expressed using Equations 3.21 to 3.27.

$$A = 1.39\left(T_{pr} - 0.92\right)^{0.5} + 0.36T_{pr} - 0.10 \tag{3.21}$$

$$B = (0.62 - 0.23T_r)P_{pr} + \left[\frac{0.066}{T_r - 0.86} - 0.037\right]P_{pr}^2 + \frac{0.32\,P_{pr}^6}{10^E} \tag{3.22}$$

$$C = 0.132 - 0.32\log T_{pr} \tag{3.23}$$

$$D = 10^F \tag{3.24}$$

$$E = 9\left(T_{pr} - 1\right) \tag{3.25}$$

$$F = 0.3106 - 0.49T_{pr} + 0.1824T_{pr}^2 \tag{3.26}$$

$$Z.Factor = A + \frac{1-A}{e^B} + CP_{pr}^D \tag{3.27}$$

2. Hall and Yarborough Method. This correlation was introduced by Hall and Yarborough in 1973 and is a more accurate correlation to estimate the gas deviation factor (Guo et al., 2005). The correlation is expressed using Equations 3.28 to 3.33

$$t = \frac{1}{T_{pr}} \tag{3.28}$$

$$A = 0.06125\ t\ e^{-1.2(1-t)^2} \tag{3.29}$$

$$B = t(14.76 - 9.76t + 4.58t^2) \tag{3.30}$$

$$C = t(90.7 - 242.2t + 42.4t^2) \tag{3.31}$$

$$D = 2.18 + 2.82t \tag{3.32}$$

$$Z.Factor = \frac{AP_{pr}}{Y} \tag{3.33}$$

Where Y is the reduced density that solves by using Equation 3.34.

$$f(Y) = \frac{Y+Y^2+Y^3-Y^4}{(1-Y)^3} - AP_r - BY^2 + CY^D = 0 \tag{3.34}$$

This non-linear equation solves using numerical techniques, such as the Newton-Raphson iteration method in Equation 3.35.

$$\frac{df(Y)}{dY} = \frac{1+4Y+4Y^2-4Y^3+Y^4}{(1-Y)^4} - 2BY + CDY^{D-1} \tag{3.35}$$

3. Dranchuk & Abou-Kassem's Method. This correlation was presented in 1975 by Dranchuk and Abu-Kassem. The authors proposed an eleven constant, as listed in Table 3.2 in order to calculate the gas deviation factor (Guo et al., 2005). The correlation is summarized in Equation 3.36.

$$Z - Factor = 1 + \left[A_1 + \frac{A_2}{T_r} + \frac{A_3}{T_r^3} + \frac{A_4}{T_r^4} + \frac{A_5}{T_r^5}\right]\rho_r + \left[A_6 + \frac{A_7}{T_r} + \frac{A_8}{T_r^2}\right]\rho_r^2 - A_9\left[\frac{A_7}{T_r} + \frac{A_8}{T_r^2}\right]\rho_r^7 \times A_{10}[1 + A_{11}\rho_r^2]\frac{\rho_r^2}{T_r^3}\ e^{-A^{11}\rho_r^2} \tag{3.36}$$

Where:

ρ_r = Reduced gas density defined in Equation 3.37.

$$\rho_r = \frac{0.27 P_{pr}}{Z\text{-}Factor\ T_{pr}} \tag{3.37}$$

Table 3.2. The coefficients of Dranchuk and Abu-Kassem correlation (Ahmed, 2006).

A	Values
A1	0.3265
A2	-1.0700
A3	-0.5339
A4	0.0157
A5	-0.0517
A6	0.5475
A7	-0.7361
A8	0.1844
A9	0.1056
A10	0.6134
A11	0.7210

4. Averaging Method. In this section, the average simple method was used to have accurate results for the gas deviation factor using Equation 3.38.

$$Z_{avg} = \frac{\sum_{i=1}^{n} Z\text{-}Factor}{n} \tag{3.38}$$

Then, the average value from three correlations was compared to the gas deviation factor from the laboratory measurement.

3.3.2 Gas Viscosity. Gas viscosity is defined as the resistance to flow exerted by the gas. In reservoir engineering applications, the gas viscosity (μ_g) is usually used in centipoises (cp). Due to a high percentage of carbon dioxide (CO_2) contain in the fluid

composition, Lee, Gonzalez, and Eakin numerical correlation was used in order to obtain accurate results.

1. Lee, Gonzalez, and Eakin Correlation. This correlation was introduced in 1966 by Lee, Gonzalez, and Eakin. Many viscosity correlations in petroleum industry have been derived from this correlation. It is one of the most accurate correlations for the calculation of the gas viscosity (Ugwu et al., 2016). The correlation theoretical concept can be expressed in Equation 3.39 to 3.43.

$$\mu_g = 10^{-4}\ K\, exp(X\, \rho^{Y}) \tag{3.39}$$

Where:

$$\rho = 1.4935\ (10^{-3})\ \frac{P_R\, Mw}{Z\, T_R} \tag{3.40}$$

$$K = \frac{(9.379 + 0.01607\, Mw) T_R^{1.5}}{(209.2 + 19.26\, Mw + T_R)} \tag{3.41}$$

$$X = 3.448 + \frac{986.4}{T_R} + 0.01009\, Mw \tag{3.42}$$

$$Y = 2.447 - 0.2224X \tag{3.43}$$

ρ = Gas density, (Ib/ft^3)

P_R = Reservoir pressure, (Psi)

T_R = Reservoir temperature, (^{0}R)

Mw = Molecular weight of the gas mixture, (Ib/gmole)

3.3.3 Isothermal Compressibility. The isothermal compressibility of the gas is defined in Equation 3.44.

$$C = -\frac{1}{V}\frac{dV}{dP} \tag{3.44}$$

Equations 3.45 to 3.47 are the mathematical derivation of the isothermal compressibility (Guo et al., 2005).

$$Cg = -\frac{1}{V}\frac{dV}{dP} = -\frac{P_R}{Z\,n\,R\,T_R}\frac{d}{dP}\left(\frac{Z\,n\,R\,T_R}{P_R}\right) \tag{3.45}$$

$$Cg = -\frac{P}{Z}\left[Z\left(\frac{-1}{P_R^2}\right) + \frac{1}{P_R}\frac{dZ}{dP}\right] \tag{3.46}$$

$$Cg = \frac{1}{P_R} - \frac{1}{Z}\frac{dZ}{dP} \tag{3.47}$$

3.4 GAS WELL TESTING INTERPRETATION

Well testing interpretation in gas wells is more complex than the analysis in oil wells due to the gas properties that are affected by changing pressures. As a result, the equation of pressure transmission through gases in a reservoir porous medium is the nonlinear equation. All of the solutions derived for well-testing interpretation were designed based on slightly compressible filled in reservoirs. However, these solutions are applicable to use in the gas well-testing interpretation by substituting the pressure and time with pseudo-pressure and pseudo-time, as shown in Equation 3.48 (Spivey et al., 2013).

$$\frac{\partial m(P)}{\partial r^2} + \frac{1}{r}\frac{\partial m(P)}{\partial r} = \frac{\emptyset\,\mu\,C_t}{k}\frac{\partial m(P)}{\partial t} \tag{3.48}$$

Equation 3.48 is a linear equation after substituting the pressure by $m(p)$, but the term $\frac{\emptyset\,\mu\,C_t}{k}$ is still a function of pressure. In practice, this remaining nonlinearity is not usually of consequence. It is often permissible to treat the equation as linear, substituting the values of viscosity (μ) and compressibility (Ct) defined at the initial reservoir pressure (Pi) (or at the highest pressure measured during the test if the initial reservoir pressure is not known) (Spivey et al., 2013).

This section focuses on the interpretation of the data for both drawdown and buildup tests from the flow-after-flow test by performing different plot approaches as follows: pressure derivative (log-log) plot as a diagnostic plot to detect the flow regimes, superposition plot (semi-log plot) in order to obtain the reservoir characteristics, type curve analysis for more confident interpretation, and the use of commercial well-testing software (Saphir) to confirm outcomes and obtain deep interpretation results.

3.4.1 Pressure Derivative Plot. The pressure derivative (log-log plot) is a modern method for well-testing interpretation. This technique is a key factor used as a diagnostic to evaluate different parameters such as reservoir permeability, wellbore storage, reservoir boundary, reservoir behavior, and flow regimes. The concept of pressure derivative in transient pressure analysis was first found by Tiab and Kumar in 1980. Since that time, several publications have been presented on the application of using pressure derivative. Bourdet (1989) illustrated how to simplify the analysis to make the well-testing interpretation more precise and easy. Nowadays, the Bourdet pressure derivative is used in all commercial well-testing software analysis, including Kappa Saphir.

Before the pressure derivate is discussed, the main input parameters are introduced in the following sections.

3.4.1.1 Single-phase pseudo-pressure. Single-phase pseudo-pressure is essential in transient pressure analysis gas reservoirs because of change in the gas properties with pressure. As a result, this method is used to account for the variable compressibility and viscosity of gas with respect to pressure. This technique was introduced by Al-Hussainy and Ramey in 1966. The pseudo-gas potential pressure is defined in Equation 3.49. This method is used only when a single phase is present in the reservoir. Therefore, if condensate

is present, it is assumed that its saturation is below the critical gas saturation, meaning the condensate is immobile. The impact of the condensate on the relative permeability curve is negligible (Raghavan et al., 1995).

$$m(p) = 2\int_{p_0}^{p_{ref}} \frac{p}{\mu_g \; z_g} \; dp \tag{3.49}$$

Where:

$m(p)$ = Pseudo-gas potential pressure, (Psi^2/cp)

Z = Gas deviation factor, (Unit-less)

μ = Gas viscosity, (cp)

p_0 = Based pressure that usually is the lowest pressure (surface pressure condition) of the range of pressures during the test, (Psi)

p_{ref} = Reference pressure that usually is the initial pressure (p_i), (Psi)

The PVT-fluid properties were determined and validated in the section of the reservoir gas condensate properties, where the trapezoidal method has been used by these properties in Equation 3.50 to obtain pseudo-gas potential pressure.

$$m(p) = 2\sum_{i=2}^{n} \frac{1}{2}\left[\left(\frac{p}{\mu\, z}\right)_{i-1} + \left(\frac{p}{\mu\, z}\right)_{i}\right](p_i - p_{i-1}) \tag{3.50}$$

3.4.1.2 Adjusted pressure. Unfortunately, the real gas pseudo-pressure unit is a function of Psi^2/cp, which is the magnitude on the order of 10^9 Psi^2/cp for a pressure of 5,000 psi (Spivey et al., 2013). For convenes unit, the adjusted pressure in Equation 3.51 is normalized from the real gas pseudo-pressure (Meunier et al., 1987).

$$(p_a) = \frac{\mu(p_{ref})\times Z(p_{ref})}{2\; p_{ref}} m(p) \tag{3.51}$$

Where:

p_a = Adjusted pressure, (Psi)

3.4.1.3 Pseudo-time and adjusted time. Agarwal introduced pseudo-time in 1979, and later Lee and Holditch described pseudo-time use in 1982. Agarwal's pseudo-time is defined in Equation 3.52.

$$t_{pseudo} = \int_0^t \frac{1}{\mu\ C_t} dt \tag{3.52}$$

The Agarwal definition of pseudotime does not have a unit of time, which makes the data plots more difficult for visual examination. As a result, Meunier et al. (1987) normalized the Agarwal equation to have the time unit, called the adjusted time, as defined in Equation 3.53.

$$t_a = \mu_i\ C_{ti} \int_0^t \frac{1}{\mu\ C_t} dt \tag{3.53}$$

Where:

t_a = Adjusted time, (hrs)

t_{pseudo} = Pseudo-time, (unitless)

μ_i = Gas viscosity at the reference pressure, (cp)

C_{ti} = Gas compressibility at the reference pressure, (Psi^{-1})

3.4.1.4 Superposition in time. The principle of superposition is a powerful concept used to solve complex cases in both pressure transient analysis (PTA) and rate transient analysis (RTA). In this thesis, the superposition approach is utilized for the multi-rate production case, which is used to convert the multi-rate production to an equivalent single rate model. Figure 3.10 shows the pressure drop response at the time n that can be defined in Equation 3.54.

ΔP = pressure drop from the well due to q_i throughout the entire flow period (flow time=t_n) + pressure drop from the well producing at (q_{i+1}-q_i), commencing at the time t_i (flow

time=t_n-t_i) + pressure drop from the well producing at (q_n-q_{i+1}), commencing at the time t_{i+1} (flow time = t_n-t_{i+1}). Therefore, as shown in Figure 3.8, the total pressure drop is defined as follows:

$$\Delta P = \Delta P_i + \Delta P_{i+1} + \Delta P_n \tag{3.54}$$

Superposition in time for the buildup test and multi-rate test is defined in Equation 3.55.

$$Sup(\Delta t_i) = \sum_{i=1}^{n-1} \left[\frac{q_i - q_{i-1}}{q_n - q_{n-1}} \times \log[t_n - t_i + \Delta t_i] + \log \Delta t_i \right] \tag{3.55}$$

Where:

$Sup(\Delta t_i)$ = superposition time at certain time during the test, (hrs)

q_i = flow rate at certain period, (MMscf/day)

q_n = last flow rate before the buildup test, (MMscf/day)

t_i = the time during the period of first flow rate, (hrs)

t_n = the final time until the buildup test starts, (hrs)

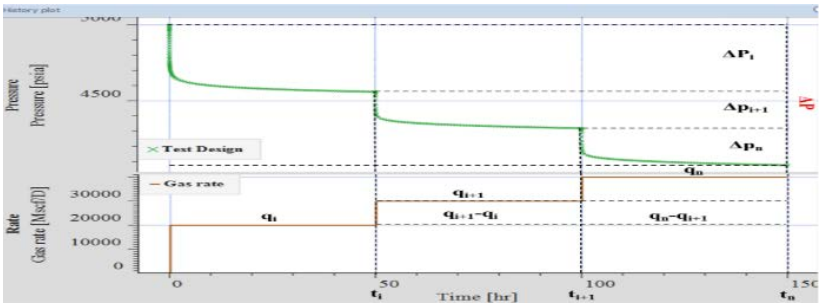

Figure 3.8. Multi-rate flow profile and pressure response due to different rates (modified from Liang et al., 2013).

3.4.1.5 The Bourdet derivative. In this thesis, the Bourdet pressure derivative technique is used in both drawdown and buildup analysis. This technique computes the

derivative from the slope points in the semi-log plot where the x-axis is the natural log of time and the y-axis is the pressure, as shown in Figure 3.9.

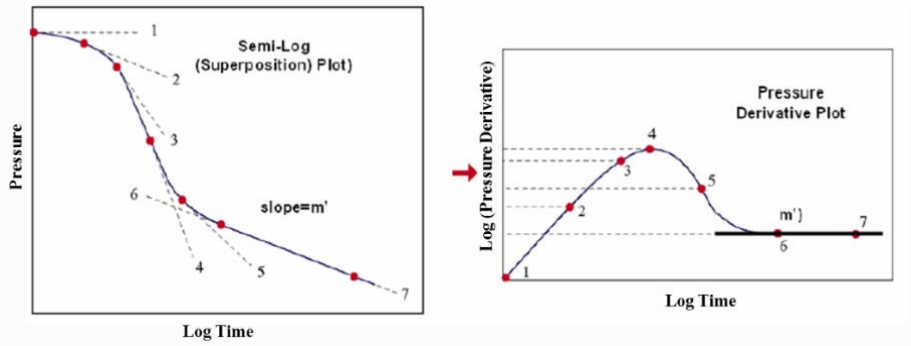

Figure 3.9. Bourdet derivative, semi-log and log-log (Dynamic Flow Analysis, Kappa, 2012).

Equations 3.56 and 3.58 are simple and standard techniques to determine the pressure derivative for the buildup and drawdown analysis.

For a drawdown:

$$\Delta p' = \frac{d\Delta p}{d\ln(\Delta t)} = \Delta t \frac{d\Delta p}{d\Delta t} \tag{3.56}$$

Where:

$$\Delta p = p_i - p_{wf}(\Delta t) \tag{3.57}$$

For buildup and multi-rate:

$$\Delta p' = \frac{d\Delta p}{d\sup(\Delta t)} \tag{3.58}$$

$$\Delta p = p_{ws}(\Delta t) - p_{wf}(tp) \tag{3.59}$$

Where:

Equations 3.57 and 3.59 are the pressure drop for the buildup and drawdown analysis, respectively.

Where:

$\Delta p'$ = Pressure derivative, (unitless)

Δp = Pressure drop, (Psi)

Δt = Time, (hrs)

tp = Production time, (hrs)

p_{wf} = Bottomhole flowing pressure, (Psi)

p_{ws} = Shut-in pressure, (Psi)

$sup(\Delta t)$ = Superposition time, (hrs)

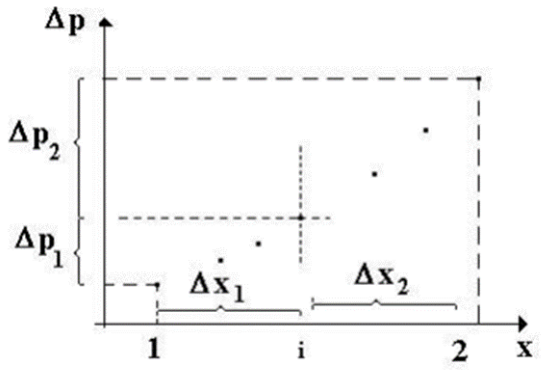

Figure 3.10. Schematic of Bourdet derivative algorithm (Dynamic Flow Analysis, Kappa, 2012).

$$\Delta p' = \frac{\left(\frac{\Delta p_1}{\Delta x_1}\Delta x_2 + \frac{\Delta p_2}{\Delta x_2}\Delta t x_1\right)}{\Delta x_1 + \Delta x_2} \tag{3.60}$$

Equation 3.60 was used for the interpretation in this thesis because the real data needs more smoothing due to the noisy pressure data during the test operation. Figure 3.10

illustrates the Bourdet derivative algorithm that is widely used by commercial software for the well-testing interpretations.

3.4.2 Type Curve Analysis. Type curve is a powerful technique used for both drawdown and buildup analysis. The type curve shows the dimensionless pressure function versus the dimensionless time function that are the solutions of the flow equation (diffusivity equation). The following are the most common used log-log type curve: Agarwal, Al-Hussainy, and Ramey (1970), Earlougher and Kersch (1974), Gringarten, Ramey, and Rhagavan (1974), and finally, Gringarten and Bourdet (1979).

In this thesis, the Gringarten and Bourdet type curve, as shown in Figure 3.11, was utilized for the analysis in order to determine the reservoir permeability, skin, and wellbore storage.

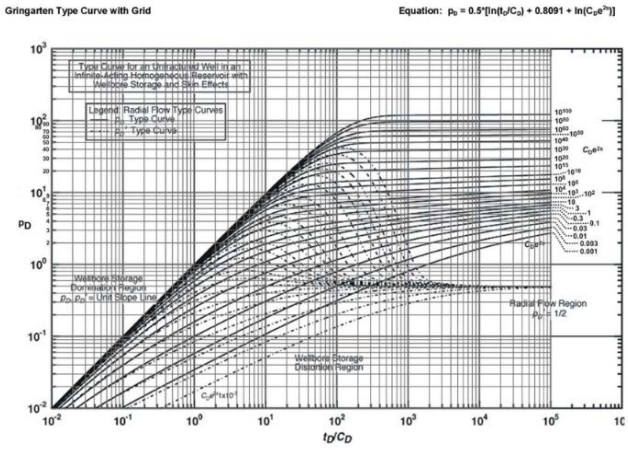

Figure 3.11. Gringarten and Bourdet type curve (Gringarten et al., 1979).

3.4.3 Interpretation procedures. The flow-after-flow tests were conducted in the North African field in 2009 and 2014. This type of test consists of four drawdown tests

and one buildup test. This section basically focuses on the analysis of the test in 2009. Consecutively, the same procedure can be used for the test in 2014. The following steps are the preparing the data for the analysis, and then the buildup test was analyzed using pressure derivative and superposition plot and type curve analysis.

1. The transient pressure data were gathered and filtrated for certain periods of time steps to avoid repeating the same value of pressure.
2. In filtration process for the pressure range, the time interval should be consistent with each step. For example, the first time interval was 60 sec, followed by a 90 sec time period, etc.
3. An Excel spreadsheet was created, and the pressure, time, and flow rates were entered as input-data for the analysis.
4. The gas flow rate for each drawdown was corrected by counting the condensate flow rate to determine the equivalent flow rate in Equation 3.61.

$$q_{gc} = q_{gs} + q_c \times 3{,}003 \times (1.03 - \gamma_c) + q_w \times 7{,}390 \qquad (3.61)$$

Where:

q_{gc} = Equivalent gas flow rate, (MMscf/day)

q_{gs} = Gas flow rate, (MMscf/day)

q_c =Condensate flow rate, (Rbbl/day)

q_w = Water flow rate, (Rbbl/day)

γ_c = Condensate specific gravity, (unitless)

5. Before the analysis began, the equivalent flow rates were checked using derivative overlay, as shown in Figure 3.12. This technique was used in order to have one mutual infinite acting radial flow (IARF) for four drawdowns.

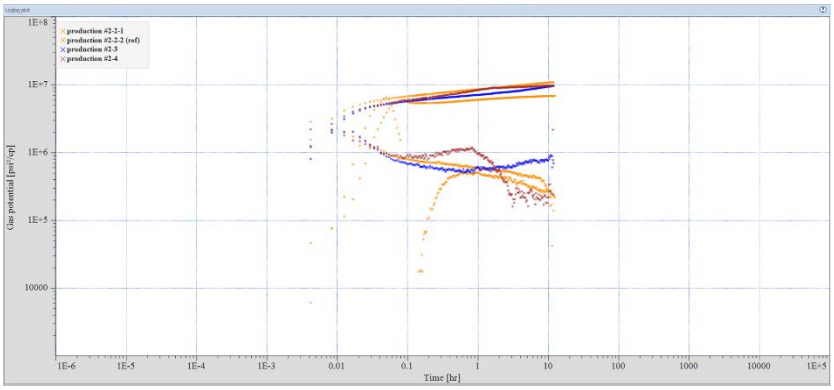

Figure 3.12. Derivative overlay for four drawdowns before adjusted flow rates.

6. If not, the equivalent flow rates were adjusted until four drawdown pressure derivatives overlaid each other, as shown in Figure 3.13.

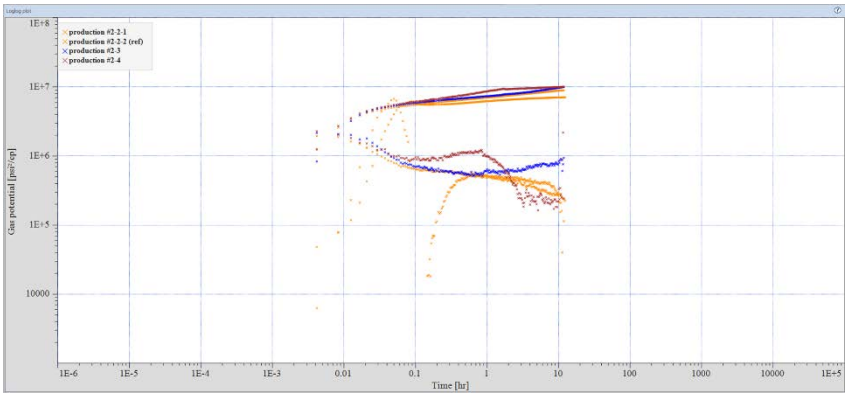

Figure 3.13. Derivative overlay for four drawdowns after adjusted flow rates.

7. After the overlay process, the pressure derivative and superposition plot method was used, followed by Gringarten type curve method for more confident and accurate results.

3.4.4 Pressure Derivative and Superposition Plot.

1. Superposition in time, pressure derivative, and pressure drop were determine in order to perform the pressure derivative for buildup test, as shown in Figure 3.14.

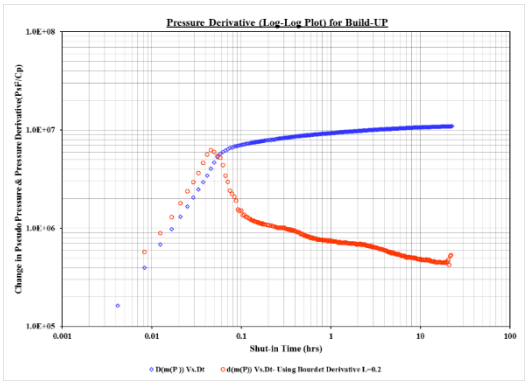

Figure 3.14. Pressure derivative plot for buildup test.

2. The radial flow regions were detected on the plot, as shown in Figure 3.15. These regions are important to determine the reservoir permeability.

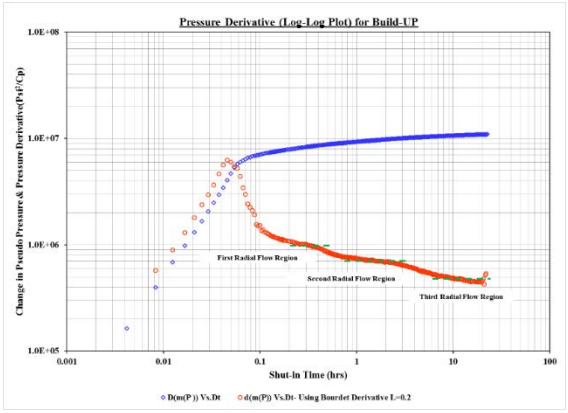

Figure 3.15. Radial flow regions on the pressure derivative plot.

3. Then, a superposition plot was created by plotting the pseudo-gas pressure and superposition in time on the semi-log plot in order to determine the slope of each radial flow region. After that, permeability and skin factor at each region were calculated using Equations 3.62 and 3.63.

$$K = \frac{162.6\, q_{gc}\, \beta_g\ \mu_g}{|m|h} \tag{3.62}$$

Where:

m = Slope, (psi^2/cp/cycle)

K = Reservoir permeability, (md)

q_{gc} = Equivalent gas flow rate, (MMscf/day)

β_g = Gas formation volume factor, (ft^3/scf)

μ_g = Gas viscosity, (cp)

h = Net pay thickness, (ft)

$$S = 1.151\left[\frac{m(p_{wf_o)} - m(p_{1hr})}{|m|} - \log\left(\frac{k}{\varphi\mu c_t r_w^2}\right) + 3.23\right] \tag{3.63}$$

Where:

S = Skin factor, (unitless)

$m(p_{wfo})$ = Pseudo-gas pressure at zero time, (psi^2/cp)

$m(p_{1hr})$ = Pseudo-gas pressure at one hour, (psi^2/cp)

$\emptyset$ = Porosity, (fraction)

C_t = Total compressibility, (psi^{-1})

r_w = Wellbore radius, (ft)

3.4.4.1 Gringarten type curve.

1. The adjusted pressure and superposition in time were plotted on the log-log scale, then overlaid on the Gringarten type curve.
2. The scale for both the pressure derivative and Gringarten type curve should be consistent, which means both plots should have the same cycle numbers in the x-axis and y-axis.
3. The derivative plot was moved over the Gringarten type curve until the match of the radial flow region was reached, as shown in Figure 3.16.
4. Then, the main points were picked on the plot where certain superposition in time and pressure drop overlay dimensionless time (t_D) and dimensionless pressure(p_D), as indicated in Figure 3.16 by the red arrows, and listed in Table 3.3.

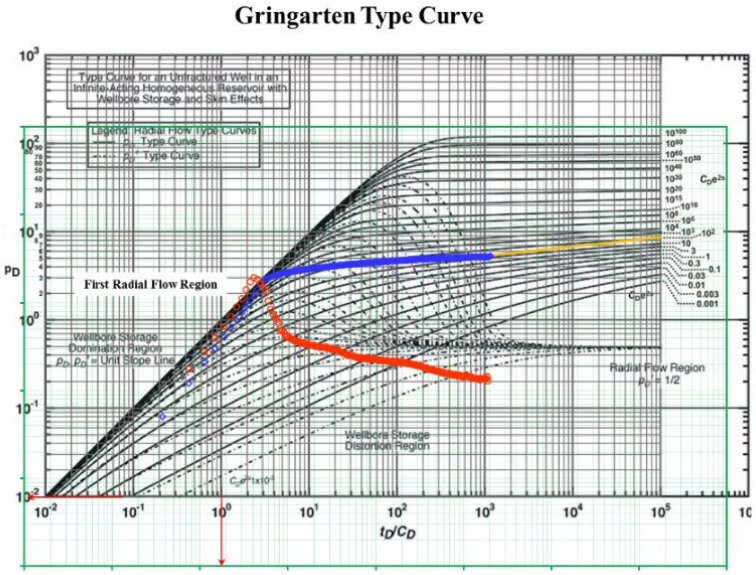

Figure 3.16. Gringarten type curve for the first radial flow region.

Table 3.3. The main input of the first region for the Gringarten type cure approach.

First Region		
Dt	5.790E-02	hrs
DP	17.719	Psi
$(\Delta ta)_m$	1.75E-02	hrs
$(\Delta P)_m$	6.05E-02	Psi
$(tD/CD)_m$	1.E+00	-
$(PD)_m$	1.E-02	-

5. These parameters were used in Equations 3.64 to 3.67 in order to calculate the reservoir permeability, dimensionless wellbore storage coefficient (C_D), wellbore storage coefficient (C), and skin factor.

$$K = \frac{q_{gc}\ \beta_g\ \mu_g}{0.00708\ h}\left(\frac{p_D}{\Delta_p}\right) \tag{3.64}$$

$$C_D = \frac{0.0002637\ K}{\varphi \mu c_t r_w^2}\left(\frac{t}{t_D/C_D}\right) \tag{3.65}$$

$$C = \frac{\varphi h c_t r_w^2}{0.894}\ C_D \tag{3.66}$$

$$S = 0.5 \ln\left(\frac{C_D\ e^{2s}}{C_D}\right) \tag{3.67}$$

6. Steps 3 and 4 were repeated two times for second radial flow region and third radial flow region, as shown in Figure 3.17 and 3.18, and the input parameters are listed in Table 3.4.

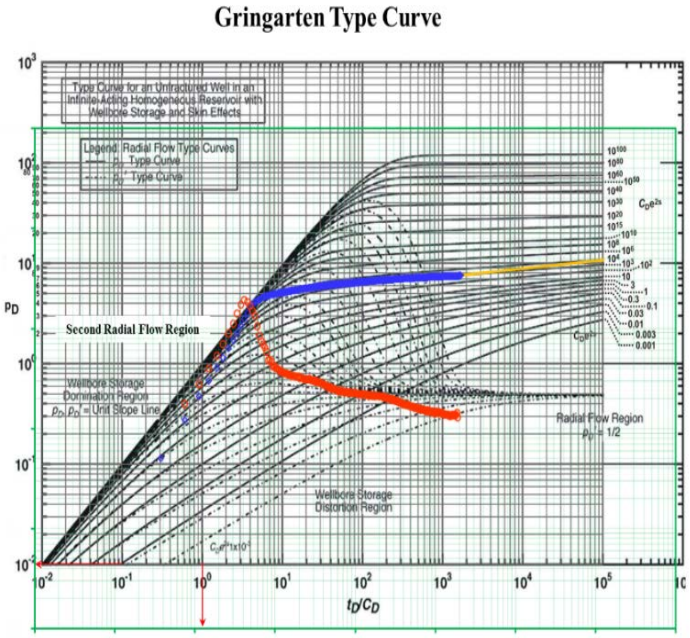

Figure 3.17. Gringarten type curve for the second radial flow region.

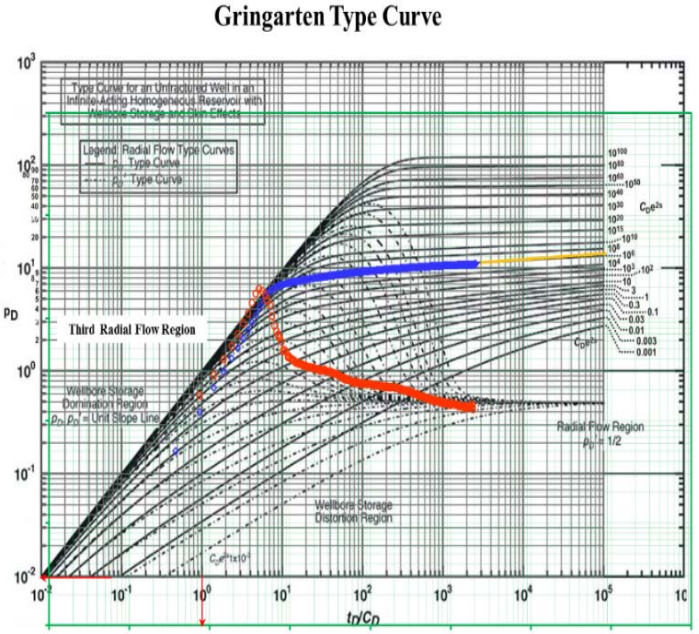

Figure 3.18. Gringarten type curve for the third radial flow region.

Table 3.4. The main input of the second and third regions for the Gringarten type cure approach.

Parameter	Second Region	Third Region	Unit
Dt	5.790E-02	5.790E-02	hrs
DP	17.719	17.719	Psi
$(\Delta ta)_m$	1.05E-02	8.20E-03	hrs
$(\Delta P)_m$	4.38E-02	2.95E-02	Psi
$(tD/CD)_m$	1.E+00	1.E+00	-
$(PD)_m$	1.E-02	1.E-02	-

3.4.4.2 Kappa Saphir software. Kappa engineering package consists of several software related to reservoir and production engineering applications. In this thesis, Saphir software was utilized for the analysis of transient pressure data because it is widely used by most companies in petroleum industry. The following are step-by-step procedures that introduce how to interpret the well-testing data using Saphir software.

1. The reservoir data were entered in the analysis information window, as shown in Figure 3.19.

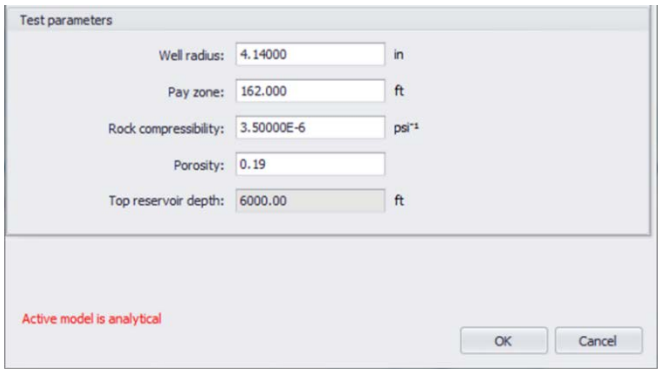

Figure 3.19. The main reservoir parameters.

2. PVT data were imported into the software where the PVT-P file was used to define the reservoir fluid properties, as shown in Figure 3.20.

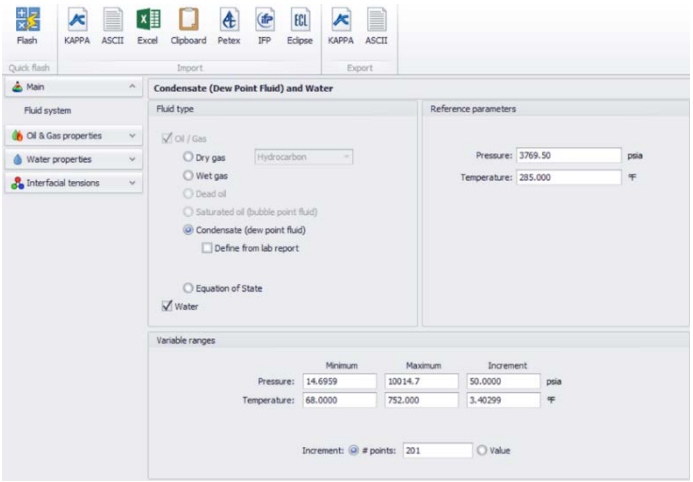

Figure 3.20. PVT data.

3. The pressures, time, and flow rates were imported into the software. Then, the data was synchronized in the edit rate and pressure (QAQC) section in order to have accurate interpretation.
4. The flow-after-flow data were divided into drawdowns data and buildup data, where the analysis was started with drawdown analysis in order to obtain the skin factor for each drawdown period.
5. Skin factors were used to determine the non-Darcy flow coefficient.
6. The pressure derivative was extracted for the first drawdown, and then the analytical model was used to match the model line represented in red with the actual data.
7. Because the early data did not fall on the unit slope, and this behavior is defined by changing wellbore storage, Hegeman model was used to have precise results.

8. Figure 3.21 shows the first drawdown pressure derivative where the software model matched the actual data perfectly.

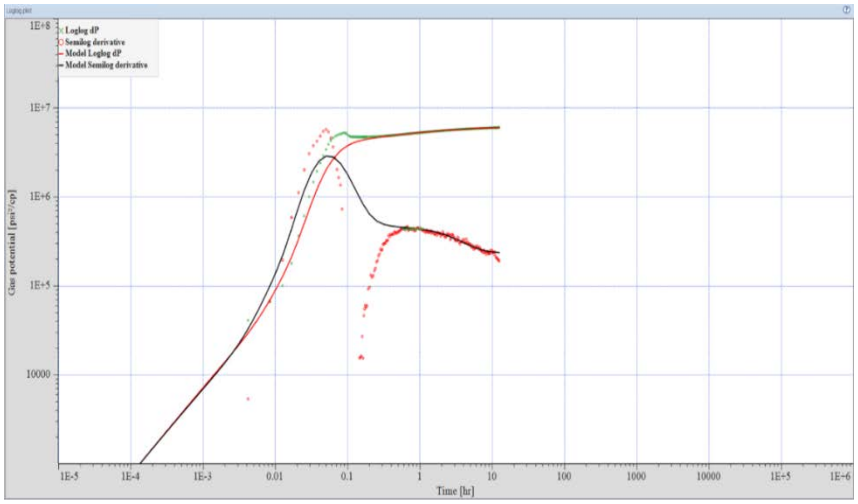

Figure 3.21. The interpretation for the first drawdown.

9. Steps 5 and 6 were repeated for the second, third, and fourth drawdown in order to have a perfect match, as shown in Figure 3.22, 3.23, and 3.24.

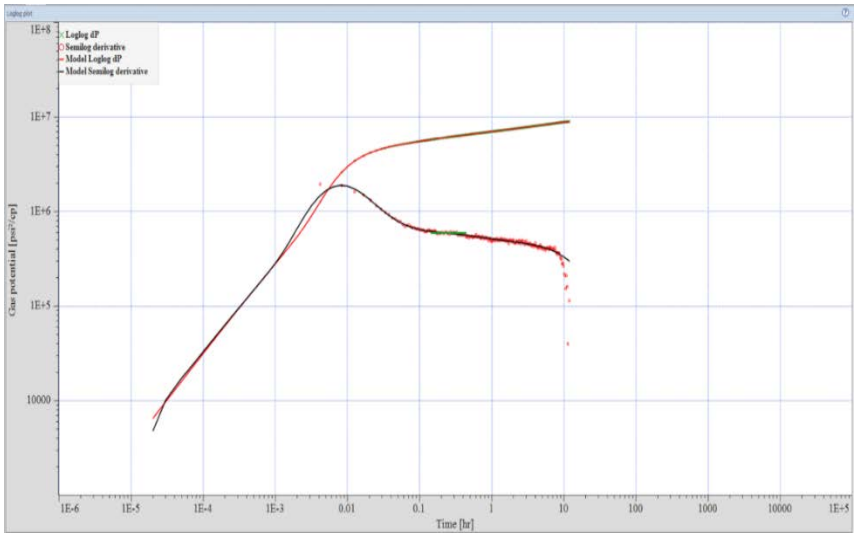

Figure 3.22. The interpretation for the second drawdown.

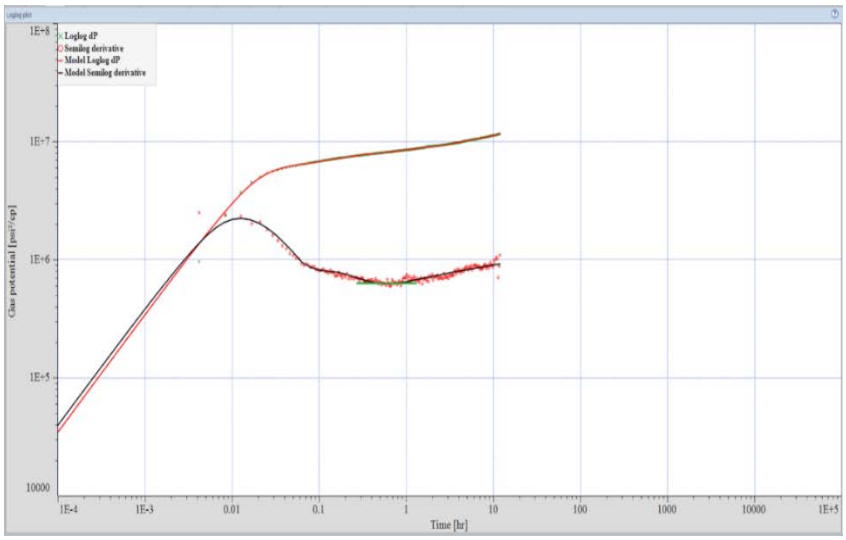

Figure 3.23. The interpretation for the third drawdown.

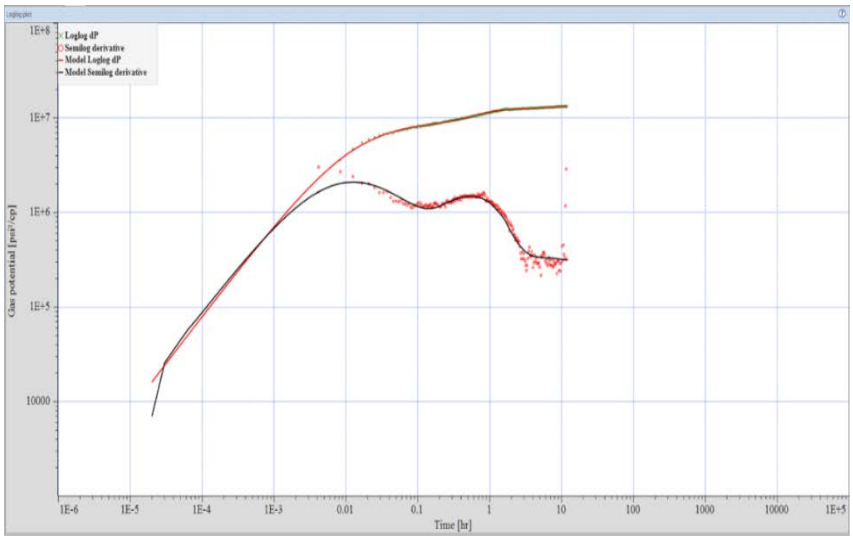

Figure 3.24. The interpretation for the fourth drawdown.

10. The same analysis was done for the buildup test in order to obtain the reservoir permeability and average reservoir pressure and confirm the results obtained from the drawdown analysis.

11. Figure 3.25 illustrates the analysis of the buildup test where the second and third radial flow regions were matched perfectly.
12. In order to determine the non-Darcy coefficient flow that is an important parameter with skin and permeability to match the pressure test with the model, there are two methods: rate-dependent skin or time-dependent skin.

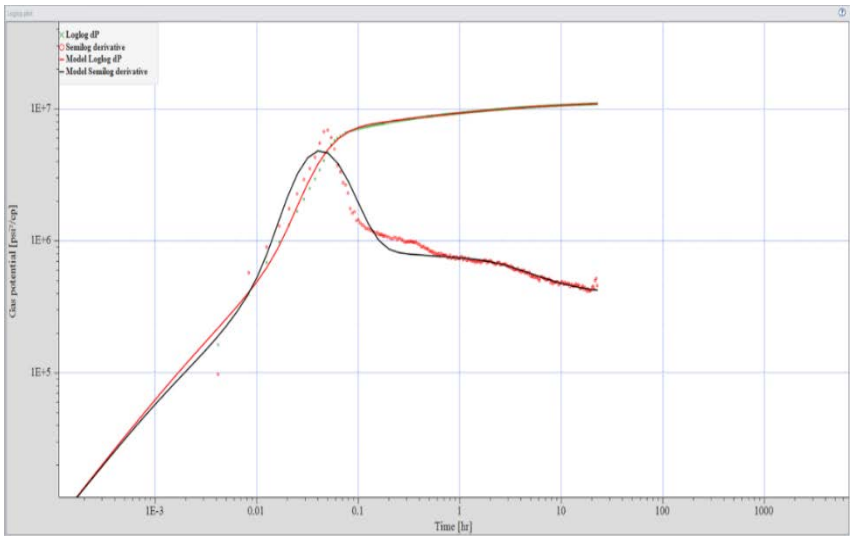

Figure 3.25. The interpretation for the buildup.

13. The rate-dependent skin was first used where the four drawdown overlaid together, as shown in Figure 3.26, and the mutual radial flow region was selected in order to perform the skin versus gas flow rate plot.
14. Figure 3.27 shows the skin versus gas flow rate where the non-Darcy coefficient flow was obtained.
15. The history pressure improvement was run to match the model with the flow-after-flow test, as shown in Figure 3.28.

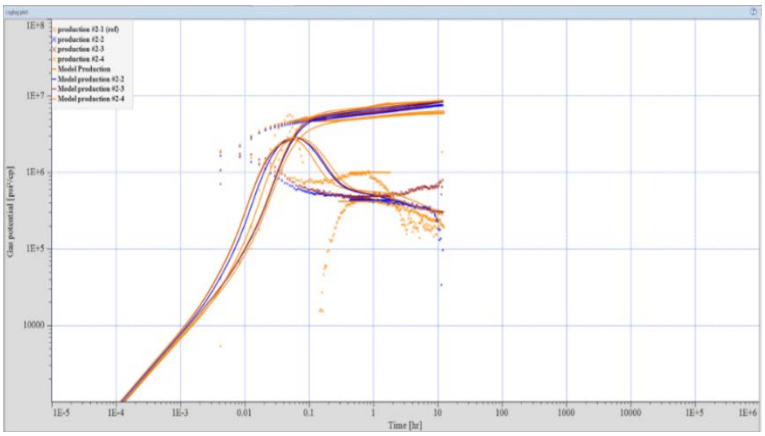

Figure 3.26. Derivative overlay for the four drawdowns.

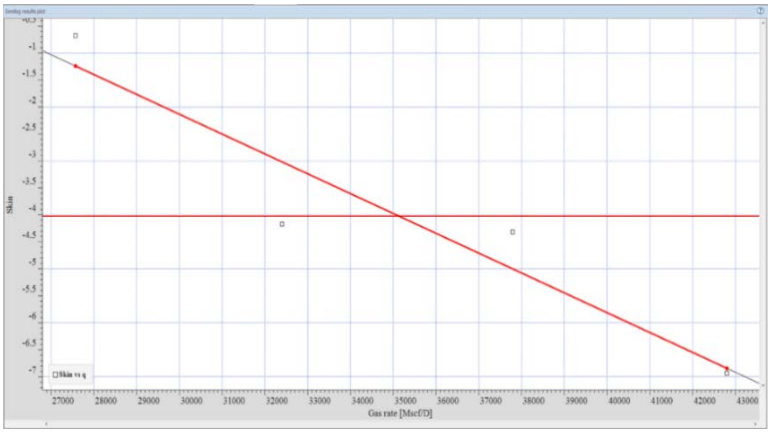

Figure 3.27. Rate-dependent skin plot.

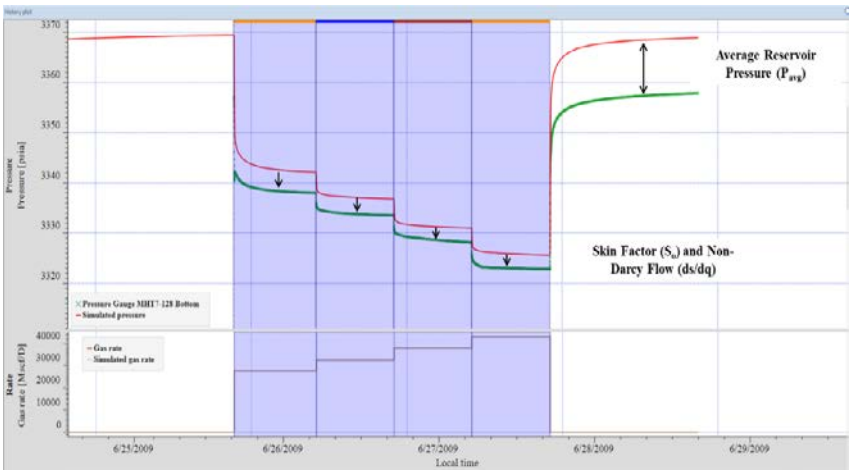

Figure 3.28. The history pressure before reaching the match using rate-dependent skin.

16. In order to improve the match, the average reservoir pressure and skin factor at the zero flow rate and non-Darcy flow coefficient were modified until the match was reached, as shown in Figure 3.29.

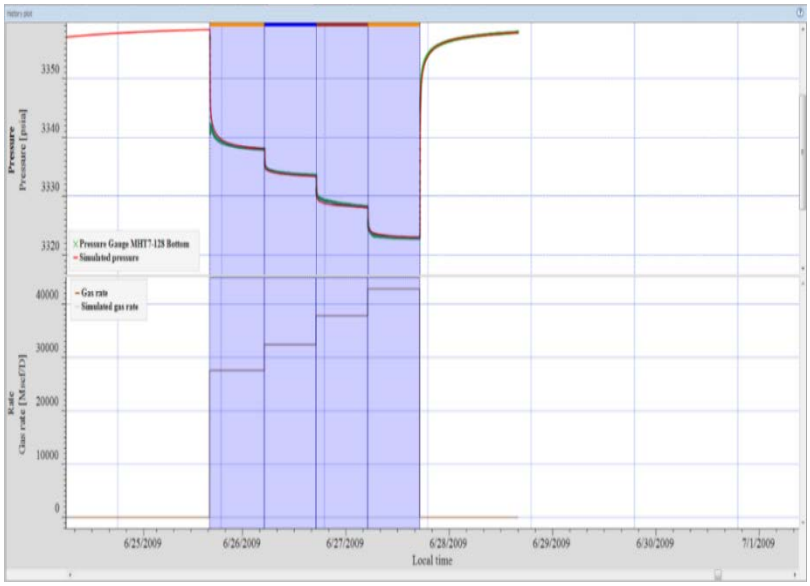

Figure 3.29. The history pressure after reaching the match using rate-dependent skin.

3.5 WELL DELIVERABILITY

The well deliverability calculations were used in this research based on the back-pressure equations where three equations were utilized to determine the absolute open flow (AOF) potential and performed the inflow performance relationship (IPR). This research studied two flow-after-flow tests in 2009 and 2014, where this section focuses on the interpretation of the test in 2009. The same analysis was used for the test in 2014. The following step-by-step procedures to determine the deliverability for the well A7 using Excel, Kappa Saphir software, and Prosper software.

3.5.1 Excel Sheet Calculation.

1. The bottomhole flowing pressure points for each drawdown test were picked from the stabilization period at the end of each drawdown test, as shown in Figure 3.30 by the red circle.
2. Table 3.5 lists the bottomhole flowing pressure versus equivalent gas flow rate in each drawdown.

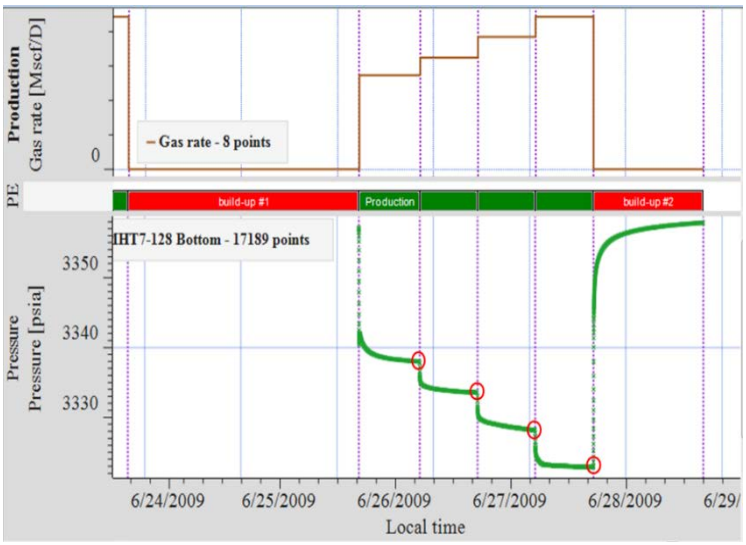

Figure 3.30. Flow-after-flow test.

Table 3.5. Main input data for the deliverability calculations.

Test	Flowing Pressure	Equivalent Gas Flow Rate
#	Psi	MM Scf/day
0	3,359.10	0
1	3,338.00	27.57
2	3,333.55	32.40
3	3,328.15	37.79
4	3,322.86	42.80

3. The pressure at test number zero is the average reservoir pressure that has been determined from well-testing interpretation using Saphir software.
4. The first method of backpressure equations is the empirical method that was used as described in the following.
   a. Calculate the pressure difference squared between the flowing pressure at each test and the average reservoir pressure, as listed in Table 3.6.

Table 3.6. Input calculation data in the empirical method.

Test #	P_{avg}^2-P_{wf}^2 Psi^2	Test #	P_{avg}^2-P_{wf}^2 Psi^2	Test #	P_{avg}^2-P_{wf}^2 Psi^2
0	0.00E+00	2	1.71E+05	4	2.42E+05
1	1.41E+05	3	2.07E+05	-	-

   b. Plot the data points on the log-log scale, where the x-axis represents the equivalent gas flow rate and the y-axis represents the pressure difference squared, as shown in Figure 3.31.
   c. The n and C values were determined from the extrapolated line equation or by using the empirical Equation 3.68.

$$q_g = C \times \left(P_{avg}^2 - P_{wf}^2\right)^n \tag{3.68}$$

   d. Absolute open potential flow was obtained using the empirical method plot, as shown in Figure 3.32, or using Equation 3.69 by assuming the flowing bottomhole pressure is 14.7 psi.

Where:

q_g = Equivalent gas flow rate, (MMscf/day)

P_{wf} = Bottomhole flowing pressure, (psi)

P_{avg} = Average reservoir pressure, (psi)

n = Performance exponent constant, (unitless)

C = Inflow (or performance) coefficient, (MMscf/day/psi^2)

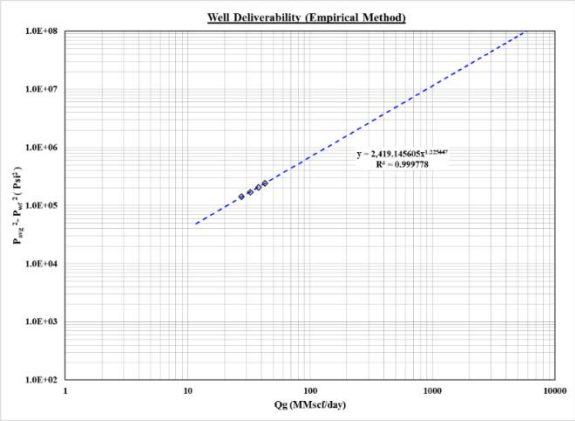

Figure 3.31. Deliverability calculation (empirical method).

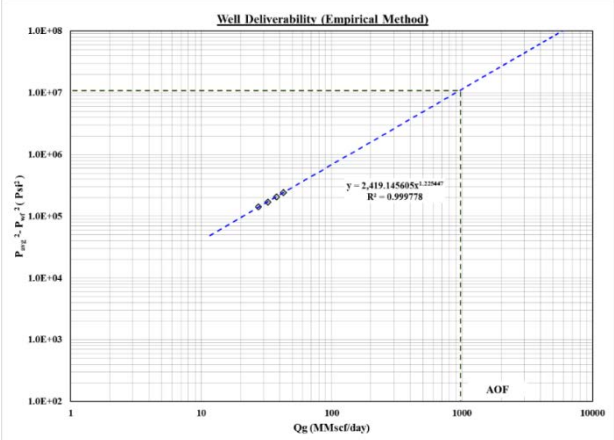

Figure 3.32. Deliverability calculation (empirical method).

e. The equation was used to determine the gas flow rates at wide range of pressures in order to contrast the inflow performance relationship plot (IPR).

$$q_g = C \times \left(P_{avg}^2 - 14.7^2\right)^n \quad (3.69)$$

5. The second method of backpressure equations is the theoretical (modified) method that was used as described in the following steps.

a. The pressure difference squared was calculated between the flowing pressure at each test and the average reservoir pressure and then divided by the equivalent gas flow rate at each test, as listed in Table 3.7.

Table 3.7. Input calculation data in the theoretical method.

Test	P_{avg}^2-P_{wf}^2/Q_g
#	Psi^2/ MM Scf/day
0	0.00E+00
1	5.13E+03
2	5.28E+03
3	5.48E+03
4	5.66E+03

b. The data points on the Cartesian scale were plotted, where the x-axis represents the equivalent gas flow rate and y-axis represents the pressure difference squared divided by the equivalent gas rate at each test, as shown in Figure 3.33.

c. The a and b values were obtained from the extrapolated line equation or by using Equation 3.70 or Equation 3.71.

d. Solver function in Excel was used in order to obtain the value of absolute open flow (AOF) potential.

$$P_{avg}^2 - P_{wf}^2 = a.q_g + b.q_g^2 \quad (3.70)$$

$$\frac{P_{avg}^2 - P_{wf}^2}{q_g} = a. + b.q_g \quad (3.71)$$

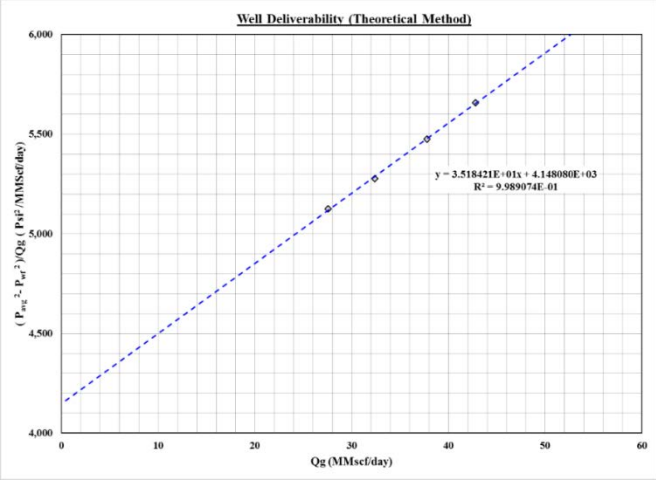

Figure 3.33. Deliverability calculation (theoretical method).

6. The final method of backpressure equations is the exact (pseudo-gas potential) method that depends on the pseudo-gas potential pressures in its calculation instead of using the normal pressures. The following are the steps that were utilized in the exact method calculations.

   a. The normal pressure at each test number was converted to pseudo-gas potential pressure using the equation that resulted from the single-phase calculation (Equation 3.50).

   b. The pseudo-gas potential pressure difference was calculated between the flowing pseudo-gas potential pressure at each test and the average pseudo-gas potential

reservoir pressure and then divided by the equivalent gas flow rate at each test, as listed in Table 3.8.

Table 3.8. Input calculation data in the exact method.

Test #	$[m(P_{avg})-m(P_{wf})]/Q_g$ Psi^2/CP	Test #	$[m(P_{avg})-m(P_{wf})]/Q_g$ Psi^2/CP
0	0.00E+00	4	2.67E+05
1	2.41E+05	-	-
2	2.49E+05	-	-
3	2.58E+05	-	-

c. The data points on the Cartesian scale were plotted where the x-axis represents the equivalent gas flow rate and y-axis represents the difference between the flowing pseudo-gas potential pressure at each test and the average pseudo-gas potential reservoir pressure divided by the equivalent gas flow rate at each test, as shown in Figure 3.34.

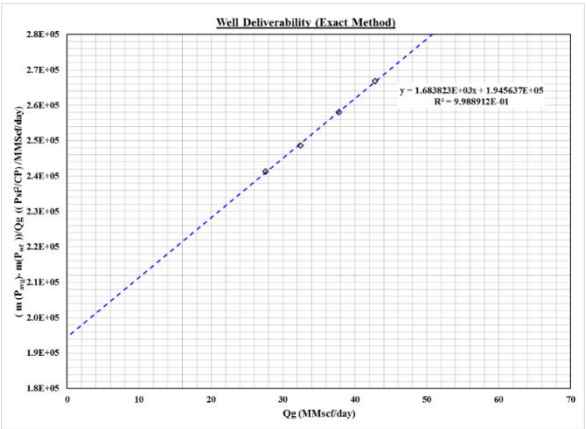

Figure 3.34. Deliverability calculation (Exact method).

d. The A and B values were determined from the extrapolated line equation or using Equation 3.72 or Equation 3.73.

$$m(P_{avg}) - m(P_{wf}) = A.q_g + B.q_g^2 \quad (3.72)$$

$$\frac{m(P_{avg}) - m(P_{wf})}{q_g} = A + B.q_g \quad (3.73)$$

e. Solver function in Excel was used in order to obtain the value of absolute open flow (AOF) potential.

The same analysis for the deliverability test can be done using production performance software package to have accurate and more confident results. The inflow performance relationship was performed using Prosper software (Petroleum Expert package).

3.5.2 Prosper Software. In order to build the nodal analysis model for a total production system, Prosper software is the best tool and is widely used in the petroleum industry for different production applications. The software was used to perform the inflow reservoir performance relationship (IPR) with the outflow system for the well (VLP). The following are the main procedures for the well performance nodal analysis model by using Prosper software:

1. The PVT model that has been built by using the WINPROP compositional simulation model was imported to the Prosper software to define the fluid system and properties.
2. A deviation survey was defined where the data for measured depth, true vertical depth, and deviation angle were imported into the software.

3. The previous step and the downhole equipment are very important for the outflow calculation that defined the main parameters, as shown in Figure 3.35, where the tubing size is 4.5 in and the mid-production zone depth is 8,888 ft.
4. The geothermal gradient data was imported by defining the temperature distribution throughout the depth as listed in Table 3.9.
5. The average heat capacities for oil, gas, and water were entered, as mentioned in Table 3.10.

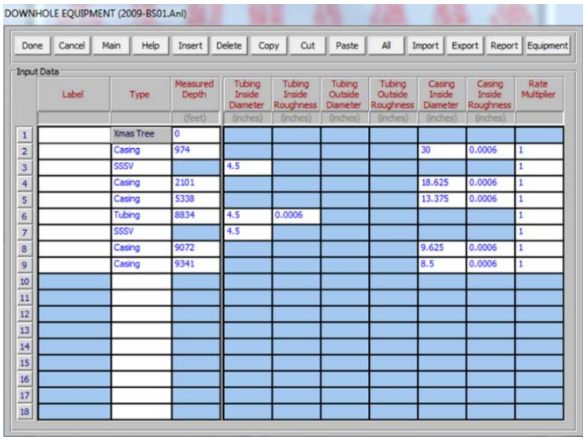

Figure 3.35. Downhole equipment.

Table 3.9. Geothermal gradient data.

Depth (ft)	Temperature (°F)
0	60
9,341	285

Table 3.10. Average heat capacities (Petroleum expert manual).

Fluid	Average heat capacities (BTU/Ib/°F)
Oil	0.53
Gas	0.51
Water	1

6. The software includes several types of methods for well deliverability analysis. However, this research focuses on the multi-rate calculations that include the backpressure approach.
7. From the inflow performance relationship (IPR) section, the multi-rate approaches were selected to contract the IPR curve.
8. Prosper software approach names are different than previous methods, but the equations and analysis are the same as the Excel and Saphir software.
9. Prosper software names the empirical, theoretical, exact methods as follows: multi-rate (C) and (n) , multi-rate Jones, and multi-rate Forchheimer with pseudo gas potential pressure, respectively.
10. These methods were utilized to determine the main parameters and perform the inflow performance relationship (IPR).
11. The tubing curve was performed from the calculation section in Prosper software, where the correlations and the input-data were entered, as shown in Figure 3.36.

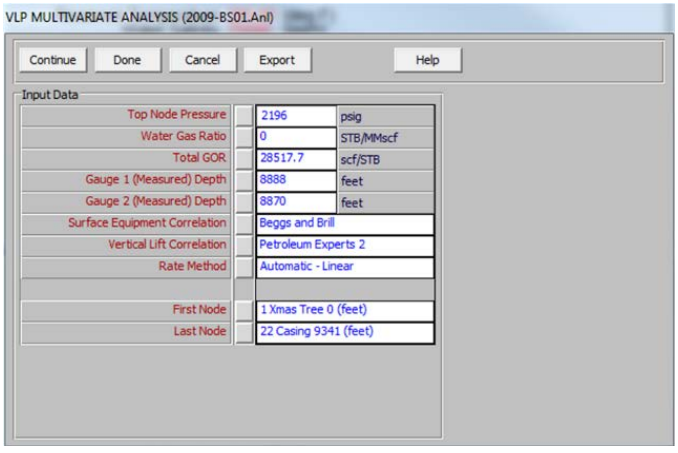

Figure 3.36. Vertical lift pressure input-data.

12. After the model was run, the vertical lift pressure system was created, as shown in Figure 3.37.
13. The vertical lift pressure system was performed in order to match with three methods of the inflow performance relationship curves.

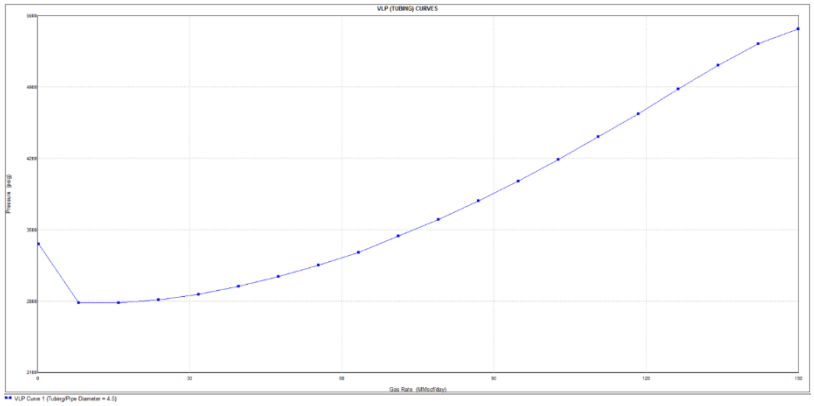

Figure 3.37. The vertical lift pressure system for current case.

3.6 RESERVOIR SIMULATION

Reservoir simulation is the powerful tool in reservoir engineering studies that is widely used by the industry. It is a beneficial tool that retains time and money for development plans in the future. After using the classic applications in reservoir engineering studies, it is the time to utilize the results from these techniques in order to mimic the North African field by using CMG simulator software (GEM). A radial reservoir model (cylindrical) was designed to simulate the flow behavior mechanisms and match the results from well-testing interpretation with the simulation results in order to forecast pressure history and production for next the thirty years.

3.6.1 Simulation Model Description. The radial reservoir model consists of 40×1×20 (r, theta, k) grid blocks, as shown in Figure 3.38, where r represents the number of radius sectors in the reservoir in which the inner radius is the wellbore radius 0.345 ft and the outer radius is the drainage radius 4,780 ft.

Also, theta represents the number of divisions in the reservoir model, where theta equaling one means 3600 angles. The top of the model is at a depth of 9,085 ft. The model includes 20 layers in k direction, and each layer has a thickness of 25 ft. In addition, the numerical aquifer (Carter-Tracy model) was built at a depth of 9,585.5 ft in the bottom side of the radial reservoir model.

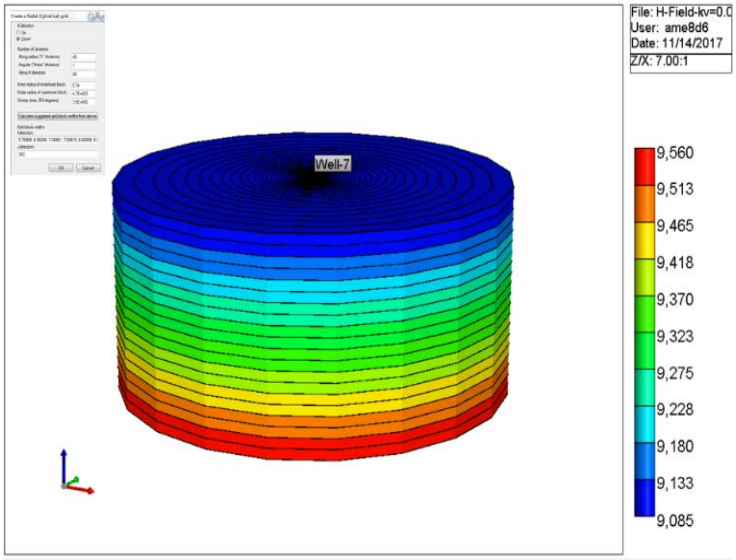

Figure 3.38. Radial reservoir simulation model description.

3.6.2 Reservoir Rock Properties. The results from open-hole logs interpretation and well-testing interpretation were utilized, as listed in Table 3.11 in order to fill the array

properties section in the simulator. These results include the grid thickness, reservoir top, porosity, permeability in three directions, and initial water saturation.

Table 3.11. The main input data for reservoir rock properties.

Parameter	Value	unit
Reservoir Top	9,085	ft
Grid Thickness	25	ft
Porosity	19	%
Formation Net Thickness	300	ft
Permeability (I-J-direction)	300	md
Vertical Perm/Horizontal Perm	0.012	Unitless
Initial Water Saturation	7.85	%

3.6.3 Reservoir Fluid Properties (PVT data). The reservoir fluid properties of the field data were defined using WINPROP compositional simulator as mentioned in the phase behavior section. The WINPROP file was converted to GEM format to enable the CMG simulator to import this file. After that, the reservoir fluid properties automatically were defined by the CMG builder throughout the radial reservoir model to mimic the reservoir fluid properties of the North African field.

3.6.4 Special Core Analysis Data (SCAL data). The special core analysis data consists of special tests such as relative permeability, capillary pressure, and wettability data. In this study, the relative permeability curves in Figure 3.39 and 3.40 were performed by laboratory measurements and provided by the Company. The relative permeability curves are very important to control the flow of gas, oil (condensate), and water. These curves have a main role and a significant effect in gas condensate reservoirs once the pressure drops below the dew-point pressure. The capillary pressure data were assumed to

be zero, which means that no transition zone between gas-oil contact (GOC) and gas-water contact (GWC). The ready data were imported in rock-fluid section in CMG builder, and following figures illustrate the two-phase relative permeability and water-oil (condensate), gas-oil (condensate), and three-phase relative permeability plot.

In addition, the three phase relative permeability plot was done by the simulator using the Stone #2 model. This plot demonstrates the flow behavior for three fluids together, as shown in Figure 3.41.

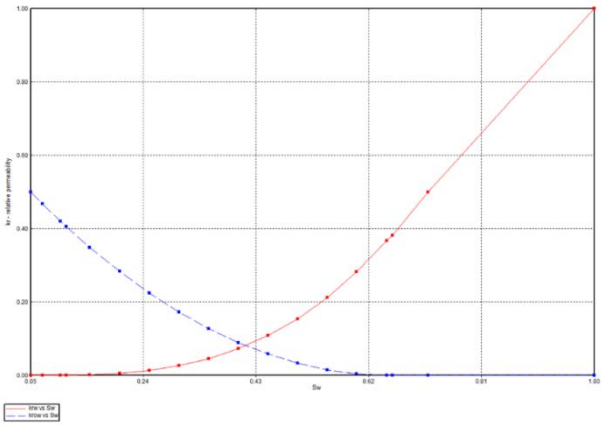

Figure 3.39. Two-phase water-oil (condensate) relative permeability.

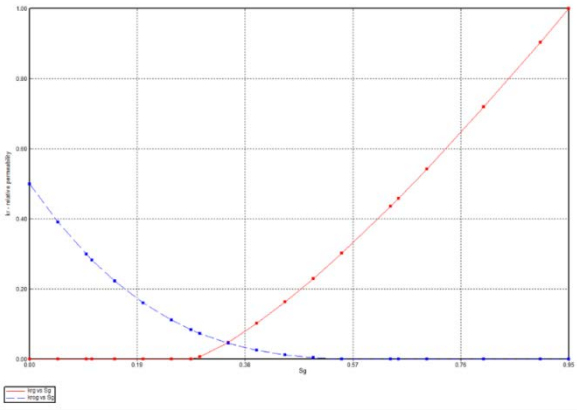

Figure 3.40. Two phase gas-oil (condensate) relative permeability.

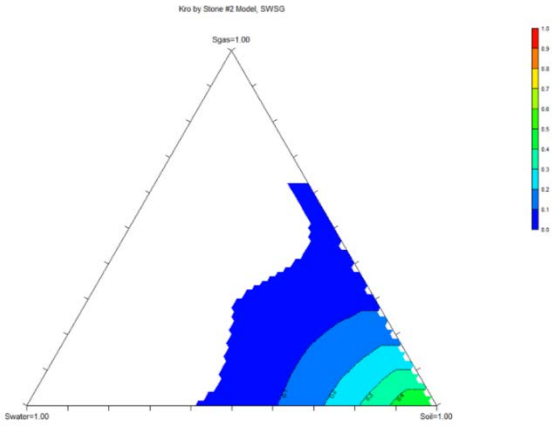

Figure 3.41. Three phase gas-oil (condensate)-water relative permeability.

3.6.5 Initial Conditions. This section is connected with the previous section, and the parameters listed in Table 3.12 are essential to define in order to complete building the model.

Table 3.12. Initial condition parameters.

Parameter	Value	unit
Reference pressure (initial reservoir pressure)	3,740	psi
Reference depth (mid-perforation depth)	9,300	ft
Water-Gas Contact (WOC)	9,585.5	ft
Water saturation below WOC	100	%

3.6.6 Wells and Recurrent Section. The well location was selected to be in the center of the reservoir with Coordinates (1 1 1:20). The well was classified as a production well and named Well-A-7. Also, the constraint values were added to the reservoir to regulate the operation system. In addition, the date ranges were added, which the study started in August 2005 to the target date in August 2050.

3.6.7 Numerical Section. This section is responsible for the solution iteration time steps in order to have a smooth run and accurate results without warning messages. Due to the complexity in gas condensate behavior, CMG support suggested that the numerical solution section needs to modify the default values by changing the maximum and minimum time step, linear solver iterations, linear solver orthogonalizations, and linear solver factorization, as listed in Table 3.13. After this modification, the model runs perfectly and shows results without any interruption during the run process.

Table 3.13. Numerical default and dataset values.

Parameter	Default Value	Dataset Value
Max. Time Step Size	365 days	5 days
Min. Time Step Size	1E-5 day	1E-6 day

3.6.8 Water Aquifer Properties. The bottom water aquifer was created based on assumptions because the aquifer properties are unknown data. The correct data were known after run the model and test the reservoir pressure history that affected directly by the water aquifer model. Table 3.14 lists the first assumption iteration for the aquifer properties

Table 3.14. Data for the water aquifer properties.

Parameter	Value	unit
Location	Bottom	-
Thickness	750	ft
Porosity	12	%
Permeability	70	md
Radius	1,690	ft
Angle	0.65	unitless
Modeling method	Carter-Tracy	-
Leak	Leakage is Allowed	-

3.6.9 Reservoir Pressure History. The reservoir pressure history match was affected by the water influx properties data and perforation completion (open or close) that controls the water influx to avoid earlier invasion into the reservoir. Firstly, the water aquifer properties were adjusted and run for multiple models. After that, the simulation results were exported to an Excel spreadsheet file to plot with the reservoir pressure history determined from the transient pressure analysis in 2009 and 2014, and other four points provided by the company. From the plot, the simulation results were compared to the actual pressure history. The perforation completion was changed by close or open the production layer that closed to the Gas-Water-Contact (GWC). The model was run again, and the results were exported to the same Excel sheet file. This step was repeated multiple times until the best water influx model has approached. The final scenario represents the North African water aquifer.

3.6.10 Gas, Condensate, and Water Production History. The production history of the reservoir was impacted by the layer thickness. The first assumption was 9 ft for each layer. However, the first scenario did not match the actual data. The decline in production history started early due to the low potential energy of the reservoir. After the adjusting process, the plateau period was longer as the layer thickness was increased until the match was reached when the layer thickness was 25 ft.

3.6.11 Future Performance. After the match for the average reservoir pressure had been reached, the projection of future IPR curve equations could be used to predict North African field performance. The two methods that were used are the theoretical and empirical methods. These techniques estimated the highest and lowest value of the absolute open potential flow. The theoretical method was used first by using Equations 3.74 and

3.75 to predict the (a) and (b) values that changed during the operation life. Moreover, the theoretical equation (Equation 3.70) was utilized to predict the new absolute open potential flow value at a certain average reservoir pressure. The same procedures were repeated for the empirical method, where inflow coefficient (C) is determined using Equation 3.76 and performance exponent (n) is a constant value throughout the reservoir life.

$$a_2 = a_1 \left[\frac{\mu_{g2} \times Z_2}{\mu_{g1} \times Z_1}\right] \tag{3.74}$$

$$b_2 = b_1 \left[\frac{\mu_{g2} \times Z_2}{\mu_{g1} \times Z_1}\right] \tag{3.75}$$

$$C_2 = C_1 \left[\frac{\mu_{g1} \times Z_1}{\mu_{g2} \times Z_2}\right] \tag{3.76}$$

3.7 SENSITIVITY ANALYSIS

Sensitivity analysis techniques were utilized as part of reservoir simulation studies in order to define the parameters that impact the reservoir pressure history, production history for both gas and condensate, water cut, and gas recovery factor. This research studied the following parameters.

3.7.1 Completion Perforation. This factor studied the effect of the production interval on the reservoir performance and the effect of water aquifer on the production by changing the location of perforation to produce far away from the gas-water-contact (GWC). The sensitivity was done by changing from open status perforation to closed status

perforation to control the thickness of the production interval. The formation thicknesses were chosen in the sensitivity analysis as follows: 250, 275, 325, and 350 ft.

3.7.2 Volume Lift Pressure Curve (VLP). Finally, after the IPR curves were forecasted for several years, the sensitivity analysis in Prosper software was utilized to predict the outflow tubing curve in order to estimate the flow rate system in the future. The wellhead pressures were chosen for the sensitivity analysis as follows: 400 psi, 800 psi, 1,200 psi, 1,600 psi, and 2,000 psi.

4. RESULTS AND DISCUSSION

4.1 FORMATION EVALUATION OF THE FIELD

The target of using open-hole log interpretation techniques was to determine the petrophysical properties for the North African field, where Figure 4.1 illustrates the main results. The figure consists of three types of results: volume of shale, porosity, and saturation through formation depths of 8,600 to 9,380 ft. As can be seen, the volume of shale (represented by green) has a low trend between depths of 9,150 to 9,300 ft. This represents the clean sand zone (limestone formation). At the same region, the porosity line (shown in yellow) has an almost a constant value around 20%. In addition, the saturation plot contains two scales of water and hydrocarbon saturation, where the water is represented by blue and the hydrocarbon (gas) is represented by red. This plot indicates that at the same interval, the hydrocarbon saturation is a high and water saturation is a low, which represents the initial water saturation around 7%.

These results were converted to the Schlumberger's Elan volume and Elan fluid in order to obtain a clear understanding and deep details about the formation. Furthermore, Figure 4.2 illustrates the Elan volume and Elan fluid for well A-7, where this figure assists the interpreter to evaluate and detect the pay zone thickness and petrophysical properties. The production interval is noticed clearly from both Elan plots, where the zone is between depths of 9,090 to 9,330 ft. The Elan volume shows the volume of shale, volume of clean sand (limestone formation), porosity, and water volume represented by gray, yellow, green, and blue, respectively. On the other hand, the Elan fluid demonstrates the saturation of

water, movable hydrocarbon, and unmovable hydrocarbon, represented by blue, red, and green, respectively.

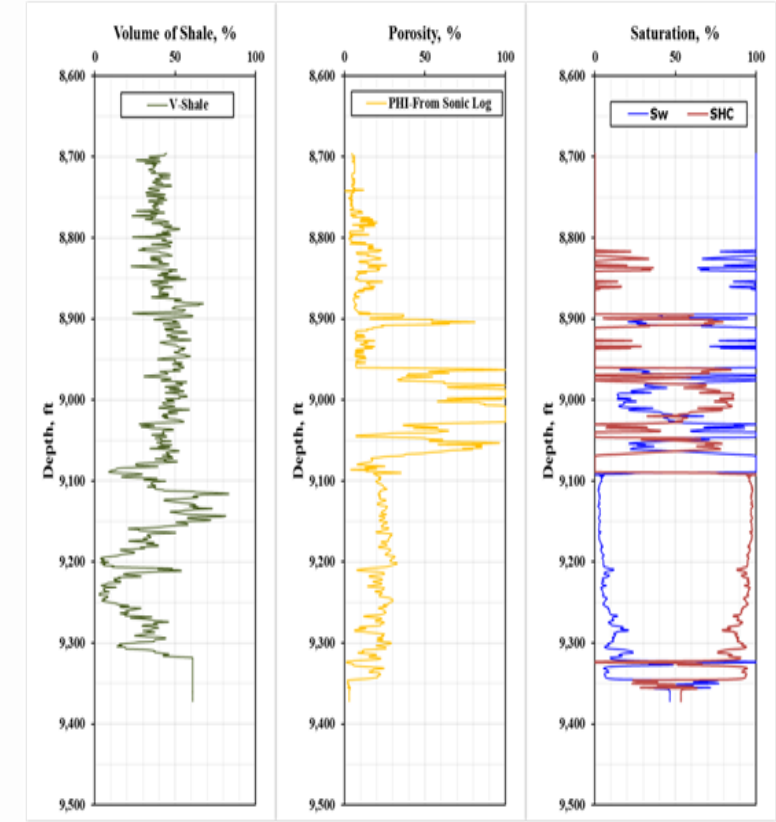

Figure 4.1. The main calculations for the open-hole log interpretation.

The formation evaluation process concluded that the formation content hydrocarbon has a good estimate, and the formation has very good bed thickness and petrophysical properties. Moreover, the interpreter can visually read the average reservoir porosity and average initial water saturation from the plot, or determine them from the cut-off procedures as mentioned in Section 3, Part 1. Table 4.1 lists the results of average reservoir porosity that is compatible to the result of the routine core analysis provided by

the company. The initial water saturation is approximately the same value as the special core analysis data (relative permeability data).

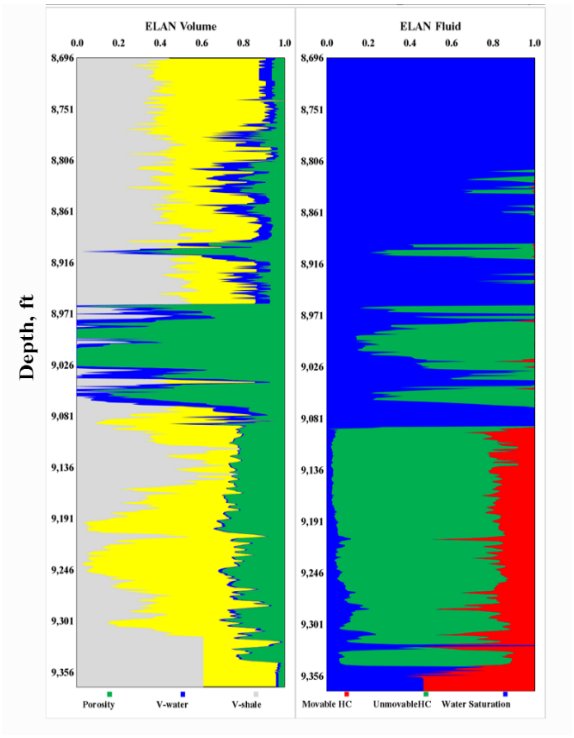

Figure 4.2. Elan volume and Elan fluid for the well A-7.

Table 4.1. The results obtained from formation evaluation process.

Parameter	Value	Unit
Formation net thickness	165	ft
Average reservoir porosity	0.19	fraction
Average initial water saturation	0.0782	fraction

4.2 FLUID CHARACTERISTICS OF THE FIELD

Representative fluid is a crucial input for reservoir simulation studies, especially for gas condensate case. In order to have a prober fluid model, a compositional simulation

model was established to match the gas condensate laboratory tests with the simulation results. Figure 4.3 illustrates the constant volume depletion plot, which represents the relationship between liquid volume (%) and pressure (psi). The dotted line shows the initial assumption step that was modulated by the simulator. As seen in the figure, the trend of the bold line indicates that the match was achieved by the final simulation run. This line was matched the experimental points perfectly and was thus taken as a representative of the fluid of the North African field. The simulator mimicked the reservoir fluid behavior in order to have accurate studies for the North African condensate fluid phenomena. The simulation results achieved dew-point pressure that was approximately the same value as the PVT data report, which is around 3,656.4 psi at the reservoir temperature 285˚F. Furthermore, the maximum liquid dropout was determined to be around 1% at reservoir pressure 1,700 psi.

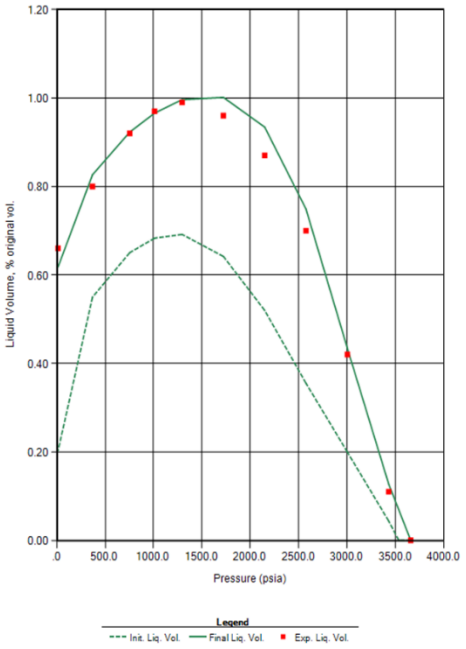

Figure 4.3. Constant volume depletion (CVD) model.

On the other hand, Figure 4.4 demonstrates the constant composition expansion plot, which represents the relationship between relative volume (fraction) and pressure (psi). The dotted line in this plot represents the initial assumption step that was automatically performed by the simulator. After regression process, the final match was reached at the dew-point pressure of 3,656.4 psi represented by the bold line. Therefore, the matching line is laying perfectly on the experimental points.

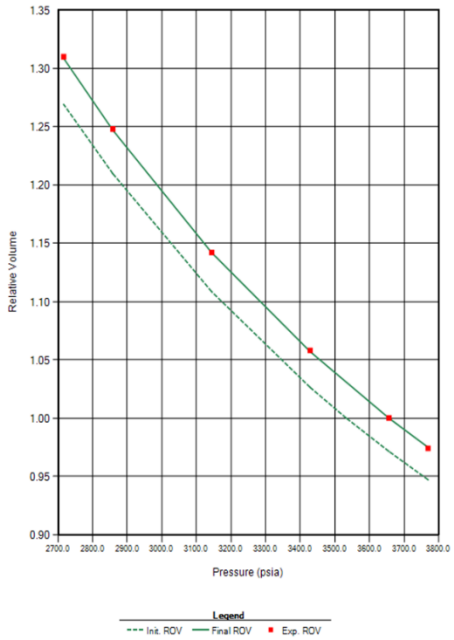

Figure 4.4. Constant composition expansion (CCE) model.

The phase envelope diagram was performed as illustrated in Figures 4.5 and 4.6, where the pressure-temperature plot represents the phase behavior of the North African field at the isothermal condition (reservoir temperature is constant throughout the reservoir). Figure 4.5 shows a wide range of the liquid volume between quality lines that is every 1%. As seen in the figure, when pressure drops below the dew point pressure at

the reservoir temperature 285˚F, the liquid starts evolving from the gas phase until reaching the maximum value of the liquid dropout at 1% liquid volume at the reservoir pressure 1,700 psi. These results are compatible with the constant volume depletion test results, constant composition expansion outcomes, and the laboratory measurements.

In order to investigate the amount of liquid dropout at a narrow range of pressures, the quality lines were performed to be every 0.1%, as shown in Figure 4.6. Moreover, it can be noticed that the quality lines are close to each other approximately every 150 psi pressure drop. As a result, the liquid dropout is increased by 0.01% liquid volume. These results are the crucial factor in order to investigate and understand the behavioral change in this case using the reservoir simulation technique.

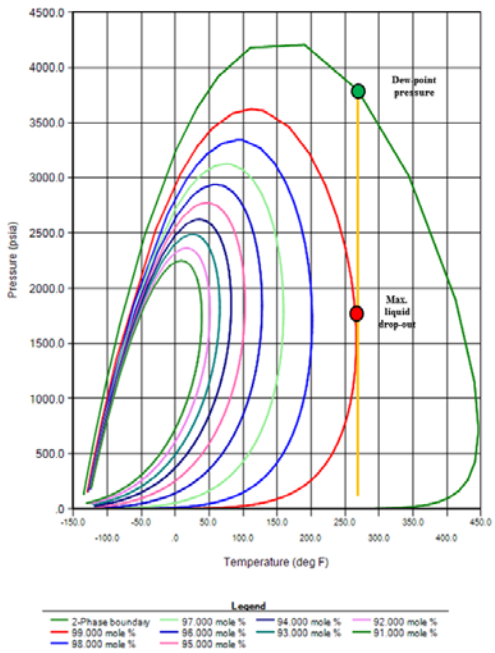

Figure 4.5. Phase envelope diagram for the gas condensate reservoir with 1% liquid volume ranges between the quality lines.

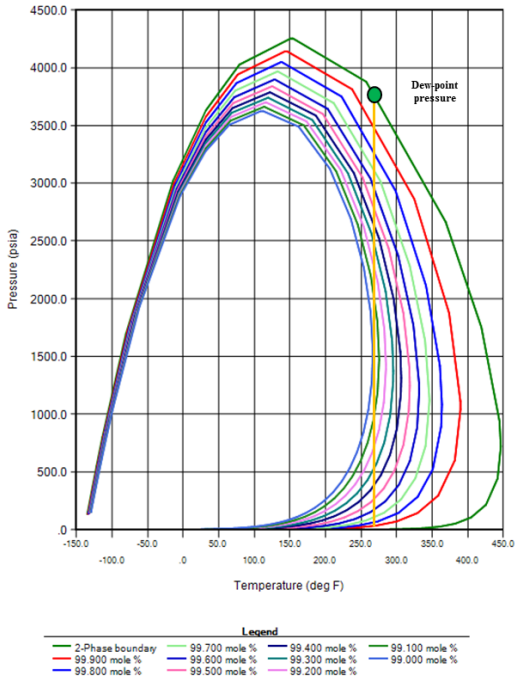

Figure 4.6. Phase envelope diagram for the gas condensate reservoir with 0.1% liquid volume ranges between the quality lines.

4.3 COMPATIBLE GAS PROPERTIES CORRELATIONS OF THE FIELD

4.3.1 Gas Deviation Factor. Several correlations and PVT software were used in order to determine the gas deviation factor. Figure 4.7 illustrates the results of these methods compared to the gas deviation factor obtained from the laboratory measurements. As can be seen in the figure, the results are very close to the laboratory measurements when pressure is below 2,500 psi. On the other hand, the correlation results are a little bit far from the laboratory results when the pressure is above 3,000 psi, except the results from PVT-P software that are approximately compatible with experiment points. In order to obtain the accurate results of the gas deviation factor, the averaging method was used to

determine the average gas deviation factor from these methods. Figure 4.8 shows the average gas deviation factor compared to the experiment gas deviation factor.

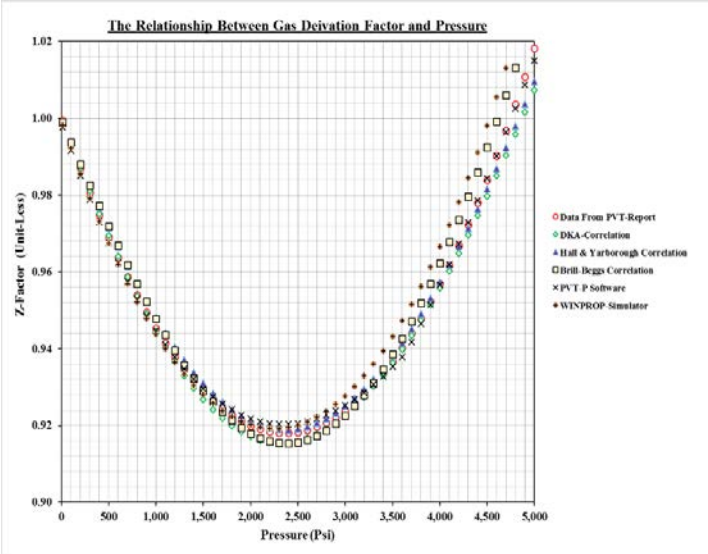

Figure 4.7. Results of gas deviation factor using different methods.

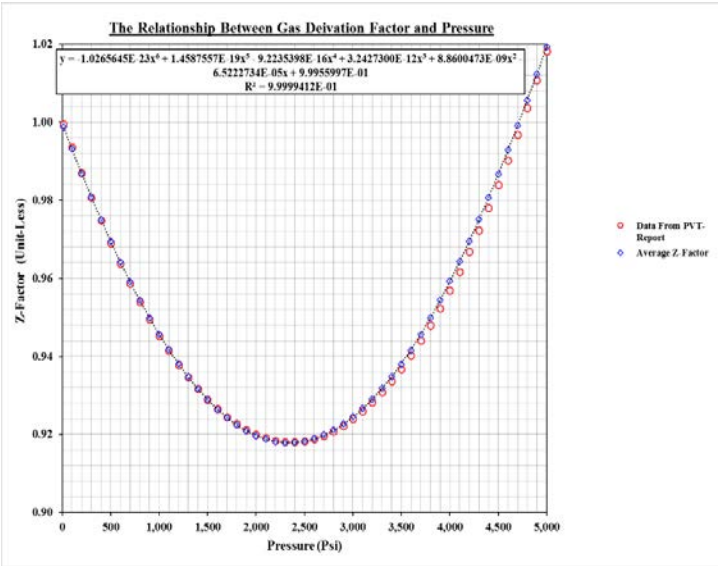

Figure 4.8. Comparison between gas deviation factor from the laboratory measurements and averaging value from different methods.

As shown in the figure, the formula obtained from the trend line was utilized to obtain the accurate gas deviation gas factor and then used for the pseudo-gas potential pressure calculations.

4.3.2 Gas Viscosity. Figure 4.9 illustrates the Lee, Gonzalez, and Eakin correlation results of the gas viscosity versus pressure. The figure indicates that the gas viscosity increased as the reservoir pressure increased. The trend line was plotted in order to obtain the gas viscosity formula and was utilized to determine the gas viscosity for wide range of pressures. These results were used with gas deviation factor results to estimate the real gas pseudo-pressure for the reservoir fluid.

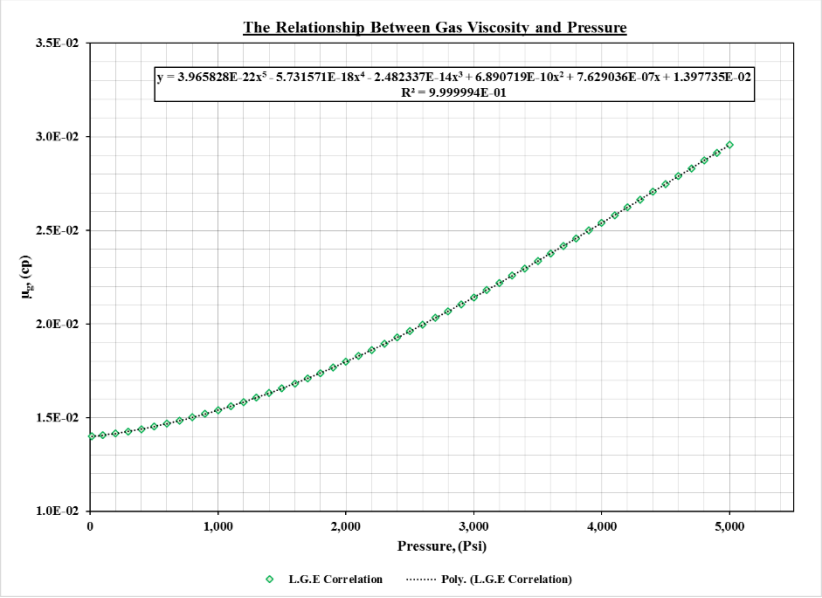

Figure 4.9. Relationship between gas viscosity using Lee, Gonzalez, and Eakin correlation and pressure.

4.3.3 Isothermal Compressibility. As the reservoir pressure increases the isothermal compressibility decreases until reaching a certain pressure that will be almost a

constant value. This relation is shown in Figure 4.10 where the isothermal compressibility is the main parameter to calculate the total compressibility factor used in the well-testing interpretation task.

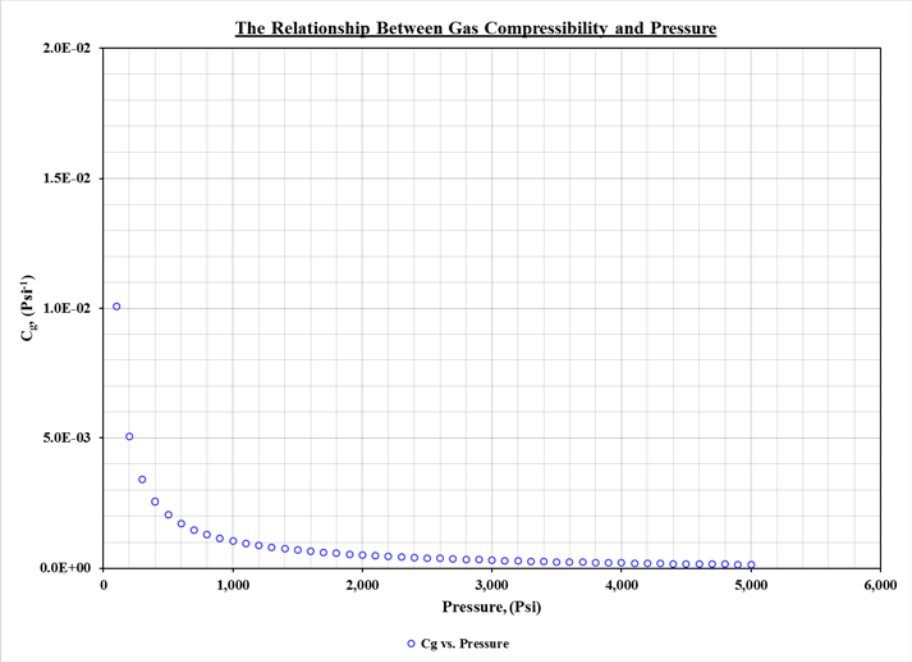

Figure 4.10. Relationship between isothermal compressibility and pressure.

4.3.4 Pseudo-Gas Potential Pressure. Figure 4.11 shows the relationship between gas-properties and pressure, and this plot defines the effect of changing pressure on the gas properties. When the reservoir pressure is below the 1,000 psi, the gas properties are almost at constant value, and the gas properties are constant when the reservoir pressure exceeds 4,000 psi. On the other hand, the middle region where the reservoir pressure relationship with the gas properties is changeable. The red circle points represent the changing pressure with gas deviation factor and viscosity, and the area under the curve represents the real pseudo-gas potential pressure.

After using the trapezoidal method, the pseudo-gas potential pressure curve was performed, as shown in Figure 4.12. The plot represents the relation between pseudo-gas potential with a wide range of pressures. The value of real pseudo-gas pressure increases as the reservoir pressure increases, and then, the trend line formula was used in order to convert the normal pressure to the pseudo-gas potential pressure. Moreover, Figure 4.13 illustrates the relationship between adjusted pressure and the normal pressure where the pseudo-gas potential pressure was converted to the adjusted pressure in order to have the pressure with convince unit. The trend line formula was utilized in order to determine adjusted pressure for a wide range of pressures and was then used in the well-testing analysis task.

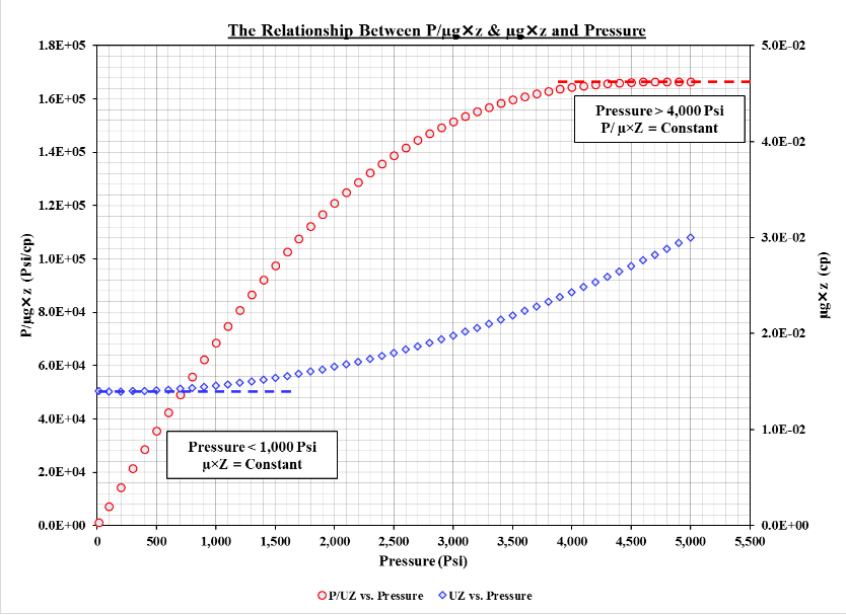

Figure 4.11. Relationship between gas properties and pressure.

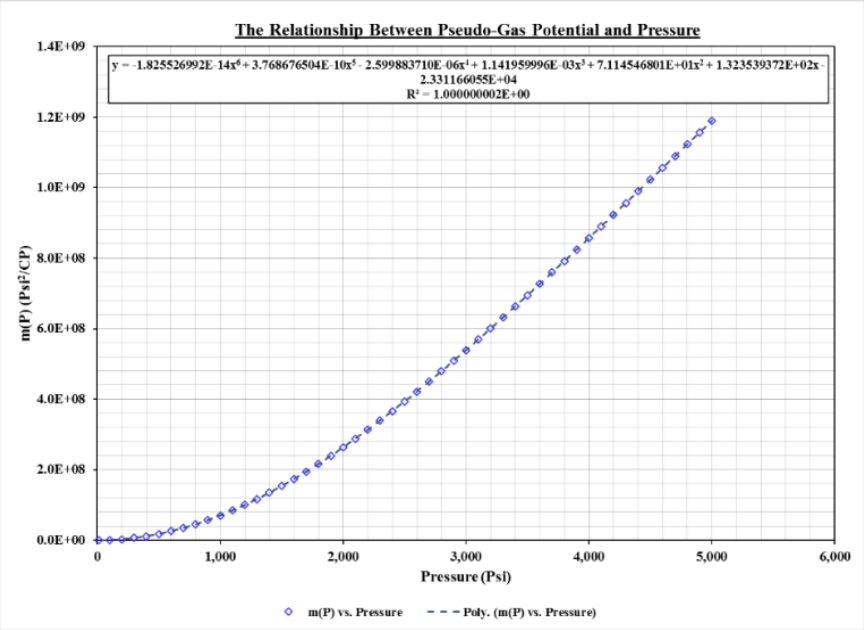

Figure 4.12. Relationship between pseudo-gas potential pressure and pressure.

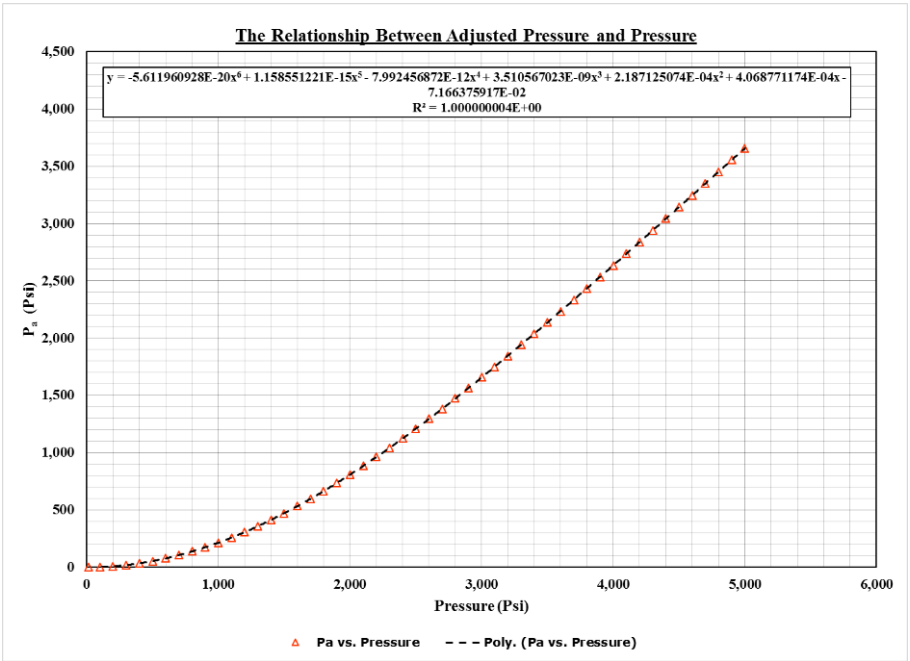

Figure 4.13. Relationship between adjusted pressure and pressure.

4.4 RESERVOIR CHARACTERISTICS OF THE FIELD

4.4.1 Analytical Method Results. The modern key result of the well-testing interpretation is the pressure derivative plot that represents the relationship between the Bourdet pressure derivative in red and pseudo-gas potential pressure drop in blue in y-axis versus the shut-in time in the x-axis, as illustrated in Figure 4.14. The early time as can be seen in the figure indicates that the wellbore storage region is varying. In this case, the wellbore storage is changing wellbore storage behavior due to a decrease in the fluid compressibility in the wellbore and tubing production. This happens in gas wells that have a high gas-oil ratio. When the well is shut-in, the liquid falls down in the borehole. This causes a change in density between gas and liquid and fluid and then a decrease in the pressure for a period of time. The middle time represents the porous media through the reservoir formation, and this case has three stabilization regions (radial flow regions). As can be seen in the figure, the pressure derivative behavior is decreased down as stairs, and this indicates that the reservoir fluid mobility ratio is changing throughout the reservoir. As the flow goes through the wellbore region, the reservoir permeability is decreased due to the decrease gas mobility ratio and increasing liquid amount in the porous media. As shown in the figure, the stabilization equation indicates that as the stabilization period is small, the permeability and net formation thickness values are high. On the other hand, the gas viscosity is low due to change the fluid behavior in the North African reservoir. Finally, the late time demonstrates the boundary effect that is not shown clearly in the derivative points. However, the late period in the pressure drop points have little stabilization, which indicates the reservoir is under the water aquifer (constant boundary).

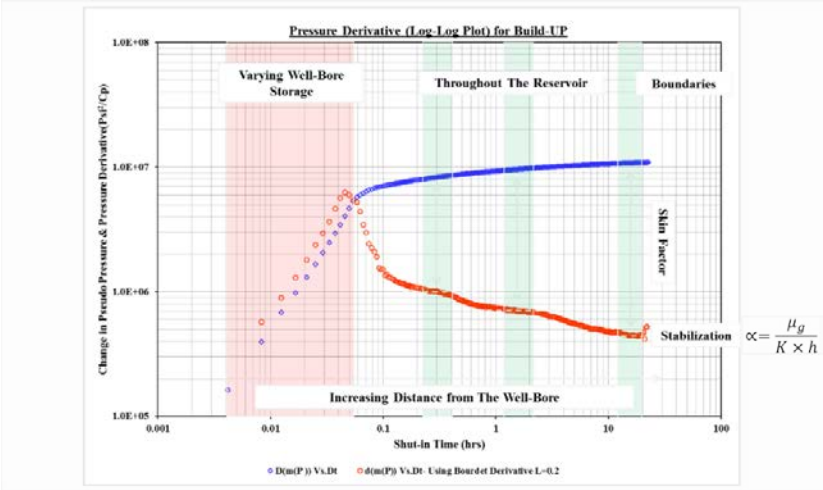

Figure 4.14. Pressure derivative plot for the buildup test.

The superposition plot approach was performed with the pressure derivative to detect the radial flow region in each stabilization period, as shown in Figure 4.15, 4.16, and 4.17. The red line represents the pressure derivative and the blue line is the pseudo-potential pressure drop. In each stabilization region, the slope was taken in order to obtain the formula, and then the reservoir characteristics values were determined.

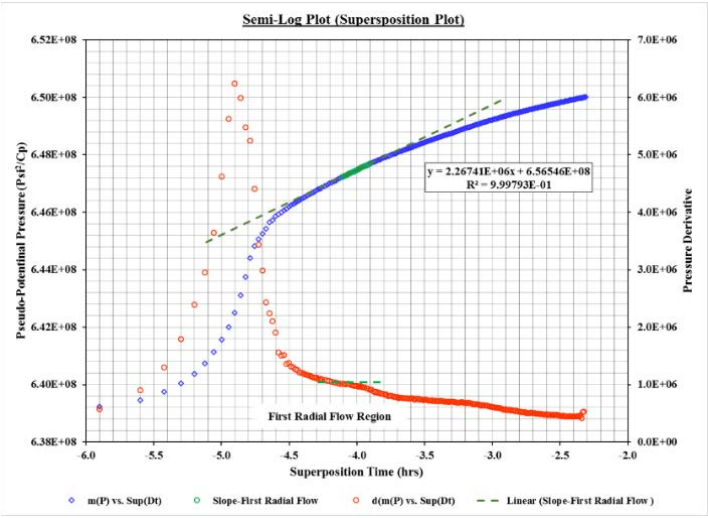

Figure 4.15. Superposition plot for the first radial flow regions.

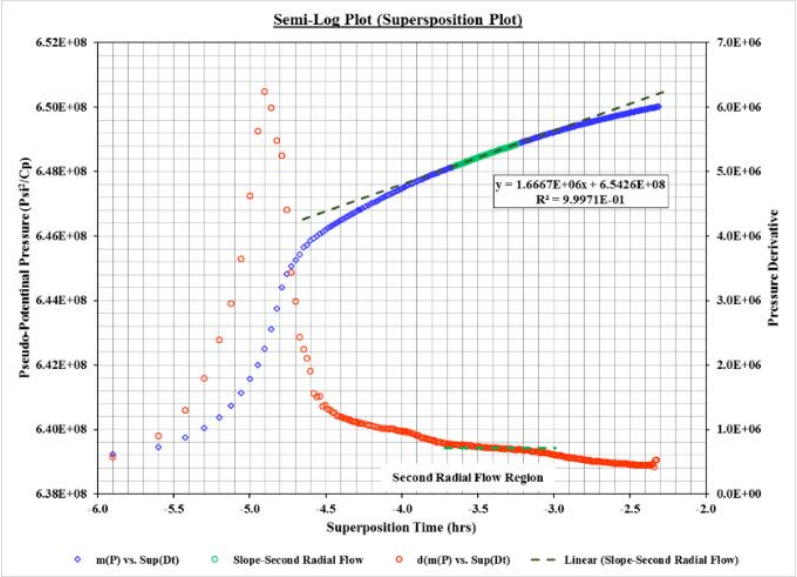

Figure 4.16. Superposition plot for the second radial flow regions.

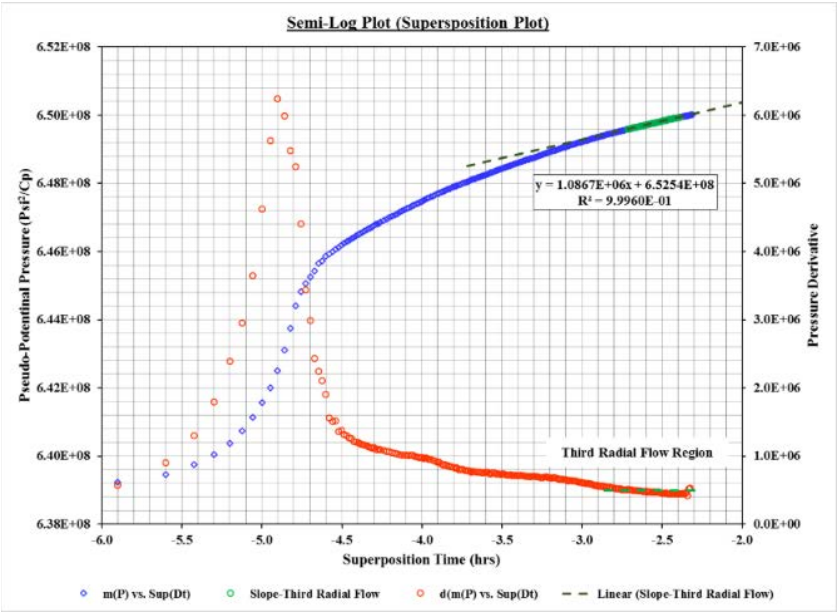

Figure 4.17. Superposition plot for the third radial flow regions.

Table 4.2 lists the results of the three regions. As seen in the table, the permeability value at the first region is lower than the second and third. Furthermore, the skin factor has a negative sign when the formation closes the wellbore region, and this indicates that an

acidizing job was done to the well after drilling operation. Finally, reservoir characteristic values indicate that the formation has good properties and decreasing in permeability is due to a change in the mobility ratio that causes the liquid dropout during the pressure drawdown.

Table 4.2. Well-testing interpretation results for three radial flow regions using superposition plot.

Parameter	First Region	Second Region	Third Region	Unit
Slope	2.2674E+06	1.6667E+06	1.0867E+06	$Psi^2/cp/Cycle$
Formation Flow Capacity	23,021	31,318	48,032	md.ft
Permeability	142.10	193.32	296.49	md
Intercept	6.5655E+08	6.5426E+08	6.5254E+08	Psi^2/cp
P_{1hr}	6.4855E+08	6.4838E+08	6.4871E+08	Psi^2/cp
Total Skin	-1.98	-0.51	3.05	-

4.4.2 Type Curve Results. Gringarten type curve analysis was utilized for more confident interpretation results. This method includes more results related to the wellbore storage outcomes. Table 4.3 lists the permeability and skin factor results for the three regions, which are very close to the superposition plot method outcomes. Because the wellbore storage results are not the same value for three regions, commercial software was used in order to obtain accurate results.

Table 4.3. Well-testing interpretation results for three radial flow regions using Gringarten type curve.

Parameter	First Region	Second Region	Third Region	Unit
Ca	5.495	5.495	5.495	Rbbl/Psi
CDe^{2s}	1.E+02	2.E+03	3.E+06	-
k	142.27	197	292	md
Kh	23,049	31,836	47,269	md.ft
CaD	6,292	5,215	6,046	-
Ca	4.864	4.031	4.674	Rbbl/Psi
S'	-2.07	-0.53	3.03	-

4.4.3 Modern Method Results. Saphir software was used for deep interpretation in order to obtain more results about the reservoir. Figure 4.18 illustrates the pressure derivative for the buildup test, where the small black line represents the software model, and the red and green points represent the pressure derivative and gas potential pressure drop for the field data. The software shows that the early time has changing wellbore storage due to change in the fluid compressibility. This region was matched using the Hegeman wellbore model, which is recommended by Kappa Engineering. Moreover, in order to match the middle region (reservoir model), multiple models were tried until the match was achieved using the radial composite model. The plot shows that the reservoir model is a radial composite model with three regions, and due to the software limitation, only the second and the third regions were matched perfectly, and the model did not match the first region, as shown in Figure 4.18.

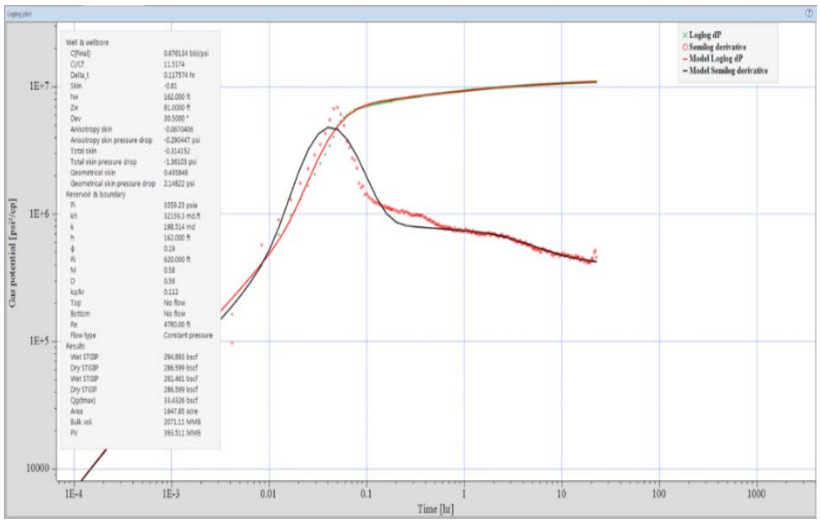

Figure 4.18. Pressure derivative plot for the buildup test using standard model.

The interpretation of the drawdown tests were done using Saphir software to obtain the skin factor and the condensate blockage radius at each drawdown. The following figures illustrate the pressure derivative of the four drawdown tests, which the model lines were matched completely by the pressure derivative behavior at each drawdown. Furthermore, the Hegeman wellbore model was used to match the early region that was affected by decreasing fluid compressibility.

Figure 4.19, 4.20, 4.21, and 4.22 demonstrate the results of the four drawdown tests the important parameter in this analysis was the skin factor to obtain the value of the non-Darcy flow coefficient and total skin at the zero flow rate.

Figure 4.23 shows the relationship between the equivalent gas flow rate and the condensate blockage radius. The results indicate that when the flow rate was increased, the radius of condensate banking was decreased to be closer to the wellbore.

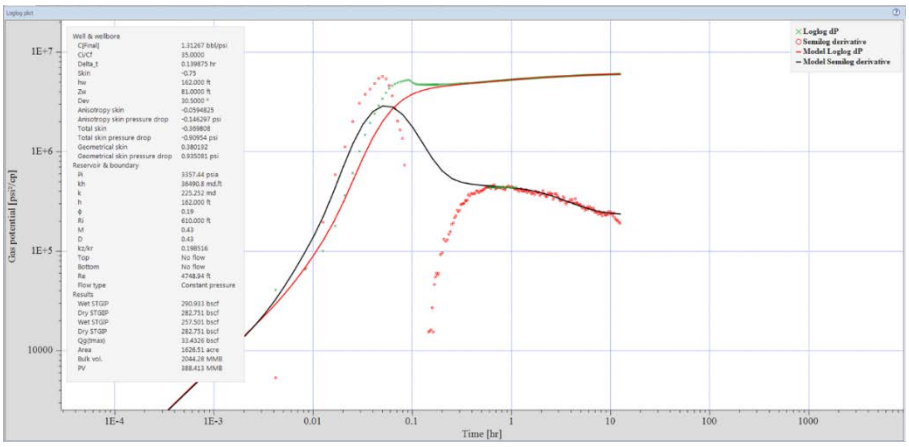

Figure 4.19. Pressure derivative plot of the first drawdown test.

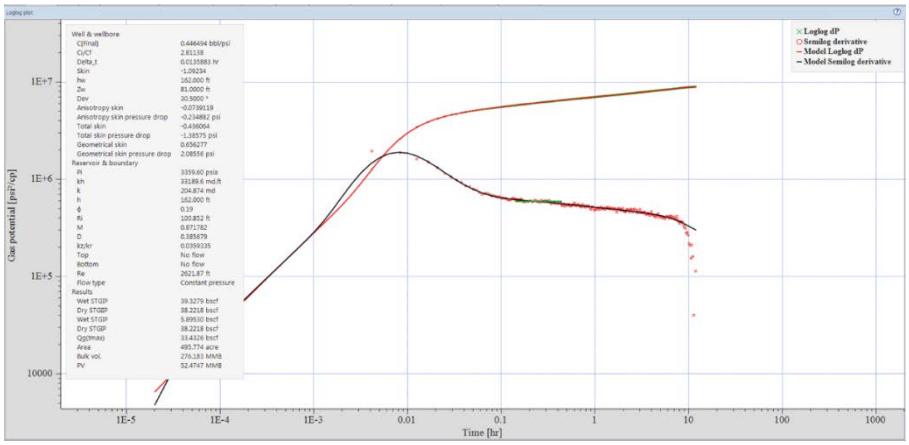

Figure 4.20. Pressure derivative plot of the second drawdown test.

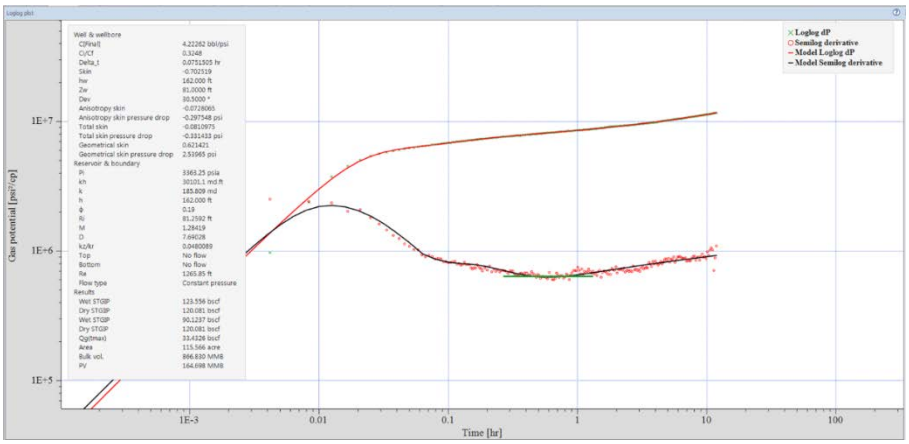

Figure 4.21. Pressure derivative plot of the third drawdown test.

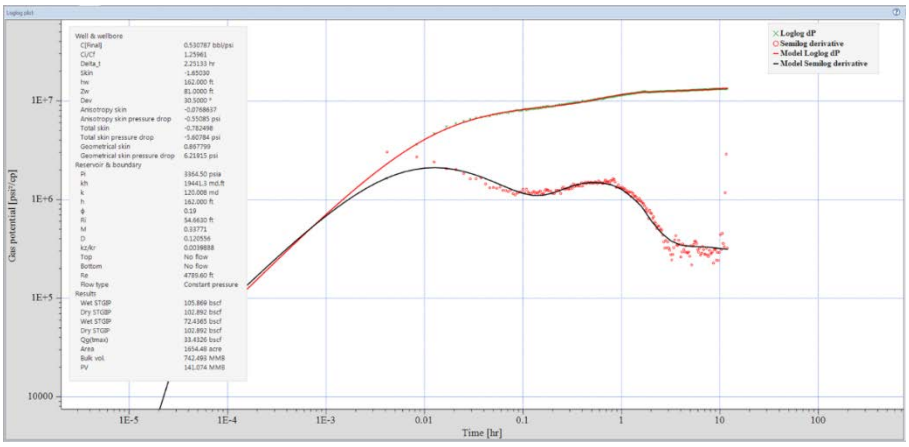

Figure 4.22. Pressure derivative plot of the fourth drawdown test.

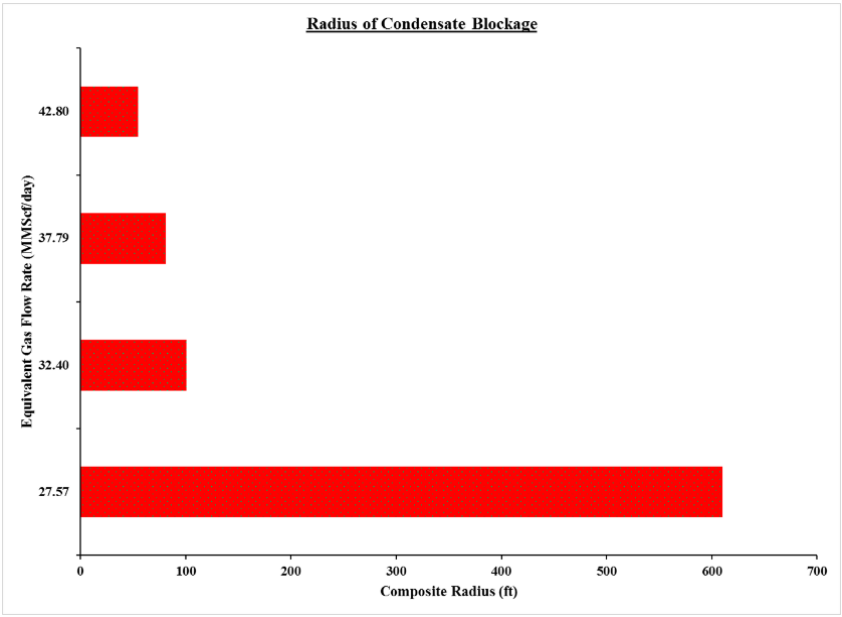

Figure 4.23. The relationship between equivalent gas flow rate and composite radius.

4.4.4 Dependent Skin Results. Figure 4.24 represents the rate-dependent skin method that was utilized to have a perfect match for the reservoir pressure history throughout the test. As can be seen in the plot, the intercept represents the skin factor at the zero flow rate and the slope represents the non-Darcy flow coefficient.

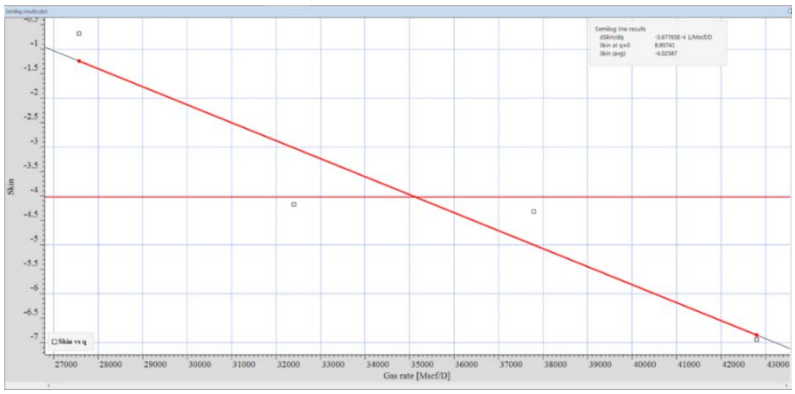

Figure 4.24. The initial results of the rate-dependent skin method.

These results that obtained from Figure 4.25 are the main effective parameters to achieve the pressure history match. Figure 4.26 shows the results after the regression process, the model matched the reservoir pressure history perfectly. The accurate skin factor at the zero flow rate, the non-Darcy flow rate, and the average reservoir pressure were obtained to be used in the deliverability calculations.

Figure 4.26 illustrates the results of the rate-dependent skin method after obtaining the skin factor from each drawdown using the time-dependent skin method. The time-dependent skin method was used to compare the results with the rate-dependent skin method to confirm the results of skin factor at the zero flow rate, the non-Darcy flow coefficient, and average reservoir pressure. As a result, the outcomes were very close in both methods, but the model line of the second method in the pressure history plot had the better match, as shown in Figure 4.27. This plot shows the results that were used in the deliverability analysis and reservoir simulation studies.

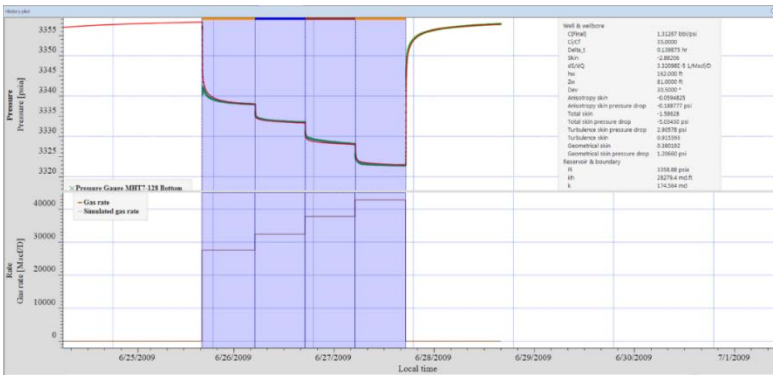

Figure 4.25. The pressure history match though the test using the rate-dependent skin method.

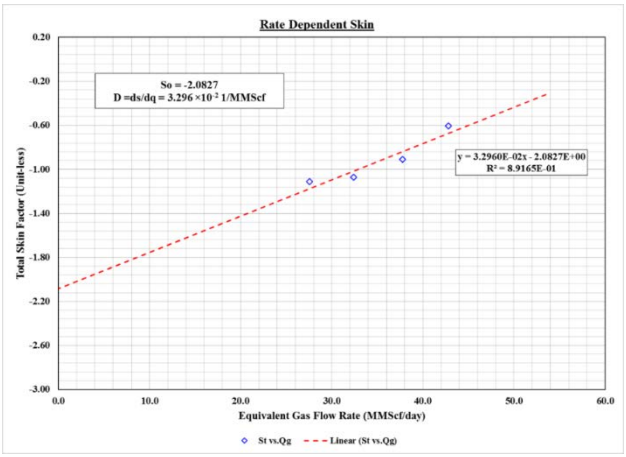

Figure 4.26. The results of the rate-dependent skin method.

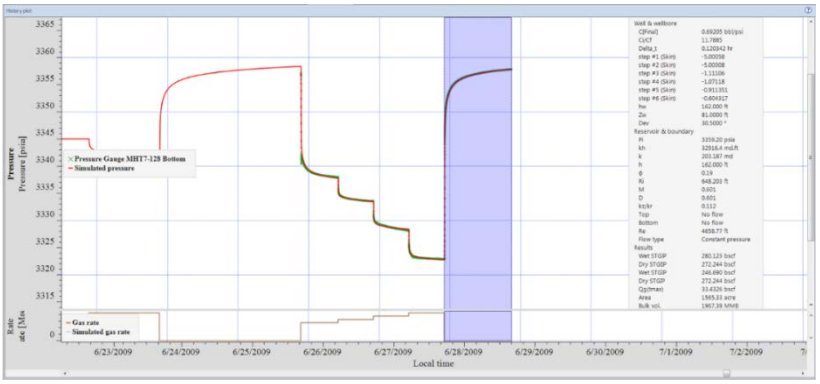

Figure 4.27. The pressure history match though the test using the time-dependent skin method.

4.4.5 Comparison Between Two Tests. The pressure derivative overlay was used to compare the pressure derivative for both the well tests in 2009 and 2014, as illustrated in Figure 4.28. As seen in the plot, both pressure derivatives have the same shape, where the three radial flow regions can be noticed. The changing in the wellbore storage exists in both pressure derivatives. Thus, all the results in both tests are approximately compatible, and slight change in the outcome values were due to changing in mobility ratio as a result, pressure depletion and increasing in the liquid dropout.

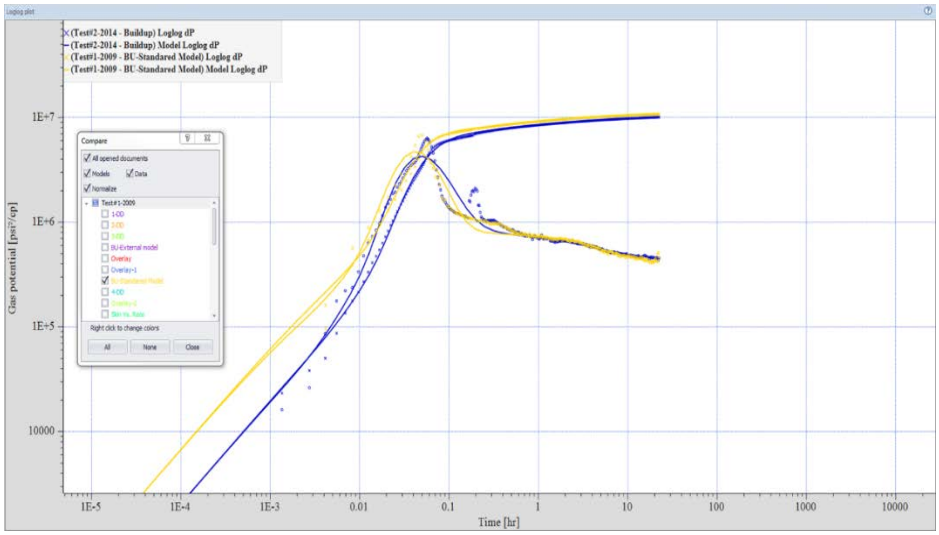

Figure 4.28. The pressure derivative overlay for the buildup tests in 2009 and 2014.

4.5 THE FIELD FLOW POTENTINAL

The results that illustrated in this section were obtained from the analysis of the flow-after-flow test in 2009.

4.5.1 Analytical Results. An empirical method was used using three techniques (Excel, Saphir, and Prosper) to obtain the empirical parameters, the inflow, and outflow

reservoir performance. Figure 4.29 illustrates the empirical method analysis using Excel calculations. The analysis shows that the performance exponent value is around 0.80 (unitless) which indicates the reservoir is under the condition flow closest to the laminar flow. The non-Darcy flow coefficient from the well-testing interpretation in 2009 was a very low value that proved there is no turbulent flow during the production process. This allows the reservoir potential to be very high, as found using the empirical method where the absolute open flow (AOF) potential in 2009 was around 985.34 MMscf/day.

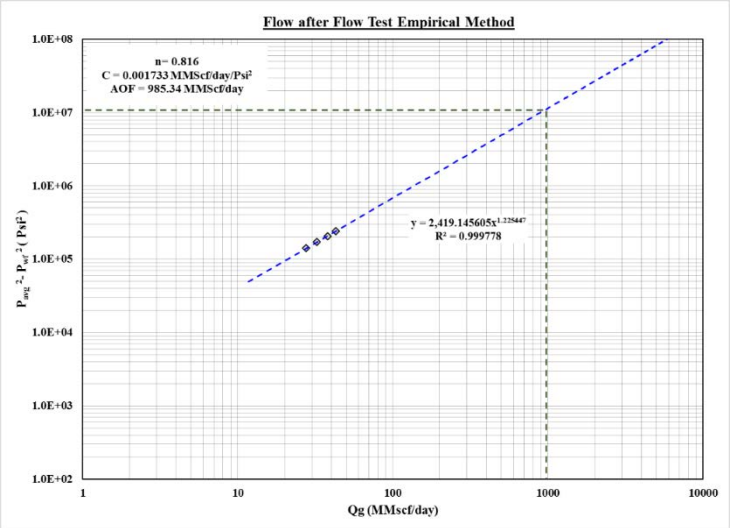

Figure 4.29. Deliverability analysis using the empirical method with the Excel.

Furthermore, the empirical method was utilized using Prosper software, and this method in the software is known as a multi-rate (C) and (n) method. Figure 4.30 illustrates the IPR curve and the main results are listed in the box inside the plot. These parameters are the same as previous approaches.

The software was selected to build the vertical lift performance with the IPR of the well in the North African field. Figure 4.31 shows the match of the outflow performance with inflow performance curve. The intersecting point between the two lines represents the gas flow rate system. This is the flow rate that the well can produce when the well-head pressure is 2,196 psi.

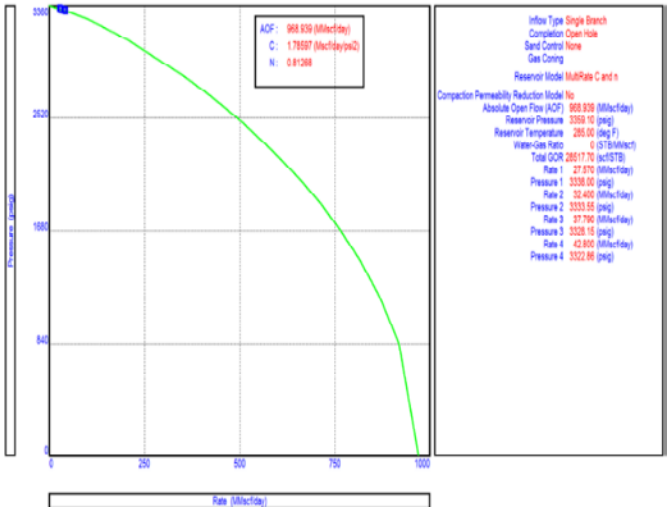

Figure 4.30. The empirical inflow performance relationship using Prosper.

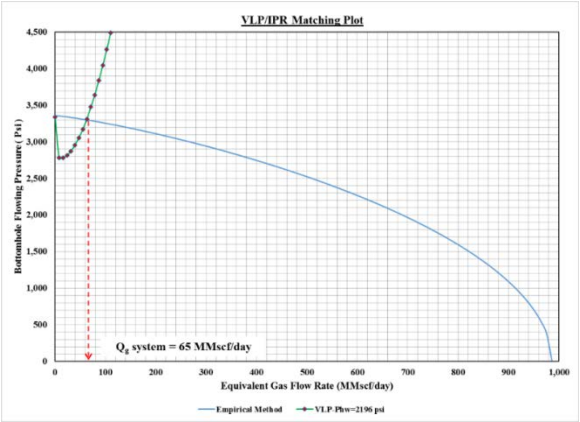

Figure 4.31. Match of vertical lift performance with the empirical inflow performance relationship using Prosper software.

Theoretical method is based on the pressure square approach that was utilized to obtain the theoretical parameters and the inflow and outflow performance of the reservoir using three applications: Excel and Prosper. Figure 4.32 shows the analysis to determine the theoretical parameters obtained from the trend line formula. These parameters were used to determine the AOF potential. This approach indicates that the reservoir potential is high as proved in the previous method, and the value of AOF is around 510 MMscf/day. This technique shows that the value of AOF is lower than the AOF from the empirical method due to the assumption in each method.

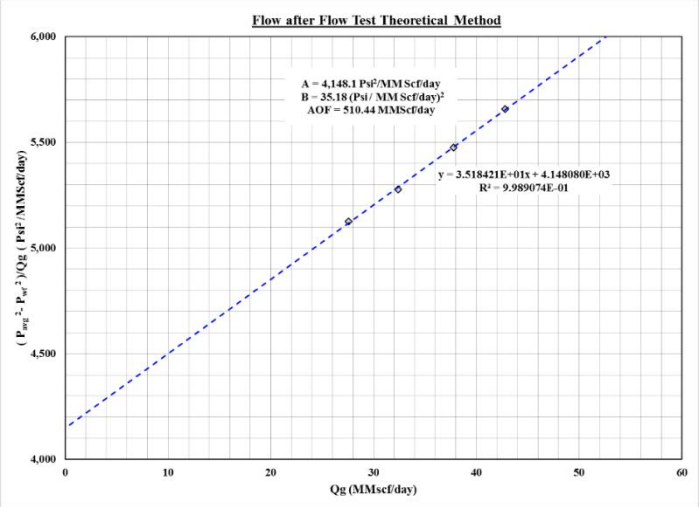

Figure 4.32. Deliverability analysis using the theoretical method with Excel.

This approach is known in Prosper by name the multi-rate Jones. As shown in Figure 4.33, the deliverability results for this method are the same as the previous technique (Excel). The plot shows the results where these parameters were used to perform the IPR curve.

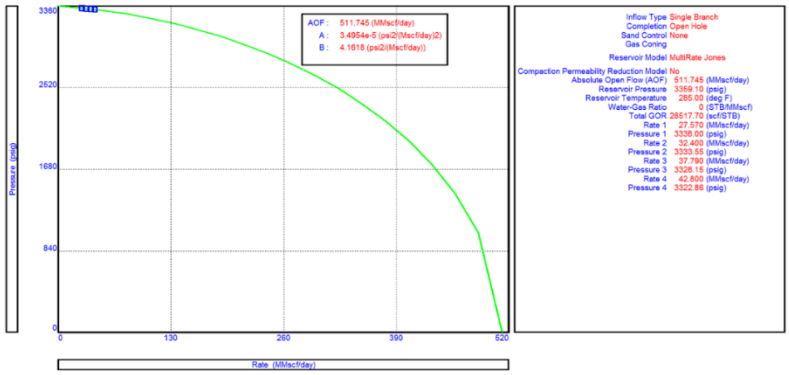

Figure 4.33. The theoretical inflow performance relationship using Prosper.

The same well-head pressure value was used in the Prosper software to obtain the gas flow rate system for the well using the theoretical method. The vertical lift performance was performed on the inflow performance plot, as shown in Figure 4.34, where the value of the gas flow rate system was around 65 MMscf/day. The result from this plot is the same as in the empirical method.

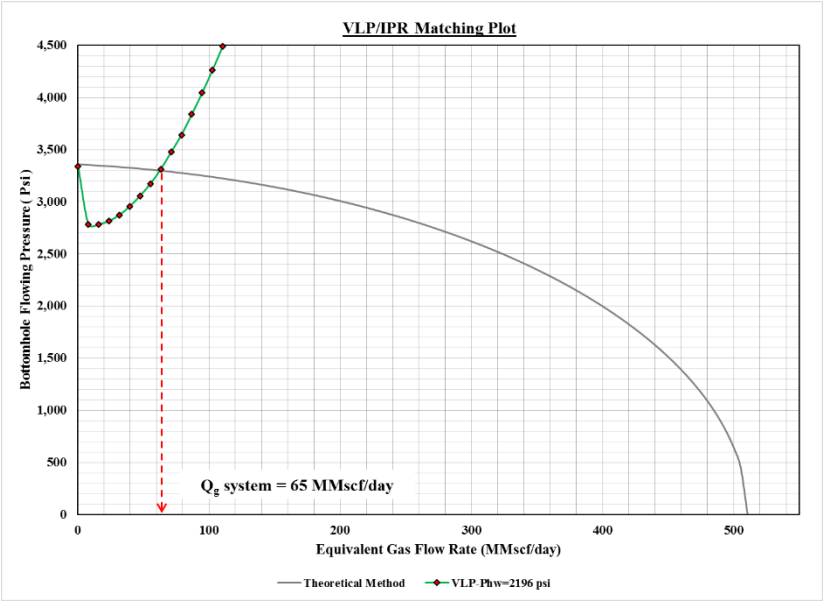

Figure 4.34. Match of vertical lift performance with the theoretical inflow performance relationship using Prosper software.

The assumption of the exact method is based on the real gas pseudo-pressure that was used to count the effect of the gas properties change with respect to pressure. This method was calculated using Excel calculations, Saphir, and Prosper. Figure 4.35 shows the results of this technique using the Excel, and the absolute open flow (AOF) potential was around 566 MMscf/day. This value is very close to the theoretical AOF, but the value of the exact AOF is lower than the empirical AOF.

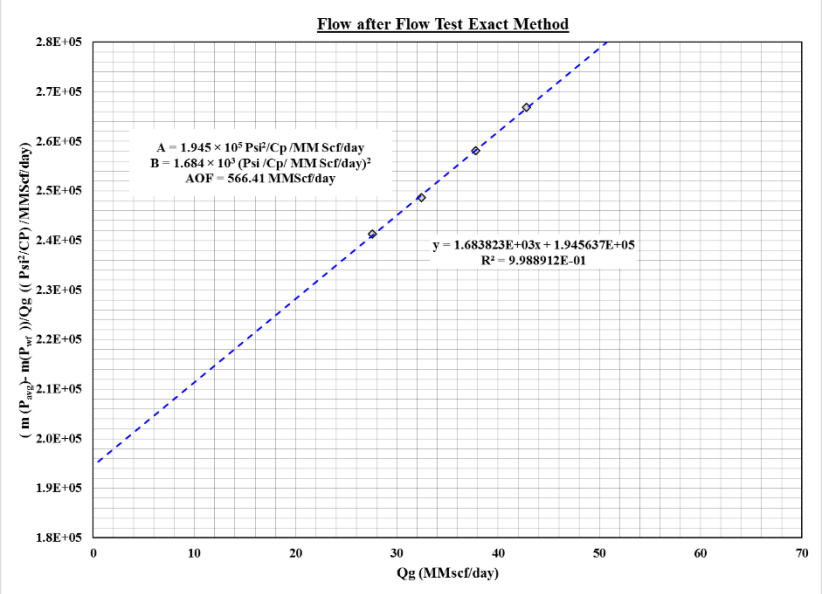

Figure 4.35. Deliverability analysis using the exact method with Excel.

Prosper shows the same results as the previous tools (Excel), where the exact parameter results are listed in Figure 4.36. The IPR curve is illustrated in the figure using the exact method, which is called the multi-rate Forchheimer with pseudo-pressure.

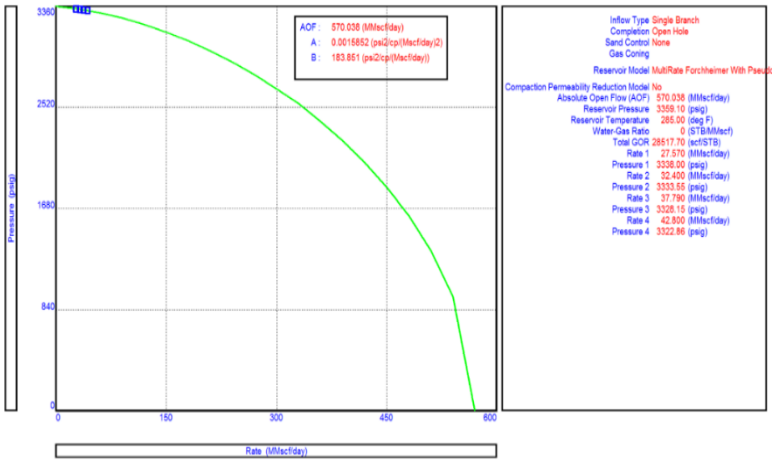

Figure 4.36. The exact inflow performance relationship using Prosper.

Figure 4.37 illustrates the vertical lift performance for the well where the intersecting point between the two models was around 65 MMscf/day. This value represents the gas flow rate system of the well in the North African field.

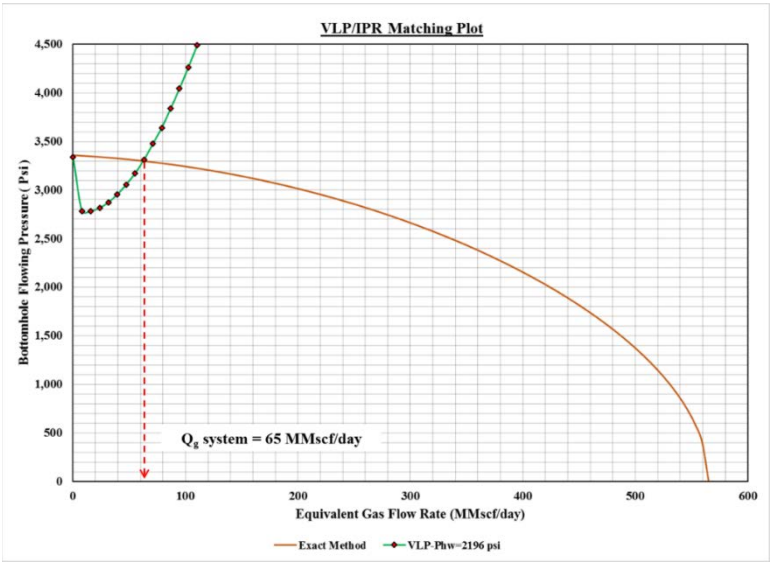

Figure 4.37. Match of vertical lift performance with the exact inflow performance relationship using Prosper.

As can be seen in Figure 4.38, the gas flow rate system is a constant value in three methods, but the absolute open flow (AOF) potential in each method has a difference value due to the different in equation assumptions.

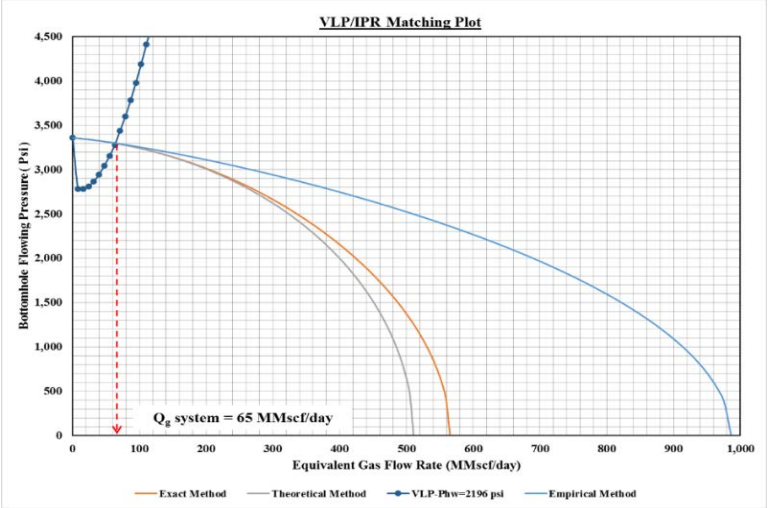

Figure 4.38. Match of vertical lift performance with the three inflow performance relationship methods using Prosper software.

4.5.2 Explanation of Results. The key factor to understand the difference in the absolute open flow potential results in the three methods is shown in Figure 4.39. When the pressure is below the 1,000 psi, the empirical method is valid due to the gas properties remaining constant with the changing pressure. The exact method works when the pressure ranges between 1,500 to 4,000 psi, as shown in the plot. This area shows that the gas properties have a large change with changing pressure. The late region represents the theoretical method area that is valid when the pressure is above 4,000 psi. According to Johnston et al., in 1991 SPE 23440, using the empirical method (Rawlins and Schellhardt) could cause an incorrect value of absolute open flow potential due to over large variations

in pressure when extrapolate the empirical equation. In addition, the empirical equation is valid only in low pressure ranges (Lee, 1982).

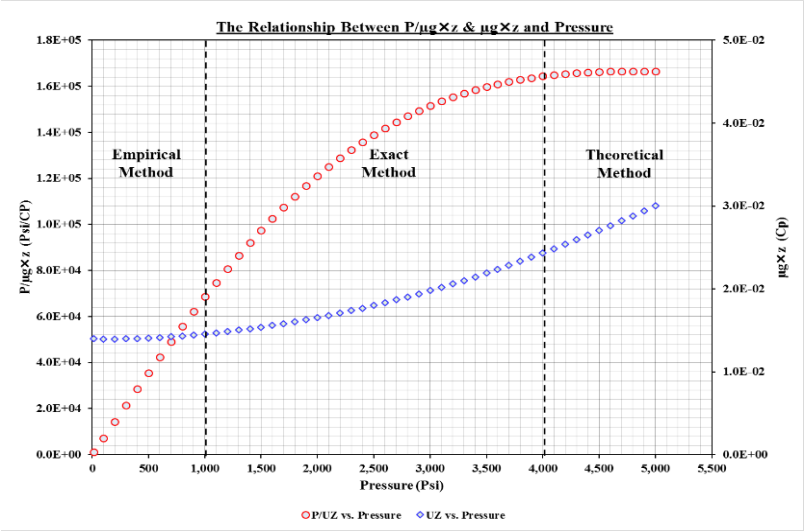

Figure 4.39. Relationship between gas properties with pressure.

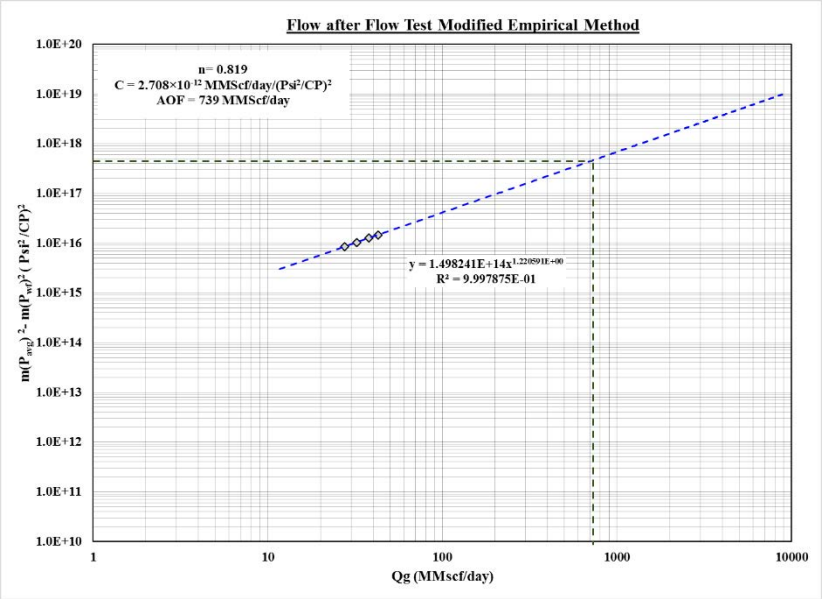

Figure 4.40. Modified empirical equation results.

In order to decrease the error in the empirical equation, the equation was modified by replacing the normal pressure with the pseudo-gas pressure in Equation 3.68. Figure 4.40 shows the results in the new empirical equation, where the absolute open flow (AOF) potential is very close to the AOFs in the theoretical and exact method. The exponent performance is almost the same as exponent performance in the normal empirical equation. According to Lee, Well Testing SPE book in 1982, this equation is applicable for wide range of pressures when the gas pseudo-pressure is used.

Figure 4.41 illustrates the inflow performance relationship with the vertical lift performance curve using the modified empirical equation.

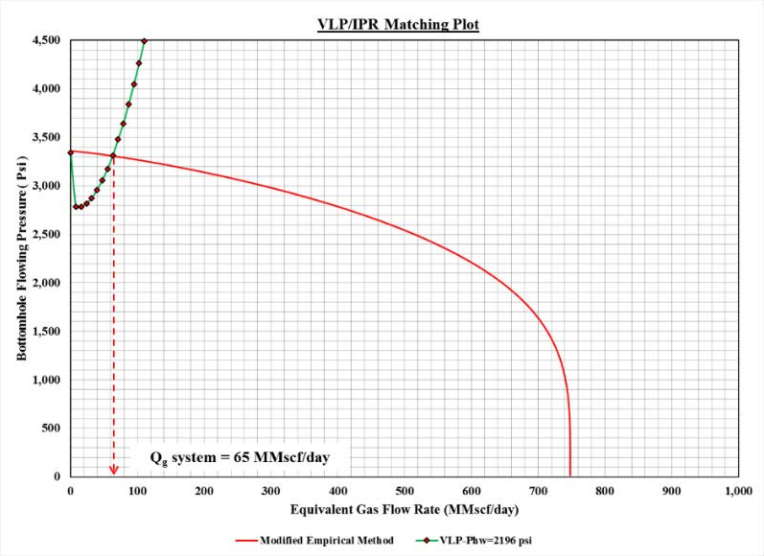

Figure 4.41. Match of vertical lift performance with the modified empirical inflow performance relationship using Prosper.

Figure 4.42 illustrates the inflow performance relationship with the vertical lift performance curve using all methods, where the difference in AOF values is shown clearly.

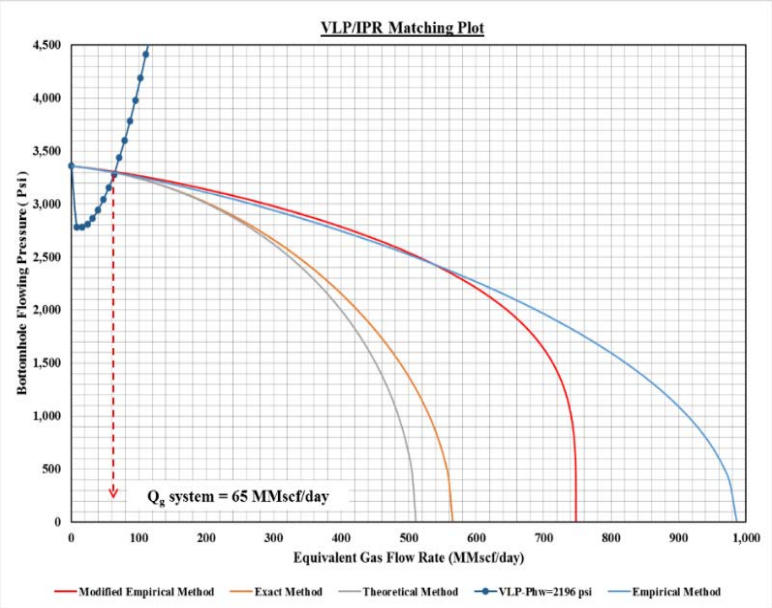

Figure 4.42. Match of vertical lift performance with all methods of the inflow performance relationship using Prosper.

4.5.3 Comparison between Two Tests. Figure 4.43 illustrates the empirical method calculations in 2009 and 2014 where test data shows the empirical method parameters for the different years. This relationship proves that the performance exponent (n) is constant through two tests, where the value is around 0.81 (unitless). Subsequently, the performance exponent is a constant value in future analysis. On the other hand, the inflow coefficient (C) was slightly increased from 2009 to 2014. As a result, the (AOF) potential was decreased by 3.38% during that time.

Furthermore, the IPR curve was performed in 2009 and 2014, as shown in Figure 4.44. This plot shows the effect of the new AOF and of C on the IPR curve, where the curve in 2014 shift down due to the reduction in AOF.

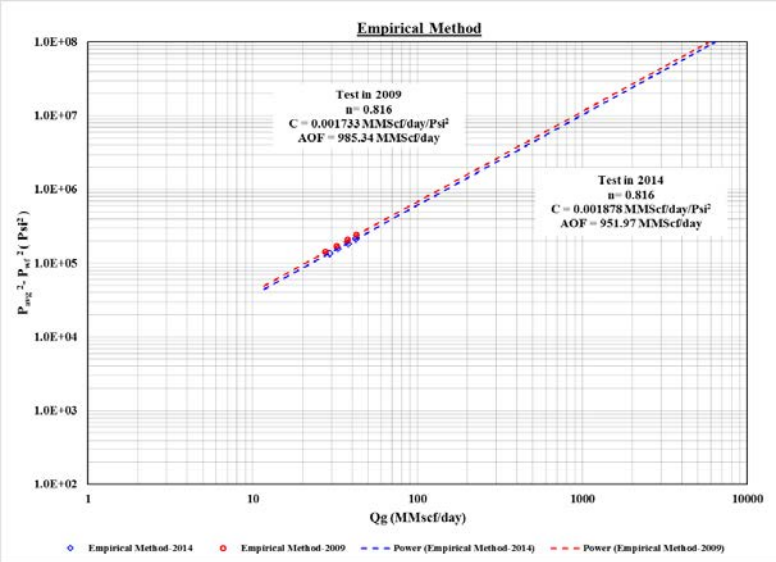

Figure 4.43.Empirical method calculations in 2009 and 2014.

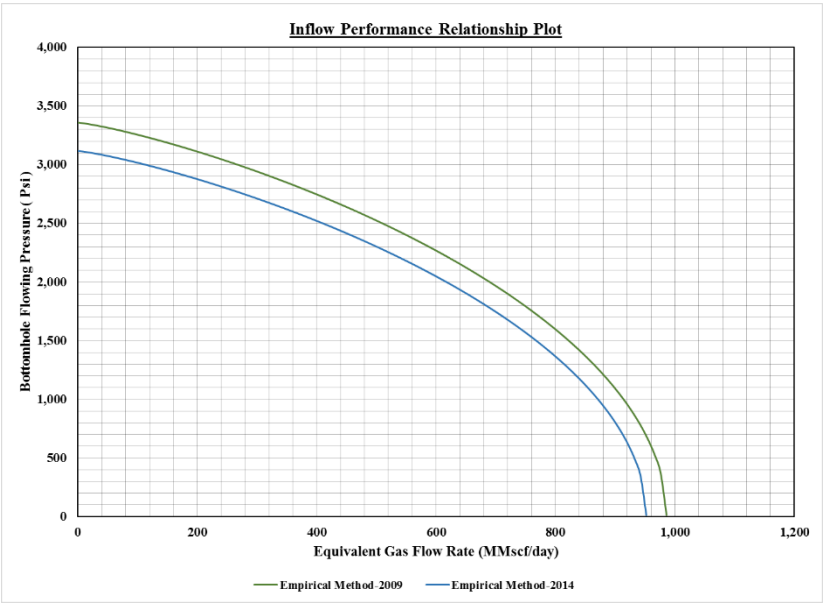

Figure 4.44. Empirical inflow performance relationship in 2009 and 2014.

Figure 4.45 and 4.46 show the IPR curve in both methods (theoretical and exact). The well performance was reduced as the years increased. The down shift in the IPR curve in 2014 was due to the change in the main parameters that built the two techniques. The

decrease in the AOF value in the theoretical method was around 1.71% and approximately 2.84% in the exact method.

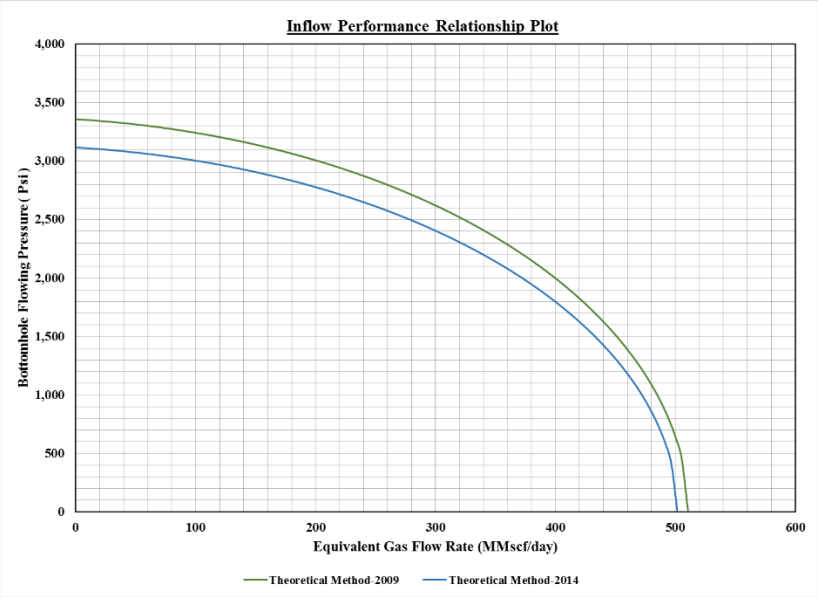

Figure 4.45. Theoretical inflow performance relationship in 2009 and 2014.

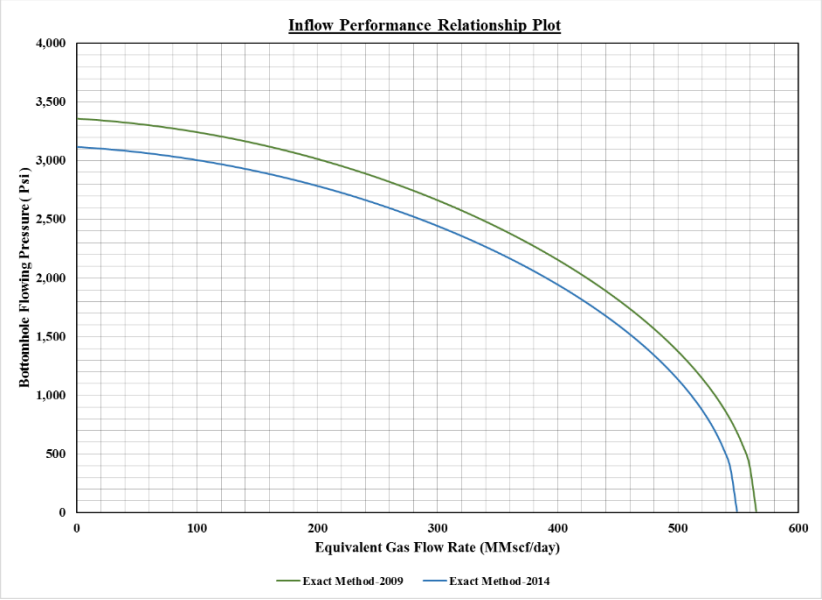

Figure 4.46. Exact inflow performance relationship in 2009 and 2014.

4.6 SIMULATION OUTCOMES OF THE FIELD

This section represents the base case for the North African simulation model. The case was built based on the previous tool results in order to mimic the field. Figure 4.47 illustrates the average reservoir pressure history simulation results over the years.

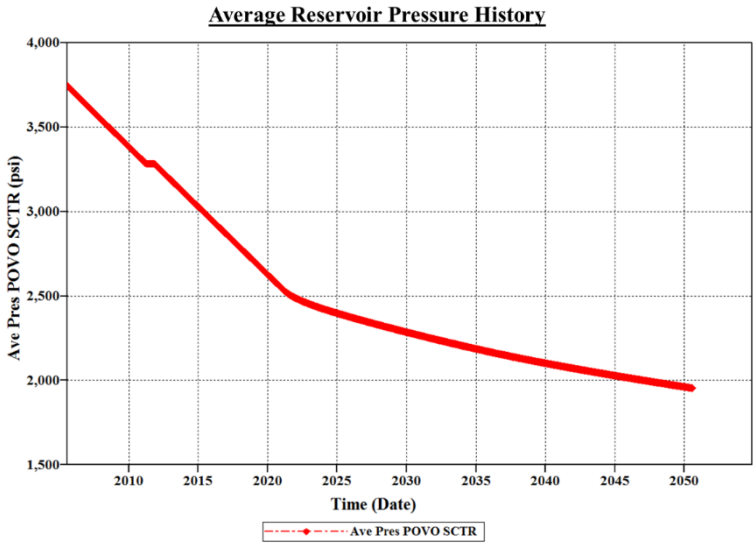

Figure 4.47. Reservoir average pressure history result using reservoir simulation.

As shown in Figure 4.48, the pressure curve is curved and shifted up when the water starts invading the reservoir approximately in the year 2022. This indicates that the water cut support the average reservoir history and prevents the early depletion in the reservoir pressure. In other words, the relationship is proportional when the water cut is increased and the reservoir pressure is more supported. The water cut in this case is very low, which is slowly increased over the years, and the ultimate water cut value in 2050 is less than 0.05.

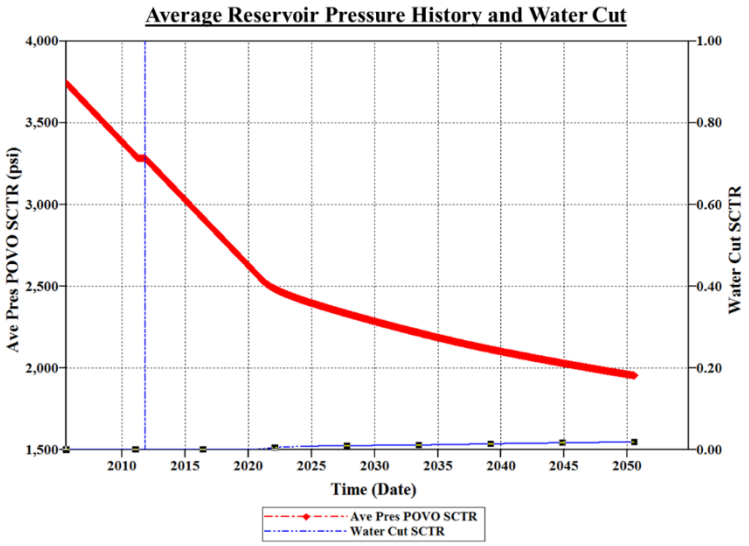

Figure 4.48. Relationship between reservoir average pressure and water cut simulation history.

Figure 4.49 illustrates the reservoir simulation results that match the results of the well-testing data points. In order to have a perfect match for the average reservoir pressure, the aquifer data were modified using trial and error techniques. Table 4.4 lists the final results that represent the North African aquifer data.

Table 4.4. The water aquifer properties data.

Parameter	Value	unit
Location	Bottom	-
Thickness	1,000	ft
Porosity	15	%
Permeability	220	md
Radius	8,600	ft
Angle	0.85	Unitless
Modeling method	Carter-Tracy	-
Leak	Leakage is allowed	-

In addition, as shown in Figure 4.49, the trend line mimics the current average reservoir pressure and the forecasting reservoir pressure performance until the year 2050. These results were used in the future reservoir performance calculations section to predict the well deliverability in the following years.

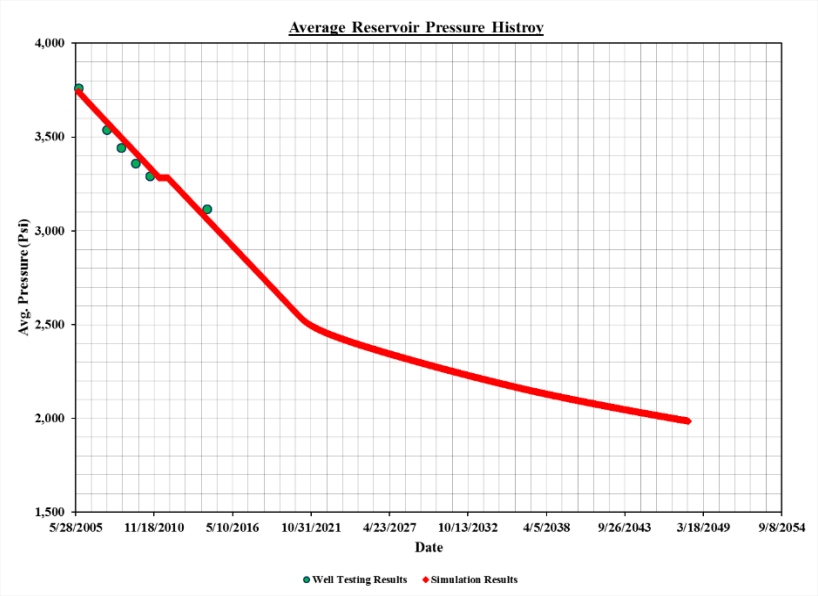

Figure 4.49. Reservoir pressure history result match with the well-testing results using reservoir simulation.

Moreover, Figure 4.50 illustrates the relationship between the gas production rates over the years. The plot shows the zero rate in 2011 when the well was shut-down. The plateau period that represents the optimum production period continued at 45 MMscf/day until 2022. After that, the production rate declines significantly from 45 MMscf/day to 10 MMscf/day in 2035. Then, the gas rate decreases slowly until reaching 8 MMscf/day in 2050. Figure 4.51 demonstrates the relationship and the effect of the water cut on the gas production rate. The decline starts when the water begins invading the reservoir in 2022.

The plot proves that the relationship is an inverse relationship, and the water has a negative impact on the gas production rate.

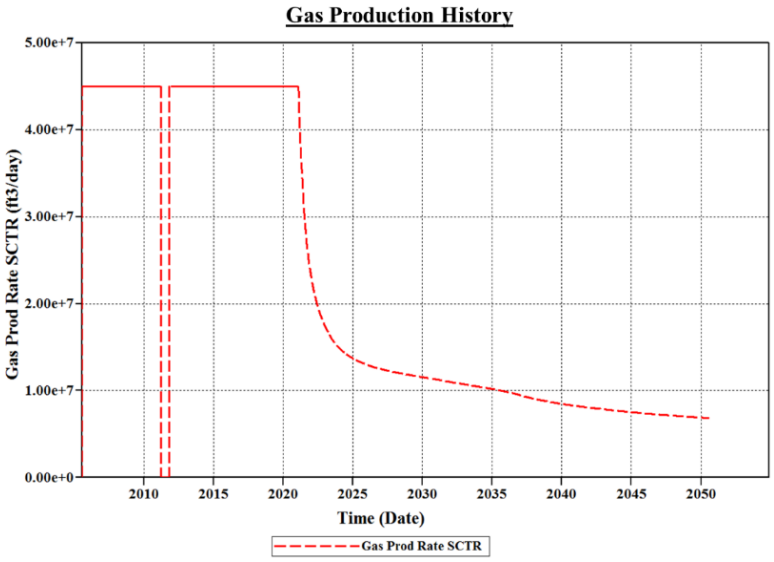

Figure 4.50. Gas production rate simulation history.

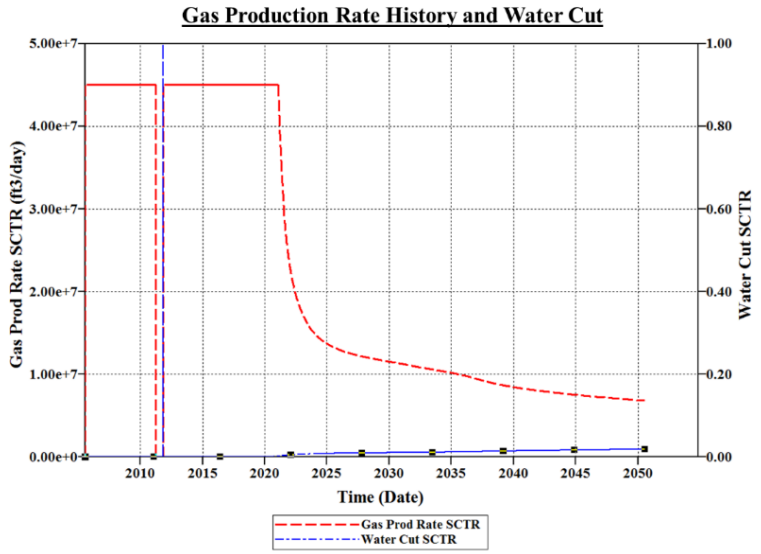

Figure 4.51. The relationship between the gas production rate and water cut simulation history.

Figure 4.52 illustrates the relationship of the condensate production rate. In the early years, the condensate production rate increased until reaching the rate of around 1,350 bbl/day. Then, the production rate decreased slowly until the year 2022 at the rate of around 1,190 bbl/day. In the same year, the water production starts and the condensate production rate declines rapidly, as shown in Figure 4.53. Therefore, this relationship is an inverse relation where the condensate production rate decreases as the water production invasion increases.

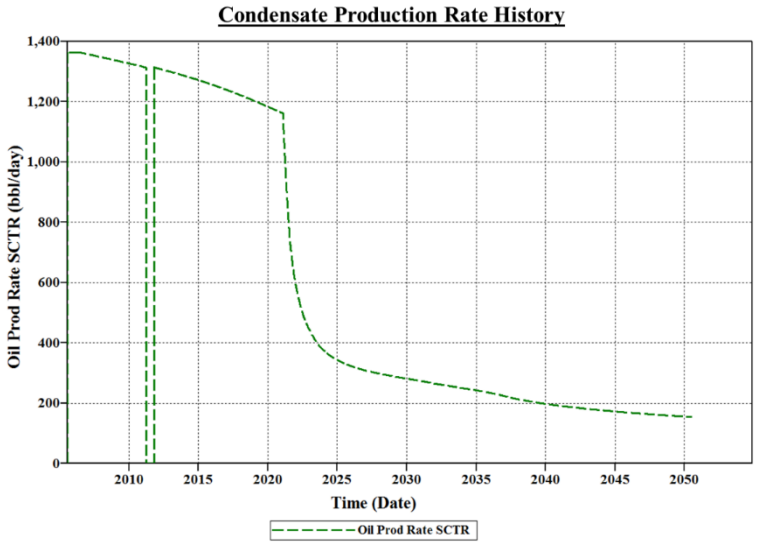

Figure 4.52. Condensate production rate simulation history.

The condensate holdup throughout the reservoir is shown in Figure 4.54, where the maximum liquid dropout shows near the wellbore region. In addition, the significant change in liquid volume is around 1,600 ft where the condensate volume increased rapidly to reach 8.62E-4 fracture volume. Due to the high pressure drop near the wellbore region, the maximum amount of condensate dropout happens in this area. Far away from the

wellbore region, the liquid dropout is an almost constant value. Also, this is proved using a well-testing interpretation tool that showed the condensate blockage is around the wellbore region. Figure 4.55 illustrates the change in condensate volume fracture over the years where the maximum amount is around 0.55 in 2055 in a distance of around 700 ft. This proves that the condensate volume increases as the average reservoir pressure decreases, which causes an increase in the pressure drop over the years.

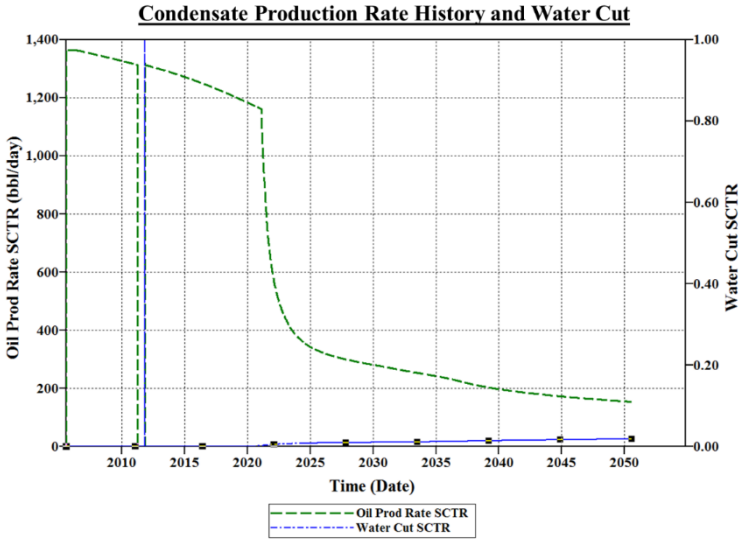

Figure 4.53. The relationship between the condensate production rate and water cut simulation history.

Figure 4.56 shows the 3-D model for the reservoir, which illustrates the water cut movement throughout the reservoir layers over the years. As shown, the three bottom layers will be completely filled with the water in 2055, and the water cut will reach 0.60 at the fourth layer. Therefore, this movement of water from the aquifer to the reservoir depends on the vertical permeability of the reservoir.

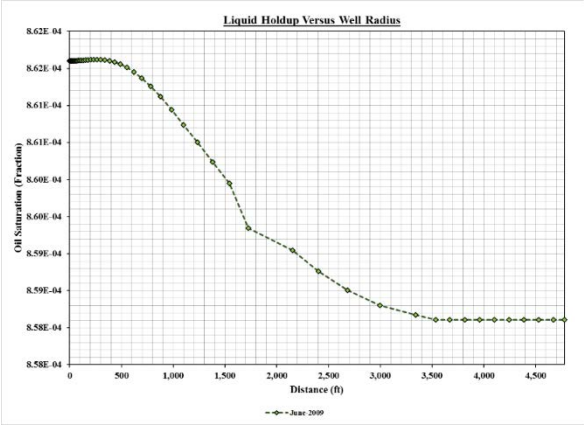

Figure 4.54. Condensate dropout throughout the reservoir radius.

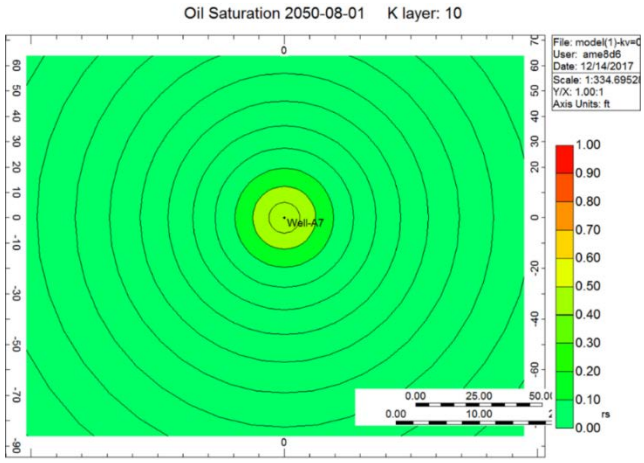

Figure 4.55. Condensate dropout over the years.

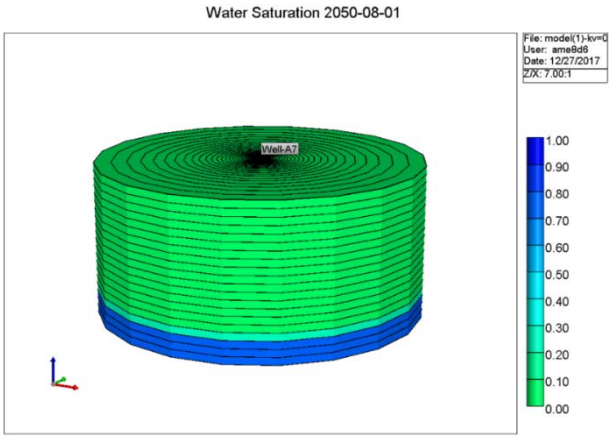

Figure 4.56. Water cut over years.

4.7 FUTURE FLOW PERFORMANCE OF THE FIELD

4.7.1 Applicability of Equations. The modified empirical method was tested to investigate the applicability of the equation results with the well deliverability analysis in the 2009 and 2014 outcomes. Table 4.5 shows the prediction results of the AOF using the modified empirical method. The results indicate that the equation is applicable for this case, and the relative error did not exceed 4% in the inflow coefficient. On the other hand, the absolute open flow (AOF) potential has a high error value which is around 10%, as seen in Table 4.6.

Table 4.5. The equation applicability in the modified empirical method.

Pressure Psi	C from Equation MMScf/day/Psi^2	AOF from Deliverability MMScf/day	AOF from Equation MMScf/day
3,117.13	2.844E-12	636.484	571.103

Table 4.6. Relative error results for the modified empirical method calculations.

Parameter	Relative Error, (%)
C	3.75
AOF	10.272

The theoretical method was also tested to investigate the error in Equation 3.73 and 3.74, as mentioned in Section 3. Table 4.7 demonstrates the results of the prediction the AOF and the theoretical parameters. Furthermore, Table 4.8 shows the relative error where the error value was around 7 % for the theoretical parameters. Although the relative errors

for the input values are somewhat high, the relative error that was determined from the absolute open flow (AOF) potential did not exceed 0.03 %, as seen in Table 4.9.

Table 4.7. The equation applicability in the theoretical method.

Pressure Psi	a from Equation Psi^2/MMScf /day	b from Equation (Psi/MMScf /day)^2	AOF from Deliverability MMScf/day	AOF from Equation MMScf/day
3,117.13	3,949.38	33.49	501.60	501.482

Table 4.8. Relative error results for the theoretical method calculations.

Parameter	Relative Error, (%)
a	5.06
b	7.5
AOF	0.024

4.7.2 Application of the Equations. Table 4.9 shows the final results of the AOFs empirical method that were predicted in 2014, 2018, and 2050. These values are shown graphically in Figure 4.57. As the reservoir pressure is depleted, the IPR curve is shifted down over the years, and this causes the production productivity to reduce.

Table 4.9. The prediction results of the IPR parameters.

Average Reservoir Pressure Psi	Date MM/DD/YYYY	C MMScf/day/Psi^2	AOF MMScf/day
3,117.13	06/01/2014	2.844E-12	571.10
2,780.56	02/01/2018	3.038E-12	444.67
1,954.85	08/01/2050	3.510E-12	183.764

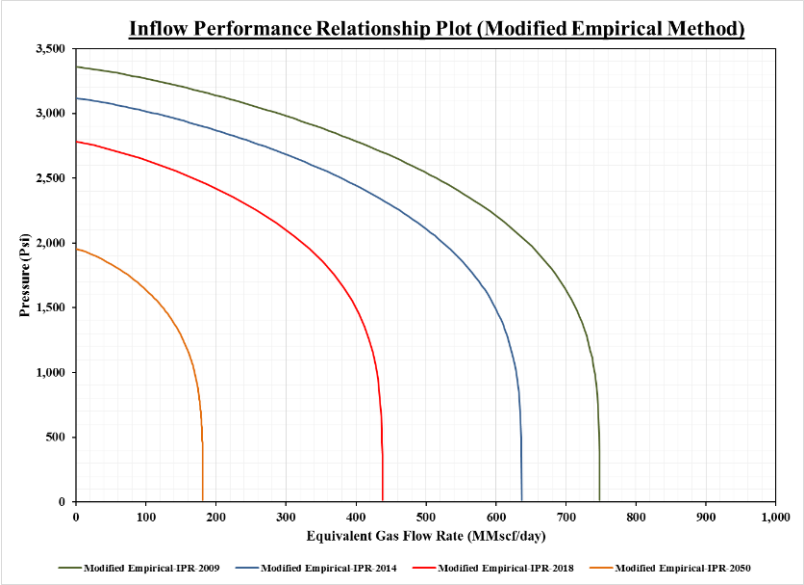

Figure 4.57. Predicting the IPR curves using the modified empirical method.

Finally, Table 4.10 lists the final results of the AOFs theoretical method that were predicted in 2014, 2018, and 2050. In addition, Figure 4.58 illustrates these results on the IPR curves that represent the performance of the reservoir in the future. As seen in the figure, the IPR curves are shifted down due to a decrease in the average reservoir pressure that caused the well performance productivity to reduce.

Table 4.10. The prediction results of the IPR parameters.

Average Reservoir Pressure Psi	Date MM/DD/YYYY	a from Equation Psi^2/MMScf /day	b from Equation (Psi/MMScf /day)^2	AOF MMScf/day
951.241	06/01/2014	3,759.00	31.14	501.48
2,780.56	02/01/2018	3,697.34	31.36	441.07
1,954.85	08/01/2050	3,200.52	27.14	320.85

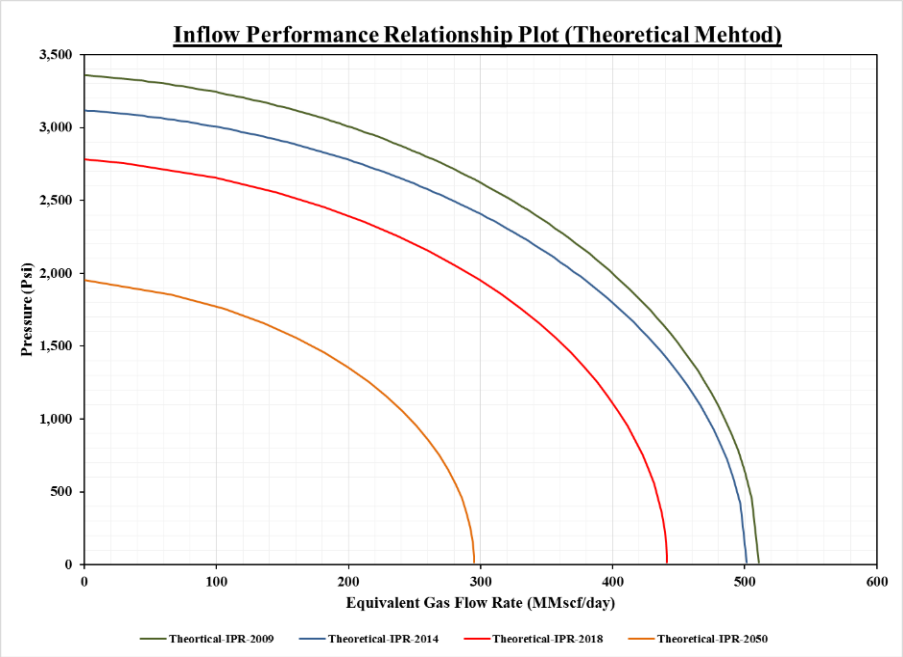

Figure 4.58. Predicting the IPR curves using the theoretical method.

4.7.3 Future Scenarios for Matching VLP with IPR. As shown in Figure 4.59 and 4.60, the wellhead pressure that is required to lift the hydrocarbon to the surface is decreased and shifted down as the average reservoir pressure decreases. All the volume lift pressure (VLP) pressures assumptions are matched with the IPR curves in 2009, 2014, and 2018. On the other hand, the IPR curve in 2050 is matched only with the VLP pressure at 1,200 psi and below. The gas flow rate system is increased as the wellhead pressure decreased where the range of the gas flow rate system is between 40 to 100 MMscf/day. The gas flow rate system results are almost the same in both methods, which proves that at the low pressure, both methods have the same result in the IPR and VLP curves. Finally, the difference in both methods is in the AOF value where the empirical method is the optimistic technique, and the theoretical method is the conservative technique.

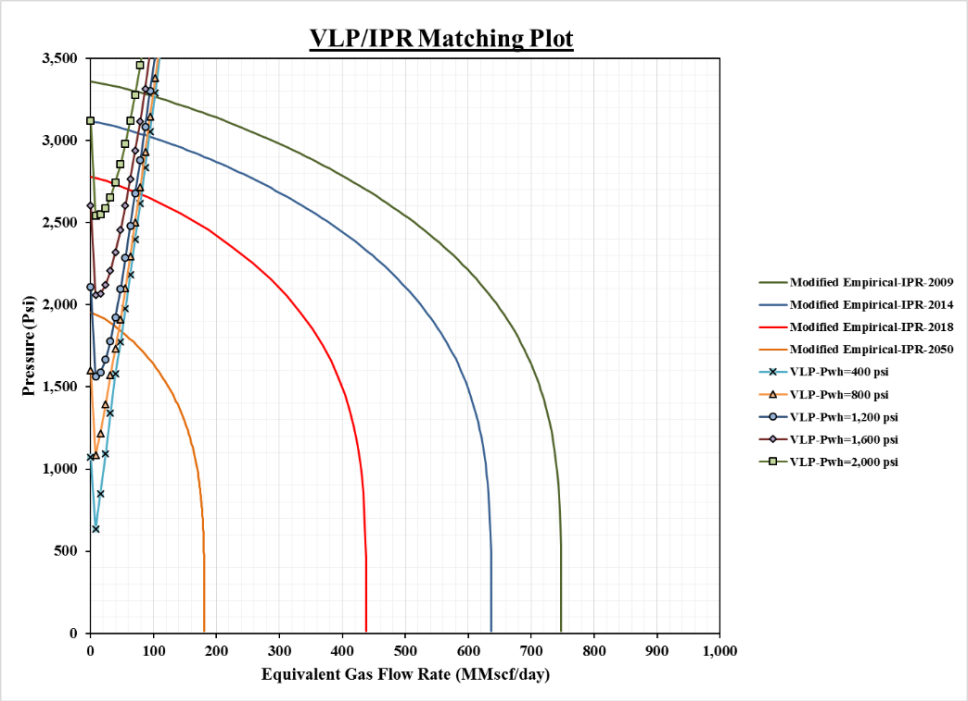

Figure 4.59. Predicting the match of VLP with the empirical IPR curves.

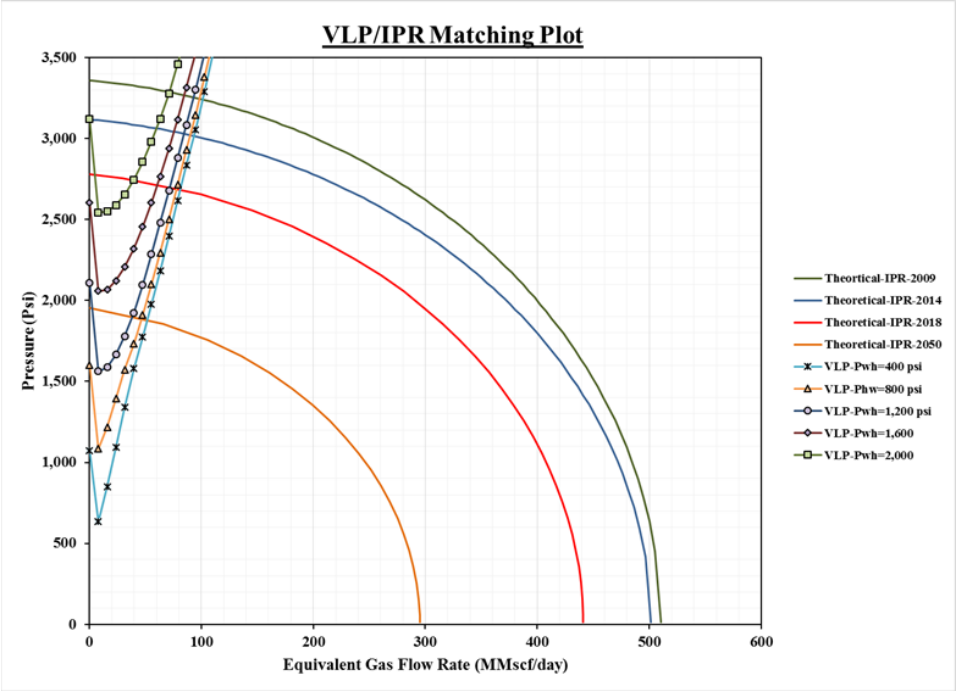

Figure 4.60. Predicting the match of VLP with the theoretical IPR curves.

4.8 DEVELOPMENT STRATEGY PLAN OF THE FIELD

In order to improve the gas recovery factor and to study the water cut effect, the development strategy plan was based on Figure 4.61. This figure represents the formation and well schematic of the North African field where the formation top is at a depth of 9,085.5 ft and the gas-water contact is at a depth of 9,435.5 ft. In addition, the total pay zone thickness is 350 ft, and each layer has a 25 ft thickness. Also, the North African water aquifer is shown in blue, which is classified as a bottom water drive with a 1,000 ft thickness. The strategy was done by closing the lower layers to avoid early water invasion into the reservoir.

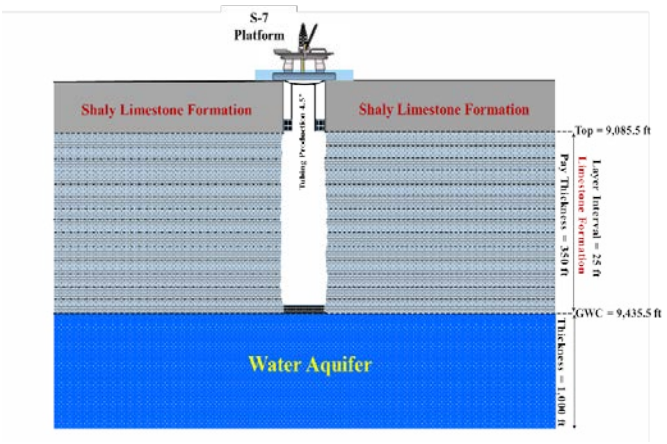

Figure 4.61. The North African formation schematic.

Figure 4.62 illustrates the relationship of the water cut history for different strategy plans over the years. The results indicate that when the pay zone thickness is opened completely, the water starts moving into the reservoir early. As shown in Figure 4.62, the dark blue case with a 350 ft thickness has a significantly higher water cut than the other cases.

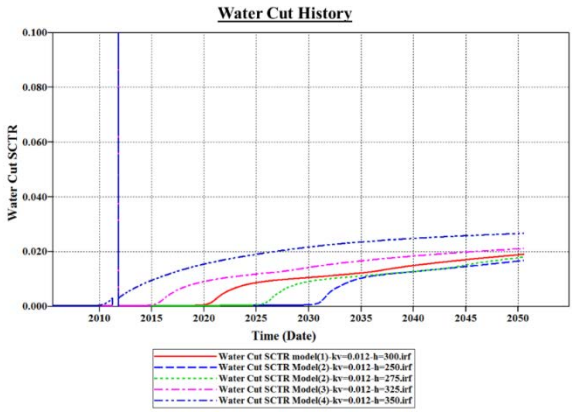

Figure 4.62. Water cut sensitivity results over the years.

In addition, Figure 4.63 shows the relationship of the gas production rate history over the years where the thickness has the main effect on the plateau period before the gas production rate starts declining. When the pay zone thickness is high, the gas production decline starts earlier. As shown in Figure 4.63 and 4.64, this happens due to the water influx into the reservoir where the water drive has a negative impact on the gas production rate.

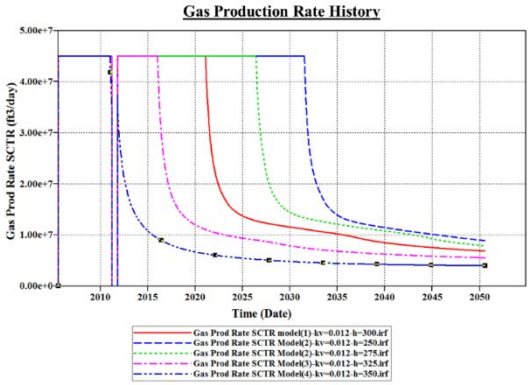

Figure 4.63. Gas production rate sensitivity results over the years.

Also, the gas recovery factor is affected by the formation thickness where the lower thickness results in a higher gas recovery factor, as shown in Figure 4.64. The main reason

that affected the gas recovery is the water cut. These is a higher gas recovery factor, the reservoir has a lower water cut.

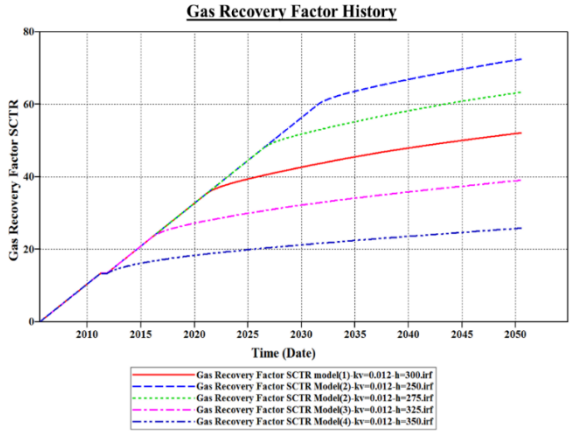

Figure 4.64. Gas recovery factor sensitivity results over the years.

Moreover, the result details are listed in Table 4.11, which includes the water cut history and the gas recovery factor for every 10 years at each pay zone thickness case. As shown, the water cut increases gradually over the years, especially in a large thickness formation. However, the gas recovery factor decreases as the water cut increases. Furthermore, this impacts the gas recovery factor, which is reduces by 43.3% in 2040 from the 250 ft to 350 ft thickness cases. The base case gas recovery factor is increased by 24.37% in 2040 compared to the 350 ft thickness case. On the other hand, the base case water influx is reduced by 0.01 (fraction) in 2040 compared to the 350 ft thickness case.

Table 4.12 shows the final results in 2050 where the water cut reaches a high value of around 0.0267 (fraction) at the 350 ft thickness case. However, at the same year and thickness, the gas recovery factor is around 25.82%, which is lower by 46.63% compared to the 250 ft thickness case.

Table 4.11. The results of the formation thickness sensitivity.

Thickness Ft	Date MM/DD/YYYY	Water Cut Fraction	Recovery Factor %
350	08/01/2010	0.00039	10.44
	08/01/2020	0.01545	18.31
	08/01/2030	0.0217	21.21
	08/01/2040	0.025	23.56
325	08/01/2010	0.00026	10.44
	08/01/2020	0.0091	27.19
	08/01/2030	0.0142	32.20
	08/01/2040	0.0184	35.81
300 (Base Case)	08/01/2010	0.00026	10.44
	08/01/2020	0.00053	32.68
	08/01/2030	0.0105	42.64
	08/01/2040	0.015	47.93
275	08/01/2010	0.00025	10.44
	08/01/2020	0.00033	32.68
	08/01/2030	0.0091	51.78
	08/01/2040	0.01273	58.20
250	08/01/2010	0.00025	10.44
	08/01/2020	0.00033	32.68
	08/01/2030	0.00058	56.32
	08/01/2040	0.01270	66.86

Table 4.12. The final results of the formation thickness sensitivity in the target year.

Date MM/DD/YYYY	Thickness Ft	Water Cut Fraction	Recovery Factor %
8/1/2050	350	0.0267	25.82
	325	0.0211	39.05
	300 (Base Case)	0.0191	52.12
	275	0.0180	63.33
	250	0.0168	72.45

5. CONCLUSIONS & RECOMMENDATIONS

5.1 CONCLUSIONS

1. The open-hole log analysis indicates that the formation has lower shale value where GR log reading is below 25 GAPI. In addition, the sonic log line trend is almost constant throughout the target zone, which indicates that the reservoir has consistent lithology. Moreover, the separation between resistivity readings refers to the hydrocarbon zone. Furthermore, the initial water saturation is very low at around 7%, and the formation fills with a high amount of hydrocarbon.
2. Elan volume and Elan fluid plots show deep and more detailed information about the North African formation, which is crucial in order to detect the bed formation thickness, average reservoir porosity, average initial water saturation, and fluid distribution throughout the depth.
3. The open-hole interpretation results indicate that the formation has good petrophysical properties, and the pay zone thickness is high enough to have significant reservoir potential gas production.
4. A compositional model built based on Peng-Robinson EOS in order to tune the North African tests for fluid to predict and simulate the behavior of the reservoir fluid.
5. The tuning process is a very important step in order to build a proper reservoir simulation that represents the real field data.
6. Phase envelope illustrates the liquid dropout distribution when the pressure falls below the dew-point pressure where the maximum liquid volume is around 1% at 1,700 psi. These results indicate that the gas condensate fluid is classified as a lean gas condensate

fluid where the maximum liquid volume does not exceed 1%, which represents a low value of liquid dropout. The liquid volume is increased by 0.1% every around 150 psi.

7. The research shows that all Z-factor correlations have lower error when pressure is below 3,500 psi compared to the laboratory gas deviation factor results.
8. Comparison results between averaging correlation results and gas deviation factor from the laboratory show that the trend lines are very close and the error is very low.
9. The correlation by Lee, Gonzalez and Eakin gives accurate results for gas viscosity, especially when fluid composition contains a high percentage of CO2.
10. Compositional model, PVT analysis, and open-hole log interpretation are crucial input data to give a clear picture about the formation and fluids with which they are treated.
11. In order to obtain accurate well testing interpretation, the pressure derivative technique is an essential method. This method is used in order to detect the radial flow region, and then, the reservoir permeability and skin factor are obtained. The pressure derivative shows the wellbore, reservoir, and boundary behavior.
12. The production period before the test is very important to obtain accurate pressure derivative shape and accurate reservoir characteristics parameters.
13. The derivative overlay technique is the key factor for the well testing interpretation in order to adjust the gas flow rate from the surface value to the downhole (sandface) values.
14. The Bourdet method using 0.2 smoothing is a technique widely used in order to calculate the pressure derivative, which allows precise detection of the radial flow region. If the smoothing in the pressure derivative is higher or lower than 0.2, the analysis is likely to be misinterpreted and the results obtained are less accurate.

15. Because of the pressure below the dew-point pressure, the reservoir has two-phase flow that makes delineation in the pressure derivative through the reservoir, which is considered as composite radial model. The derivative shows the three radial flow regions.
16. The superposition plot and Gringarten type curve approaches give close results compared to the software results.
17. Hegeman models match the decreasing the wellbore storage and gives the precise wellbore storage coefficient values.
18. In order to obtain the excellent model match with the pressure derivative, the external model is the most effective.
19. Drawdown test analysis shows that the relationship between the composite radius and the gas flow rate is in direct proportion.
20. The results from the rate-dependent skin and time-dependent skin methods are very close to each other. In cases where there is one buildup and multiple drawdowns, the time-dependent skin is more confident and the recommended method.
21. Deliverability results from Excel, Saphir, and Prosper are compatible when the reservoir potential production is due to multiple reasons, such as the formation bed thickness, negative skin factor, lower dependent skin value, lower liquid dropout (almost only gas production), and high reservoir permeability.
22. The performance exponent (n) value is around 0.81, which means the reservoir fluid behavior is close to the laminar flow.

23. Three techniques that were used gave different results of absolute open flow (AOF) potential value where the empirical method overestimated the results. The explanation of the difference in results is based on the assumption of the equations.
24. The results of two tests indicate that the performance exponent (n) value is constant throughout the reservoir life, which means the future flow behavior is laminar flow.
25. The average reservoir pressure history depends on the aquifer parameters since these parameters are the only unknown inputs. By changing the aquifer properties, the average reservoir pressure history was reached and matched with the well testing results.
26. The liquid dropout throughout the formation radius is very low and increased rapidly when the formation radius was around 1,500 ft.
27. The condensate volume throughout the years reaches a maximum near the wellbore region.
28. Comparison between results from the deliverability tests and future performance equations shows that the future performance equation has lower error percentages and is applicable for this case study.
29. The vertical lift performance curve had the same results in three deliverability methods.
30. The completion effect is the main factor that can be used in order to create a development plan strategy in the future. This technique is useful to obtain high gas recovery.
31. The water influx has a negative effect on the reservoir performance. A higher water cut value results a lower gas reservoir recovery.

5.2 FUTURE WORK RECOMMENDED

The following titles are suggestions for future work in order to obtain a comprehensive study about the North African field:

1. Full field reservoir simulation including all wells. Perform ‘what if’ scenarios for larger tubing sizes.
2. Investigate sensitivity of the tubing flow (VLP) using Gray’s correlation for gas wells
3. Integrate an economic assessment with the tubing size study in #1

BIBLIOGRAPHY

1. Adkar Abdrakhmanov (2013). Modeling and Optimization of the Rich Gas Condensate Reservoir. Norwegian University of Science and Technology.

2. Agarwal, R. G. (1979). Real Gas Pseudo-Time - A New Function for Pressure Buildup Analysis of MHF Gas Wells. Society of Petroleum Engineers. doi: 10.2118/8279-MS.

3. Agarwal, R.G., Al-Hussainy, R., and Ramey, H.J. (1965). The Importance of Water Influx in Gas Reservoirs. Journal of Petroleum Technology 17 (11): 1336–1342. SPE-1244-PA.

4. Ahmed T. (2000). Reservoir Fluid Properties. In: Reservoir Engineering Handbook. Houston, Texas, USA, Gulf Professional Publishing.

5. Ahmed T. (2006). Reservoir Engineering Handbook, Fourth Edition. Burlington. The United State of America: Gulf Professional Publishing.

6. Akpabio, J. U., Udofia, E. E., & Ogbu, M. (2014, August 5). PVT Fluid Characterization and Consistency Check for Retrograde Condensate Reservoir Modeling. Society of Petroleum Engineers. doi:10.2118/172359-MS.

7. Al-Hussainy, R., & Ramey, H. J. (1966). Application of Real Gas Flow Theory to Well Testing and Deliverability Forecasting. Society of Petroleum Engineers. doi:10.2118/1243-B-PA.

8. Al-Ismail, M. (2010). Field Observations of Gas-Condensate Well Testing. M.S. Thesis, Stanford University.

9. Al-Ismail, M., & Horne, R. N. (2010). Pressure Buildup Test Analysis of a Gas Condensate Well in the Middle East. Society of Petroleum Engineers. doi:10.2118/134671-MS.

10. Al-Shaidi, S (1997). Modelling Of Gas Condensate Flow in Reservoir at Near Wellbore Conditions, PhD. Thesis, Heriot-Watt University.

11. Amanat U. Chaudhry. (2003). Fundamentals of Pressure Buildup Analysis Method. In: Gas Well Testing Handbook. Houston Texas, USA, Gulf Professional Publishing.

12. Asquith, G.B., and Gibson, C, R. (1982). Basic Well Log Analysis for Geologists. The American Association of Petroleum Geologists.

13. Bassiouni, Z. (1994). Theory, Measurement, and interpretation of well logs. SPE Textbook Series Vol.4.

14. Bourdet, D., Ayoub, J. A., & Pirard, Y. M. (1989). Use of Pressure Derivative in Well Test Interpretation. Society of Petroleum Engineers. doi:10.2118/12777-PA.

15. Bruno Roussennac. (2001). Gas Condensate Well Test Analysis. Stanford University.

16. C. Whitson, O. Fevang, and T. Yang, (1999). Gas Condensate PVT – What's Really Important and Why?. Presented at the IBC Conference –Optimization of Gas Condensate Fields, held in London, Jan 28-29, 1999.

17. Chase, R. W. (2002). Improved Estimation of Gas Well Deliverability from Single-Point Tests. Petroleum Society of Canada. doi:10.2118/02-11-04.

18. Chen, Z., (2007). Reservoir Simulation: Mathematical Techniques in Oil Recovery. Society for Industrial and Applied Mathematic (SIAM).

19. Computer Modelling Group (CMG). (2013). WinProp Manual Technical Description. Phase behavior and fluid property.

20. E-learning system, 2012: https://www.ipims.com.

21. Fan Li, Harris B. W., Jamaluddin A., Kamath J., Mott R., Pope G. A. and Whitson C. H. (2006). Understanding Gas Condensate Reservoirs. Oilfield Review, 17 (4)14–27.

22. Fekete Associates Inc, 2010: https://ihsmarkit.com.

23. Fevang, Φ and Whitson, C. H. (1996). Modeling Gas-condensate Well Deliverability. SPE Reservoir Engineering, 221-230.

24. Firoozabadi, A., Olsen, G., & van Golf-Racht, T. (1987). Residual Gas Saturation in Water-Drive Gas Reservoirs. Society of Petroleum Engineers. doi:10.2118/16355-MS.

25. Gravier, J. F., Lemouzy, P., Barroux, C., and Abed, A. F. (1986). Determination of Gas condensate Relative Permeability on Whole Cores under Reservoir Conditions, SPEFE.

26. Gringarten, A. C., Bourdet, D. P., Landel, P. A., & Kniazeff, V. J. (1979). A Comparison between Different Skin and Wellbore Storage Type-Curves for Early-Time Transient Analysis. Society of Petroleum Engineers. doi:10.2118/8205-MS.

27. Guehria, F. M. (2000). Inflow Performance Relationships for Gas Condensates. Society of Petroleum Engineers. doi:10.2118/63158-MS.

28. Guo, B., and Ghalambor, A. (2005). Natural Gas Engineering Handbook.

29. Hashem, Y. K. S., & Kazemi, H. (1996). Reservoir Properties and Stabilized Gas Well Performance from Short Deliverability Tests. Society of Petroleum Engineers. doi:10.2118/35618-MS.

30. Houpeurt, A. (1959). On the Flow of Gases in Porous Media, Revue de L'Institut Fracdais du Petrole, XIV (11), 1468-1684.

31. Houzé, O, Viturat, D, Fjaere, O.S., www.kappaeng.com/downloads/ddabook, Dynamic Data Analysis, 2012.

32. Izuwa, N. C., & Nwosu, C. N. (2014). Influence of Aquifer Support on Gas Condensate Reservoir Performance. Society of Petroleum Engineers. 172372-MS.

33. J.R. Jones and R. Raghavan. (1985). Interpretation of Flowing-Well Response in Gas-Condensate Wells. Paper SPE14204, SPE Annual Technical Conference and Exhibition, Las Vegas, Nevada.

34. John Lee, Robert A. Wattenbarger. (1996). Properties of Natural Gases. In: Gas Reservoir Engineering. Richardson, Texas, Society of Petroleum Engineering.

35. Johnston, J. L., Lee, W. J., & Blasingame, T. A. (1991). Estimating the Stabilized Deliverability of a Gas Well Using the Rawlins and Schellhardt Method: An Analytical Approach. Society of Petroleum Engineers. doi:10.2118/23440-MS.

36. Jokhio, S. A., & Tiab, D. (2002). Establishing Inflow Performance Relationship (IPR) for Gas Condensate Wells. Society of Petroleum Engineers. doi:10.2118/75503-MS.

37. Kabir, C. S. (2006). What Is the Real Measure of Gas-Well Deliverability Potential?. Society of Petroleum Engineers. doi:10.2118/84469-PA.

38. Kamal, M. M., Freyder, D. G., & Murray, M. A. (1995). Use of Transient Testing in Reservoir Management. Society of Petroleum Engineers. doi:10.2118/28008-PA.

39. Kamal, M.M. (2009). Transient Well Testing. Mongraph Series Vol.23.

40. Kamath, J. (2007). Deliverability of gas-condensate reservoirs – field experiences and prediction techniques, J. Pet. Tech. V.59 No.4, 94-99.

41. Kelkar, M. (2008). Natural Gas Production Engineering. First Edition. Tulsa, Oklahoma: PennWell.

42. Kgogo, T. C., & Gringarten, A. C. (2010). Comparative Well-Test Behaviors in Low-Permeability Lean, Medium-rich, and Rich Gas-Condensate Reservoirs. Society of Petroleum Engineers. doi:10.2118/134452-MS.

43. Lee, W. J. and Holditch, S. A. (1982). Application of Pseudotime to Buildup Test Analysis of Low Permeability Gas Wells with Long-Duration Wellbore Storage Distortion, J. Pet. Tech., 2877-2887.

44. Li, F., Billy, W.H., Jamaluddin, A., Kamath, J., Mott, R., Pope, G., Shandrygin, A., and Whitson, C.H. (2005). Understanding Gas-Condensate Reservoirs. Oilfield Review 17(4).

45. Liang, P., Rahmanian, M., & Mattar, L. (2013). Superposition-Rate as An Alternative to Superposition-Time. Society of Petroleum Engineers. doi:10.2118/167124-MS.

46. Matthews, C. S. (1961). Analysis of Pressure Buildup and Flow Test Data. Society of Petroleum Engineers. doi:10.2118/1631-G-PA.

47. Matthews, C. S. (1986). Transient, Semi-steady State, and Steady-State Flow. Society of Petroleum Engineers. doi:10.2118/15278-PA.

48. McCain Jr.W.D (1991). Reservoir fluid property correlations-State of the Art. SPE.

49. Mellitah Gas & Oil B.V, 2016: https://mellitahog.ly.

50. Meunier, D. F., Kabir, C. S., & Wittmann, M. J. (1987). Gas Well Test Analysis: Use of Normalized Pseudovariables. Society of Petroleum Engineers. doi:10.2118/13082-PA.

51. Moses, P. L. and Donohoe, C. W. (1962). Gas-condensate reservoirs, Petroleum Engineering Handbook. SPE, pp. 39:1-39-28.

52. National Oil Corporation of State of Libya, 2016: https://noc.ly.

53. O'Dell, H. G. and Miller, R. N. (1967). Successfully cycling a Low Permeability, High-Yield Gas Condensate Reservoir. JPT 41-47; Trans., AIME, 240.

54. Ogolo, N. A., Isebor, J. O., & Onyekonwu, M. O. (2014). Feasibility Study of Improved Gas Recovery by Water Influx Control in Water Drive Gas Reservoirs. Society of Petroleum Engineers. doi:10.2118/172364-MS.

55. Petroleum Expert. (2011). PVT-P Manual Technical Description Version 8.5.

56. PetroSkills Courses, 2014: https://www.petroskills.com.

57. Poe, B. D., & Jennings, J. W. (1988). A Review of the Methods of Estimating Stabilized Absolute Open-Flow Potential of Gas Wells. Society of Petroleum Engineers. doi:10.2118/17308-MS.

58. Raghavan, R. and Jones, J. R. (1996). Depletion Performance of Gas-Condensate Reservoirs. JPT 725-731.

59. Raghavan, R., Chu, W.C., and Jones, J. R. (1995). Practical considerations in the analysis of gas-condensate well tests. SPE paper 30576.

60. Rawlins, E. L. and Schelhardt, M. A. (1936). Back-Pressure Data on Natural Gas Wells and Their Application to Production Practices. U. S. Bureau of Mines Monograph 7.

61. Rishi raj Phukan. (2012). Seminar on Water Influx and Well Testing. [Presentation].

62. Roussennac, B. (2001). Gas Condensate Well Test Analysis. M.Sc. Thesis, Stanford University.

63. Sadeghi, A., Gerami, S., & Masihi, M. (2010). New Technique for Calculation of Gas Condensate Well Deliverability. Society of Petroleum Engineers. doi:10.2118/130139-MS.

64. Schlumberger. (1972). Log interpretation principles and applications.

65. Schlumberger. (2013). Log Interpretation Charts.

66. Shi, C., & Horne, R. N. (2008, January 1). Improved Recovery in Gas-Condensate Reservoirs Considering Compositional Variations. Society of Petroleum Engineers. doi:10.2118/115786-MS.

67. Spivey, J.P., and Lee, W.J. (2013). Applied Well Test Interpretation. SPE Textbook Series Vol.13.

68. Sugiarto, I., Mazumder, S., Wittemeier, R., & Sharma, V. (2015). Inflow Performance Relationship correlation of 2 Phase CBM Reservoir. Society of Petroleum Engineers. doi:10.2118/176185-MS.

69. Thomas, F. B., Bennion, D. B., & Andersen, G. (2009). Gas Condensate Reservoir Performance. Petroleum Society of Canada. doi:10.2118/09-07-18.

70. U.S. Energy Information Administration, 2015: https://www.eia.gov/.

71. Ugwu, J., Mason, E., and Gobina, E., (2016). Modified Gas Condensate Down-hole PVT Property Correlations. Robert Gordon University, Aberdeen.

72. Urayet, A. A. (2011). Advanced Natural Gas Engineering Course. University of Tripoli.

73. Villa, M., Farhat, A., & Pirodeau, J. (2003). Development of the Subsea Production System for the Bahr Essalam Field. Offshore Mediterranean Conference.

74. Wall, C. G (1982). Characterization of gas-condensate reservoirs and traditional production methods, North Sea Gas-condensate Reservoirs and their Development. Oyez scientific and technical service, pp. 1-12.

75. Whitson, C. H. and Brule, M. R. (2000). Phase Behavior, SPE monograph V. 20.

76. Zendehboudi, S., Ahmadi, M. A., James, L., and Chatzis, I. (2012) Prediction of Condensate-to-Gas Ratio for Retrograde Gas Condensate Reservoirs Using Artificial Neural Network with Particle Swarm Optimization. dx.doi.org/10.1021/ef300443j| Energy Fuels 2012, 26, 3432−3447.

VITA

Abdulaziz Mustafa Em. Ellafi was born in Tripoli, Libya. In May 2011, he received his bachelor's degree in petroleum engineering from University of Tripoli, Tripoli, Libya. After graduation, he worked for University of Tripoli as a teacher assistant from October 2012 to December 2014. He attended Missouri University of Science and Technology, Roll, Missouri, USA, in the spring of 2016. He worked as a researcher under the guidance of his advisor, Dr. Ralph Flori, from June 2016 to May 2018. He participated in the Mid-Continent North America Regional Student Paper Contest on April 2017. He published a conference paper in SPE Trinidad and Tobago Energy Resources Conference 2018. Abdulaziz received a master's degree in Petroleum Engineering in May 2018 from Missouri S&T.